Electronic Supplementary Material (ESI) for Inorganic Chemistry Frontiers.

Supporting Information

The rationalized pathway from field-induced slow magnetic relaxation in Co^{II}–W^{IV} chains to single-chain magnetism in isotopological Co^{II}–W^{V} analogues

Tomasz Charytanowicz, Robert Jankowski, Mikolaj Zychowicz, Szymon Chorazy,* and Barbara Sieklucka*
Faculty of Chemistry, Jagiellonian University, Gronostajowa 2, 30-387 Kraków, Poland

Corresponding authors: simon.chorazy@uj.edu.pl; barbara.sieklucka@uj.edu.pl

Fig. S1	Infrared (IR) absorption spectra of **1**, **2**, **3**, and bpp ligand.	S4
Fig. S2	Solid-state UV-vis-NIR absorption spectra of **1**, **2** and **3**.	S4
Fig. S3	Thermogravimetric (TG) curves for **1**, **2**, and **3**.	S5
Table S1	Crystal data and details of the structure refinement for compounds **1**–**3**.	S6
Fig. S4	Experimental powder X-ray diffraction (P-XRD) patterns of **1**–**3** compared with the respective P-XRD patterns calculated from the structural models obtained within the SC-XRD experiments.	S7
Fig. S5	Additional structural views showing the nearly perpendicular arrangement of neighbouring tetrametallic squares within the cyanido-bridged coordination chains of **1**–**3**.	S8
Fig. S6	Comparison of the asymmetric units of **1**–**3**.	S9
Table S2	Result of Continuous Shape Measures (CShM) analysis for $[W^{IV/V}(CN)_8]^{4-/3-}$ complexes in **1**–**3**.	S10
Table S3	Result of Continuous Shape Measures (CShM) analysis for Co^{II} complexes in **1**–**3**.	S10
Table S4	The selected metric parameters for compounds **1**–**3**.	S11
Fig. S7	Arrangement of water molecules and the hydrogen bonds network in **1**.	S12
Fig. S8	Arrangement of water molecules and the hydrogen-bonds network in **2** and **3**.	S13
Fig. S9	The visualization of π-π interactions involving aromatic rings of bpp ligands in **1**–**3**.	S13
Fig. S10	Direct-current (*dc*) magnetic characteristics of **1**.	S14
Fig. S11	Magnetic-field-dependent alternate-current (*ac*) magnetic characteristics of **1** at T = 1.8 K.	S15
Fig. S12	Temperature-dependent alternate-current (*ac*) magnetic characteristics of **1** at H_{dc}= 1000 Oe.	S16
Fig. S13	Temperature dependence of the magnetic relaxation time in **1** presented with the best-fit curve taking into account three different relaxation pathways with visualized contributions.	S17
Fig. S14	Main direct-current (*dc*) magnetic characteristics of **2** and **3**.	S18
Fig. S15	Field-cooled magnetization curves for **2** recorded at various *dc* fields from the 10–7000 Oe range.	S19
Fig. S16	Field-cooled magnetization curves for **3** recorded at various *dc* fields from the 10–5000 Oe range.	S20
Fig. S17	Field dependences of magnetization gathered for various temperature from the 1.8–11 K range, presented together with the dM/dH versus H plots, for **2** and **3**.	S21
Fig. S18	H–T magnetic phase diagrams for **2** and **3** with the explanation regarding their construction.	S22
Fig. S19	Temperature-dependent alternate-current (*ac*) magnetic characteristics of **2** at H_{dc}= 0 Oe.	S23
Fig. S20	Temperature-dependent alternate-current (*ac*) magnetic characteristics of **3** at H_{dc}= 0 Oe.	S24
Table S5	Basis sets employed in the *ab initio* calculations for Co^{II} complexes of **1**, **2**, and **3**.	S25
Table S6	The energy splitting of ground Kramers doublets and their pseudo-*g*-tensors for **Co1** centres in **1**.	S25
Table S7	The energy splitting of ground Kramers doublets and their pseudo-*g*-tensors for **Co1A** centres in **2**.	S25
Table S8	The energy splitting of ground Kramers doublets and their pseudo-*g*-tensors for **Co1B** centres in **2**.	S26
Table S9	The energy splitting of ground Kramers doublets and their pseudo-*g*-tensors for **Co1A** centres in **3**.	S26
Table S10	The energy splitting of ground Kramers doublets and their pseudo-*g*-tensors for **Co1B** centres in **3**.	S26
Table S11	*Ab initio* calculated zero-field splitting parameters and the related *g*-tensor components for Co(II) complexes of **1**–**3** determined for the full spin Hamiltonian for S = 3/2 compared with the *g*-tensor components corresponding to the effective pseudo spin 1/2 Hamiltonian.taken directly from the results of the *ab initio* calculations for the lowest lying Kramers doublet of the $^4T_{1g}$ multiplet,	S27
Fig. S21	Visualization of four additionally considered magneto-structural models for **1** (ZC-4, ZR-4, ZC-8, ZR-8).	S28

Fig. S22	Comparison of the experimental $\chi_M T(T)$ curve for **1** with the $\chi_M T(T)$ curves calculated for isolated Co1 centres from the *ab initio* calculations and obtained from modelling the magnetic properties using the magneto-structural models of ZC-4, ZR-4, ZC-8, ZR-8, ZC-4(4st.), and ZC-4(4st.).	S29
Fig. S23	Comparison of the experimental $M(H)$ curve for **1** at various low temperatures with the respective $M(H)$ curves calculated for isolated Co1 centres from the *ab initio* calculations and obtained from modelling the magnetic properties using the ZC-12, ZR-12, ZC-4, ZR-4, ZC-8, ZR-8, ZC-4(4st.), and ZR-4(4st.) models.	S30
Fig. S24	The scheme of exchange states for **1** calculated by employing the *ab initio* calculations and two different magneto-structural models of ZC-12 and ZR-12.	S31
Fig. S25	The dependence between the energy of the pairs of exchange states and the energy gaps determined for **1** using the *ab initio* calculations and two magneto-structural models of ZC-12 and ZR-12.	S32
Table S12	The lists of 32 lowest lying exchange states (16 pseudo-doublets) and the respective energy gaps obtained for **1** using the *ab initio* calculations and two magneto-structural models of ZC-12 and ZR-12.	S33
Fig. S26	The scheme of exchange states for **1** calculated by employing the *ab initio* calculations and four different magneto-structural models of ZC-4, ZR-4, ZC-4(4st.), and ZR-4(4st.).	S34
Fig. S27	The scheme of exchange states for **1** calculated by employing the *ab initio* calculations and two different magneto-structural models of ZC-8 and ZR-8.	S35
Fig. S28	The dependence between the energy of the pairs of exchange states and the energy gaps determined for **1** using the *ab initio* calculations and two magneto-structural models of ZC-4 and ZR-4.	S36
Table S13	The lists of 16 lowest lying exchange states (8 pseudo-doublets) and the respective energy gaps obtained for **1** using the *ab initio* calculations and two magneto-structural models of ZC-4 and ZR-4.	S37
Fig. S29	The dependence between the energy of the pairs of exchange states and the energy gaps determined for **1** using the *ab initio* calculations and two magneto-structural models of ZC-8 and ZR-8.	S38
Table S14	The lists of 32 lowest lying exchange states (16 pseudo-doublets) and the respective energy gaps obtained for **1** using the *ab initio* calculations and two magneto-structural models of ZC-8 and ZR-8.	S39
Fig. S30	The dependence between the energy of the pairs of exchange states and the energy gaps determined for **1** using the *ab initio* calculations and two magneto-structural models of ZC-4(4st.) and ZR-4(4st.).	S40
Table S15	The lists of 32 lowest lying exchange states (16 pseudo-doublets) and the respective energy gaps obtained for **1** using the *ab initio* calculations and two magneto-structural models of ZC-4(4st.) and ZR-4(4st.).	S41
Fig. S31	Comparison of the experimental *dc* magnetic data for **2** and **3** with the respective magnetic curves calculated based on the results of the *ab initio* calculations performed for isolated Co centres.	S42
Fig. S32	Possible arrangements of H_2O and Cl- ligands attached to the Co centres in **2** together with the labels of the resulting magneto-structural models that could be considered for the modelling of the magnetic properties.	S43
Fig. S33	Visualization of the ABBA-type magneto-structural models for modelling the magnetic properties of **2**.	S44
Fig. S34	Visualization of the ABAB-type magneto-structural models for modelling the magnetic properties of **2**.	S45
Fig. S35	Visualization of the AABB-type magneto-structural models for modelling the magnetic properties of **2**.	S46
Fig. S36	Scheme of the (AA+BB)-type (part 1) magneto-structural models for modelling the magnetic properties of **2**.	S47
Fig. S37	Scheme of the (AA+BB)-type (part 2) magneto-structural models for modelling the magnetic properties of **2**.	S48
Fig. S38	The alignment of pseudo-*g*-tensor components in the chains of **2** within the tested magneto-structural models of ABBA, ABAB, and AA+BB.	S49
Fig. S39	Comparison of the experimental temperature dependences of the magnetic susceptibility–temperature product for **2** with the respective magnetic curves calculated using the results of the *ab initio* calculations and various magneto-structural models.	S50
Fig. S40	Comparison of the experimental field dependences of magnetization at 25, 30, and 35 K for **2** with magnetic curves calculated using the results of the *ab initio* calculations and various magneto-structural models.	S51
Fig. S41	The scheme of exchange states for **2** calculated by employing the *ab initio* calculations and six different magneto-structural models of C6-ABBA, C6-ABBA(4st.), C12-ABBA, R6-ABBA, R6-ABBA(4st.), and R12-ABBA.	S52
Fig. S42	The scheme of exchange states for **2** calculated by employing the *ab initio* calculations and six different magneto-structural models of C6-ABAB, C6-ABAB(4st.), C12-ABAB, R6-ABAB, R6-ABAB(4st.), and R12-ABAB.	S53
Fig. S43	The scheme of exchange states for **2** calculated by employing the *ab initio* calculations and six different magneto-structural models of C6-AABB, C6-AABB(4st.), C12-AABB, R6-AABB, R6-AABB(4st.), and R12-AABB.	S54
Fig. S44	The scheme of exchange states for **2** calculated by employing the *ab initio* calculations and six different magneto-structural models of C6-AA+BB (part 1), C6-AA+BB(4st.) (part 1), C12-AA+BB (part 1), R6-AA+BB	S55

	(part 1), R6-AA+BB(4st.) (part 1), and R12-AA+BB (part 1).	
Fig. S45	The scheme of exchange states for **2** calculated by employing the *ab initio* calculations and six different magneto-structural models of C6-AA+BB (part 2), C6-AA+BB(4st.) (part 2), C12-AA+BB (part 2), R6-AA+BB (part 12), R6-AA+BB(4st.) (part 2), and R12-AA+BB (part 2).	S56
Fig. S46	The dependence between the energy of the pairs of exchange states and the energy gaps determined for **2** using the *ab initio* calculations and two selected magneto-structural models of C6-AABB and C6-AABB(4st.).	S57
Fig. S47	The dependence between the energy of the pairs of exchange states and the energy gaps determined for **2** using the *ab initio* calculations and the magneto-structural models of C6-AA+BB and C6-AA+BB(4st.) (part 1).	S58
Fig. S48	The dependence between the energy of the pairs of exchange states and the energy gaps determined for **2** using the *ab initio* calculations and the magneto-structural models of C6-AA+BB and C6-AA+BB(4st.) (part 2).	S59
Table S16	The lists of 16 lowest lying exchange states (8 pseudo-doublets) and the respective energy gaps obtained for **2** using the *ab initio* calculations and two magneto-structural models of C6/C12-ABBA.	S60
Table S17	The lists of 16 lowest lying exchange states (8 pseudo-doublets) and the respective energy gaps obtained for **2** using the *ab initio* calculations and two magneto-structural models of R6/R12-ABBA.	S61
Table S18	The lists of 16 lowest lying exchange states (8 pseudo-doublets) and the respective energy gaps obtained for **2** using the *ab initio* calculations and two magneto-structural models of C6/C12-ABAB.	S62
Table S19	The lists of 16 lowest lying exchange states (8 pseudo-doublets) and the respective energy gaps obtained for **2** using the *ab initio* calculations and two magneto-structural models of R6/R12-ABAB.	S63
Table S20	The lists of 16 lowest lying exchange states (8 pseudo-doublets) and the respective energy gaps obtained for **2** using the *ab initio* calculations and two magneto-structural models of C6/C12-AABB.	S64
Table S21	The lists of 16 lowest lying exchange states (8 pseudo-doublets) and the respective energy gaps obtained for **2** using the *ab initio* calculations and two magneto-structural models of R6/R12-AABB.	S65
Table S22	The lists of 16 lowest lying exchange states (8 pseudo-doublets) and the respective energy gaps obtained for **2** using the *ab initio* calculations and two magneto-structural models of C6/C12-AA+BB (part 1).	S66
Table S23	The lists of 16 lowest lying exchange states (8 pseudo-doublets) and the respective energy gaps obtained for **2** using the *ab initio* calculations and two magneto-structural models of R6/R12-AA+BB (part 1).	S67
Table S24	The lists of 16 lowest lying exchange states (8 pseudo-doublets) and the respective energy gaps obtained for **2** using the *ab initio* calculations and two magneto-structural models of C6/C12-AA+BB (part 2).	S68
Table S25	The lists of 16 lowest lying exchange states (8 pseudo-doublets) and the respective energy gaps obtained for **2** using the *ab initio* calculations and two magneto-structural models of R6/R12-AA+BB (part 2).	S69
Fig. S49	Experimental temperature dependence of the $\chi_M T$ for **2** compared with the $\chi_M T(T)$ plots simulated using the results of the *ab initio* calculations combined with the fitting of the exchange coupling employing the magneto-structural model of C6-AABB with three different coupling constants J of 24.2, 25.1, and 25.6 cm^{-1}.	S70
Fig. S50	Experimental temperature dependence of the $\chi_M T$ product under H_{dc} = 1000 Oe for **3** compared with the $\chi_M T(T)$ curves calculated using the results of the *ab initio* calculations combined with the simulations of magnetic exchange employing C6-AABB and C6-AABB(4st.) models.	S71
Fig. S51	The scheme of exchange states for **3** calculated by employing the *ab initio* calculations and two selected magneto-structural models of C6-AABB and C6-AABB(4st.).	S71
Fig. S52	The dependence between the energy of the pairs of exchange states and the energy gaps determined for **3** using the *ab initio* calculations and two selected magneto-structural models of C6-AABB and C6-AABB(4st.).	S72
Table S26	The lists of 16 lowest lying exchange states (8 pseudo-doublets) and the respective energy gaps obtained for **3** using the *ab initio* calculations and two magneto-structural models of C6-AABB and C6-AABB(4st.).	S73
Fig. S53	Comparison of the representative structural fragments of **2** and **3** with other reported cyanido-bridged Co^{II}–$[W^{V}(CN)_8]^{3-}$ chains.	S74
Table S27	Comparison of structural features and magnetic properties of **2** and **3** with other reported Co^{II}–$[W^{V}(CN)_8]^{3-}$ chains.	S75

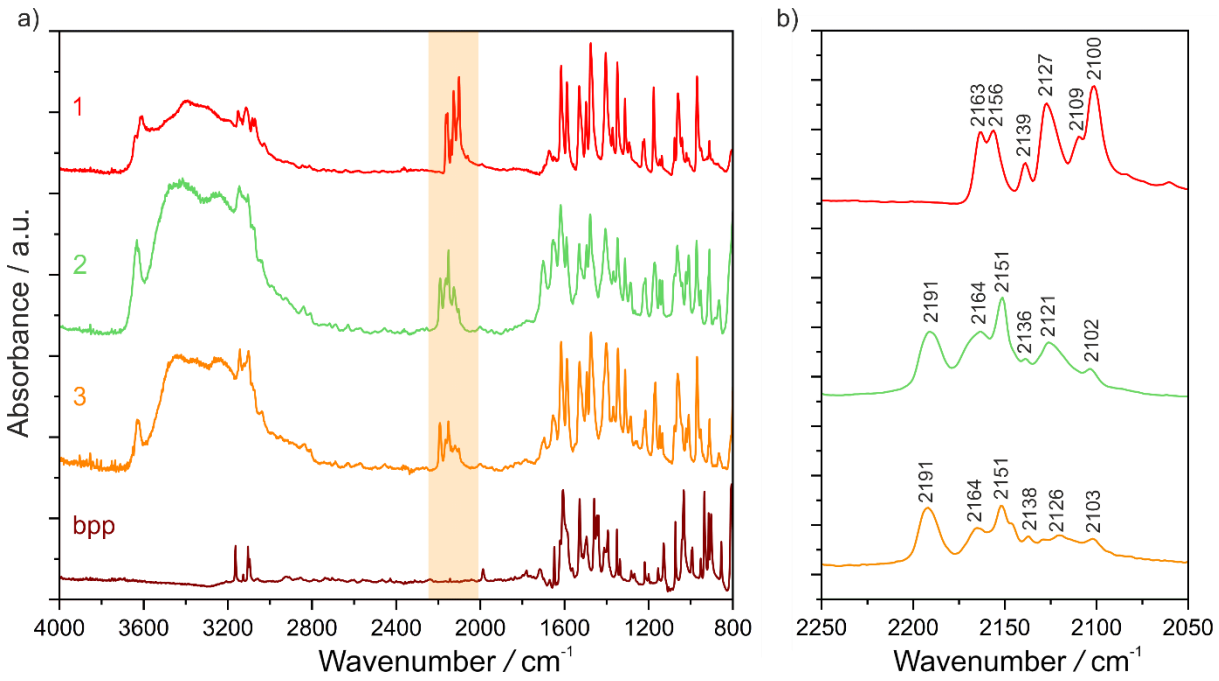

Fig. S1 Infrared (IR) absorption spectra of **1–3** and bpp ligand recorded in the 4000-800 cm^{-1} range (a) together with the enlargement of the 2250–2050 cm^{-1} region representing the absorption bands related to the stretching vibrations of cyanido ligands (b).

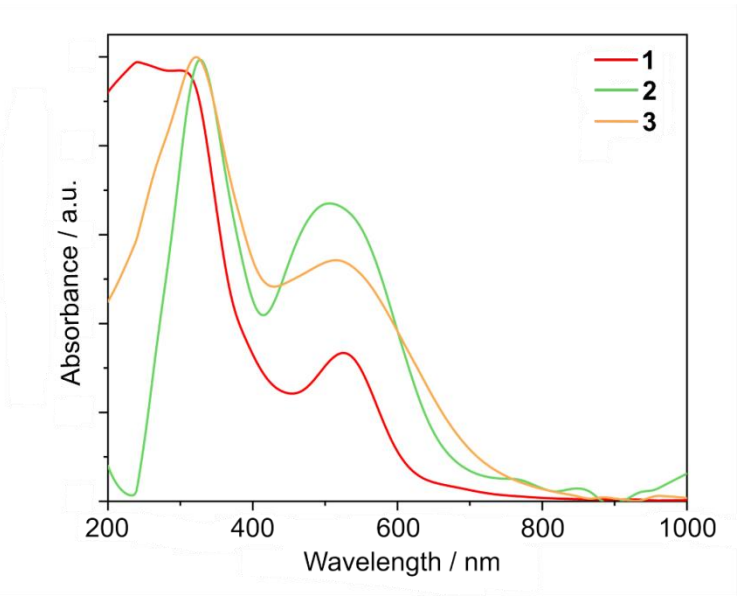

Fig. S2 Solid-state UV-vis-NIR absorption spectra for **1–3** measured in the 200–1000 nm range. Absorption bands of **2** and **3** in the 400–600 nm region are related to the sum of d-d electronic transitions within Co^{II} centres and electronic transitions of the W^{V}–Co^{II} metal-to-metal charge transfer (MMCT) character. In **1**, the MMCT transitions do not occur, thus the absorption band in the visible region is weaker and can be ascribed exclusively to the d-d electronic transitions of Co^{II} centres.

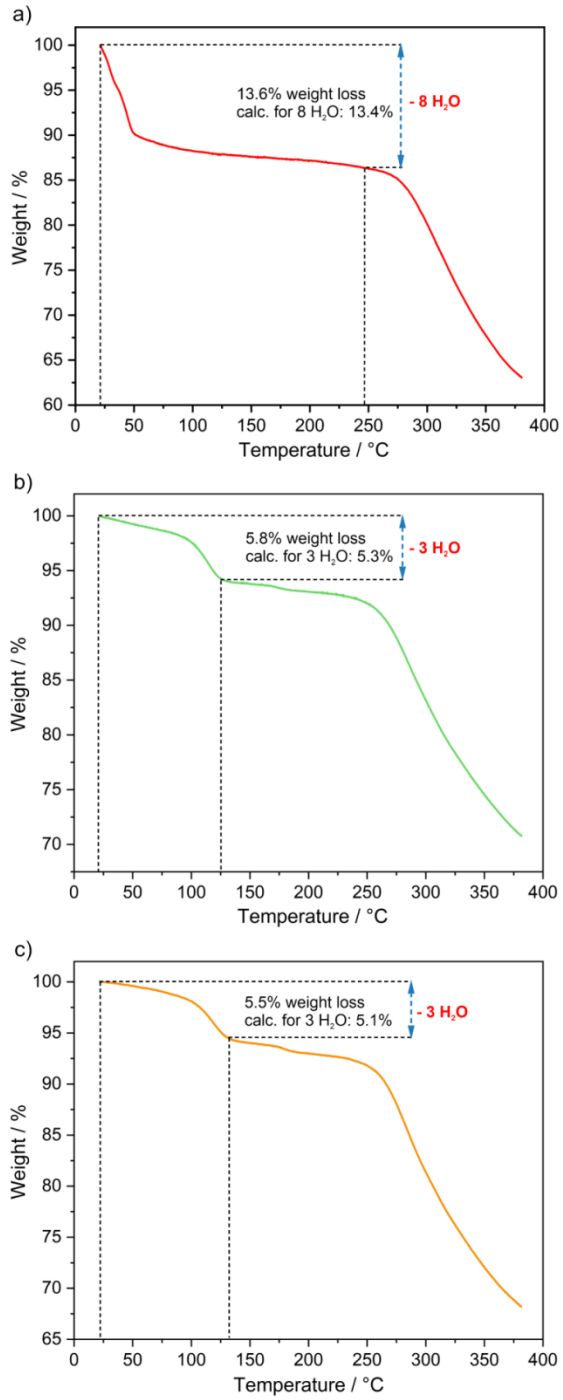

Fig. S3 Thermogravimetric (TG) curves for **1** (a), **2** (b), and **3** (c) obtained from measurements carried out under a nitrogen atmosphere in the 22–375 °C range. The weight losses indicating the removal of water molecules were depicted on the graph.

Comment to Fig. S3:

Upon heating of compound **1** from room temperature to ca. 50 °C, the sharp decrease of the sample weight is observed. This is due to the relatively easy removal of the most of existing water molecules of crystallization. However, further heating up to ca. 245 °C leads to the additional, gradual decrease of the sample mass. It can be ascribed to the removal of stronger bonded coordinated water molecules. The combined weight loss from room temperature to ca. 245 °C suits well the value calculated for the removal of all water molecules existing in **1**. Heating to temperatures above ca. 250 °C leads to the dramatic decrease of the sample mass which is presumably connected with the removal of the part of cyanido as well as organic ligands, and the resulting decomposition of the compound.

In the case of compounds **2** and **3**, upon heating from room temperature to 100 °C, the weaker gradual decrease of the sample weights is observed, followed by the sharp decrease of the sample masses in the 100–125 °C region. It can be ascribed to the removal of both crystallization and coordinated water molecules. Upon further heating, a rather small decrease of the sample mass is observed up to ca. 240 °C, after that a large decrease of the sample mass was detected. It can be presumably connected with the removal of the part of cyanido as well as organic ligands, and the resulting decomposition of the respective compound. The related weight losses ascribable to the removal of water molecules are in good agreement with the calculated ones.

Table S1 Crystal data and details of the structure refinement for compounds **1**–**3**.

	1	**2**	**3**
CCDC deposition no.	2083967	2083969	2083968
temperature / K	100(2)	100(2)	100(2)
formula	$Co_2W_1C_{30}H_{34}N_{18}O_8$	$Co_2W_1Cl_1C_{30}H_{20}N_{18}O_3$	$Co_2W_1Br_1C_{30}H_{20}N_{18}O_3$
formula weight / g·mol^{-1}	1076.46	1017.8	1062.26
radiation	Mo Kα (λ = 0.71073)	Mo Kα (λ = 0.71073)	Mo Kα (λ = 0.71073)
crystal system	monoclinic	monoclinic	monoclinic
space group	*C*2/c	*C*2/c	*C*2/c
***a* [Å]**	23.0143(13)	23.1568(13)	22.9910(15)
***b* [Å]**	12.8994(7)	12.8536(7)	12.8877(8)
***c* [Å]**	13.2566(7)	13.3618(7)	13.3285(9)
***β* [°]**	106.340(2)	109.9440(10)	108.6080(10)
volume [Å^3]	3776.5(4)	3738.6(4)	3742.8(4)
Z	4	4	4
ρ_{calc} / g·cm^{-3}	1.893	1.808	1.885
absorption coefficient / cm^{-1}	3.982	4.077	5.069
***F*(000)**	2128	1980	2052
crystal shape	plate	block	block
crystal colour	violet	red	red
crystal size / mm x mm x mm	0.45 x 0.1 x 0.05	0.42 x 0.17 x 0.14	0.28 x 0.19 x 0.15
θ range / deg	2.596 - 25.023	3.144 - 26.728	2.633 - 27.485
limiting indices	-27 < *h* < 27 -15 < *k* < 15 -15 < *l* < 15	-29 < *h* < 29 -16 < *k* < 14 -15 < *l* < 16	-28 < *h* < 29 -15 < *k* < 16 -17 < *l* < 17
reflections collected	15497	15497	15497
unique reflections	3325	3969	4298
R_{int}	0.0466	0.0259	0.0301
completeness / %	99.5	99.8	99.9
data/restraints/ parameters	3325/15/318	3969/30/318	4298/17/318
GOF on F^2	1.049	1.150	1.056
final *R* indices	*R_1 = 0.0310* [$I > 2\sigma(I)$] *wR_2 = 0.0801* (all data)	*R_1 = 0.0326* [$I > 2\sigma(I)$] wR_2 = 0.0842 (all data)	*R_1 = 0.0305* [$I > 2\sigma(I)$] wR_2 = 0.0680 (all data)
largest diff. peak/hole [e · Å^{-3}]	1.606/–0.851	1.885/–1.498	2.186/–1.951

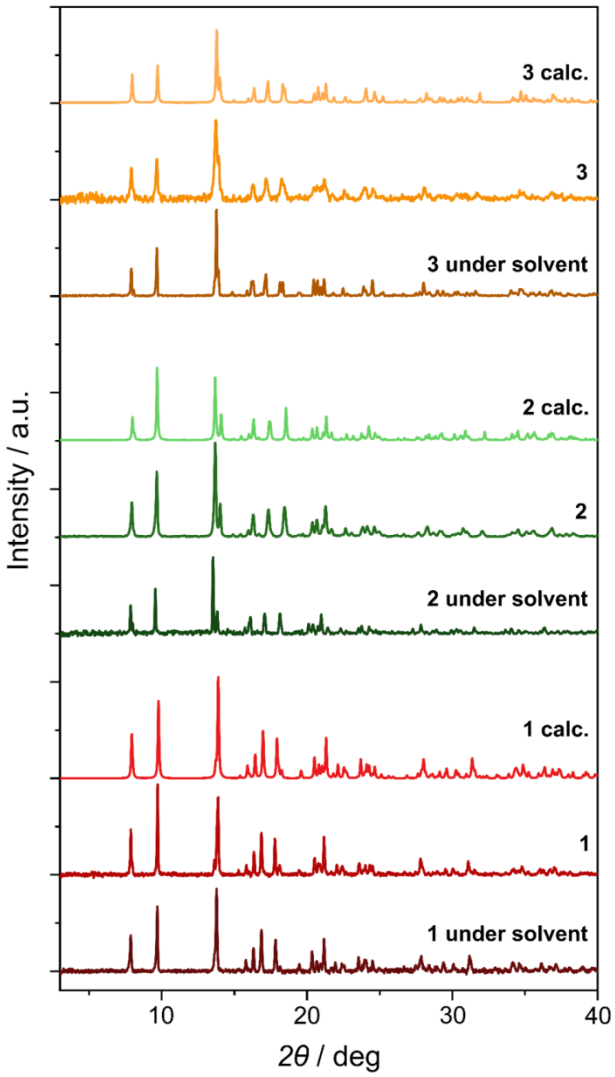

Fig. S4 Comparison of the experimental powder X-ray diffraction (P-XRD) patterns for bulk samples of **1**–**3** (measured both under solvent as well as after drying them on the air) with the respective P-XRD patterns calculated from the structural models obtained within the single-crystal X-ray diffraction (SC-XRD) experiment.

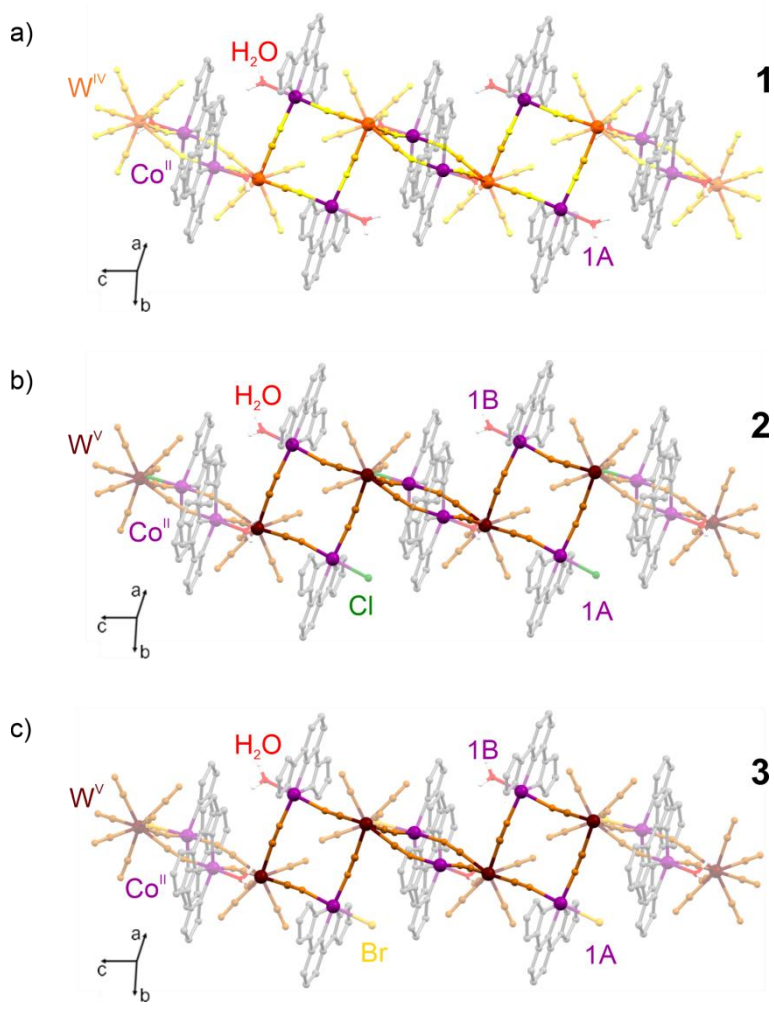

Fig. S5 Additional structural views showing the nearly perpendicular arrangement of neighbouring tetrametallic squares within the cyanido-bridged coordination chains of **1** (a), **2** (b), and **3** (c).

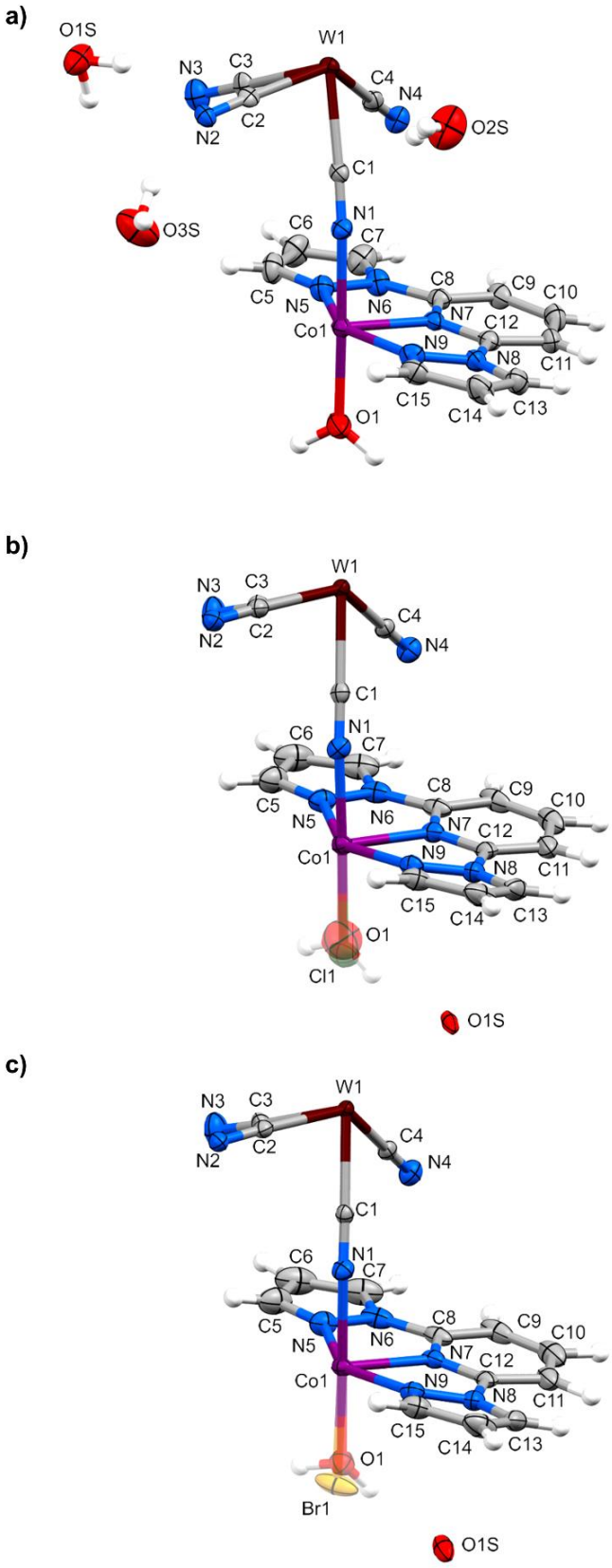

Fig. S6 Comparison of asymmetric units of **1** (a), **2** (b), and **3** (c) presented with the labelling scheme for all non-hydrogen atoms. Thermal ellipsoids are presented at the 50% probability level. Hydrogen atoms were shown as fixed-sized spheres with a 0.2 Å radius. The coordination sphere of Co(II) complexes in **2** and **3** are completed by halogen (Br, Cl) or aqua ligands, each of them revealing the 0.5 occupation.

Table S2 The results of the Continuous Shape Measures (CShM) analysis for eight-coordinated $[W^{IV/V}(CN)_8]^{3-/4-}$ anions present in the crystal structures of **1**–**3**. The $S_{geometry}$ value of 0 indicates an ideal reference geometry, the higher values represent the deviation from the idealized polyhedron of **BTPR** – bicapped trigonal prism, **SAPR** – square antiprism, and **TDD** – triangular dodecahedron.[S1,S2]

	S_{BTPR}	S_{SAPR}	S_{TDD}
1 (W^{IV})	1.799	0.893	0.831
2 (W^{V})	1.813	0.481	1.370
3 (W^{V})	1.778	0.688	1.067

Table S3. The results of the Continuous Shape Measures (CShM) analysis for six-coordinated Co^{II} complexes present in the structures of **1**–**3**. The $S_{geometry}$ value of 0 indicates an ideal reference geometry, the higher values represent the deviation from the idealized polyhedron of **PPY** – pentagonal pyramid, **OC** – octahedron, and **TPR** – trigonal prism.[S1,S2] In the structures of **2** and **3**, coordination spheres of Co^{II} centres including aqua (**A**) or halogen (Cl^- for **2** and Br^- for **3**) ligands (**B**) are considered.

	S_{PPY}	S_{OC}	S_{TPR}
1, Co1 (Co^{II})	22.394	1.995	10.979
2, Co1A (Co^{II})	21.316	2.213	11.188
2, Co1B (Co^{II})	21.564	2.308	11.715
3, Co1A (Co^{II})	21.409	2.124	11.379
3, Co1B (Co^{II})	21.618	2.649	11.801

References to Tables S2–S3:

S1 M. Llunell, D. Casanova, J. Cirera, J. Bofill, P. Alemany, S. Alvarez, M. Pinsky and D. Avnir, *SHAPE v. 2.1. Program for the Calculation of Continuous Shape Measures of Polygonal and Polyhedral Molecular Fragments,* University of Barcelona, Barcelona, Spain, 2013.

S2 D. Casanova, J. Cirera, M. Llunell, P. Alemany, D. Avnir and S. Alvarez, *J. Am. Chem. Soc.*, 2004, **126**, 1755.

Table S4 The selected metric parameters for compounds **1**–**3**, presented with the related visualization of the structural fragment.

	1	**2**	**3**
Co1-N1 / Å	2.109(4)	2.154(4)	2.145(3)
Co1-N2 / Å	2.051(4)	2.053(4)	2.049(3)
Co1-N5 / Å	2.137(5)	2.131(4)	2.121(4)
Co1-N7 / Å	2.098(4)	2.103(4)	2.101(3)
Co1-N9 / Å	2.147(4)	2.129(4)	2.130(4)
Co1-O1 / Å	2.136(4)	2.066(12)	2.062(8)
Co1-Cl1 / Å	-	2.442(4)	-
Co1-Br1 / Å	-	-	2.6098(12)
Co1-N1-C1 / °	160.2(4)	159.8(4)	159.9(3)
Co1-N2-C2 / °	170.7(4)	172.7 (4)	172.5(3)
N5-Co1-N7 / °	74.91(17)	74.78(17)	74.70(15)
N5-Co1-N9 / °	149.00(17)	147.61(17)	147.69(15)
N7-Co1-N9 / °	74.38(16)	74.38(16)	74.17(14)
W1-C1 / Å	2.160(5)	2.167(5)	2.163(4)
W1-C2 / Å	2.173(5)	2.174(5)	2.169(4)
W1-C3 / Å	2.142(5)	2.163(5)	2.158(4)
W1-C4 / Å	2.169(5)	2.160(5)	2.158(4)
W1-C1-N1 / °	176.9(4)	174.7(4)	174.8(3)
W1-C2-N2 / °	177.0(4)	176.6(4)	176.5(3)
W1-C3-N3 / °	179.2(5)	177.5(5)	177.6(4)
W1-C4-N4 / °	178.4(4)	178.4(4)	178.0(3)

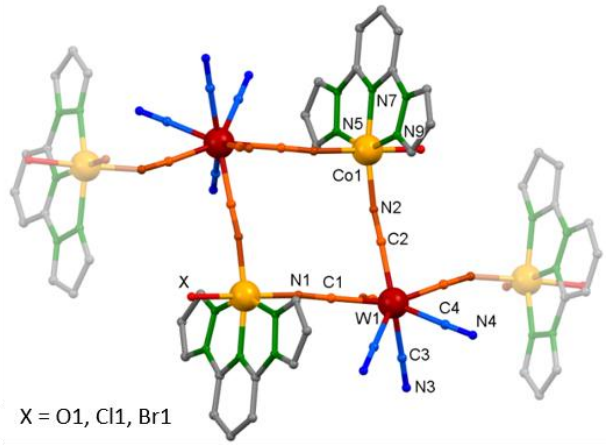

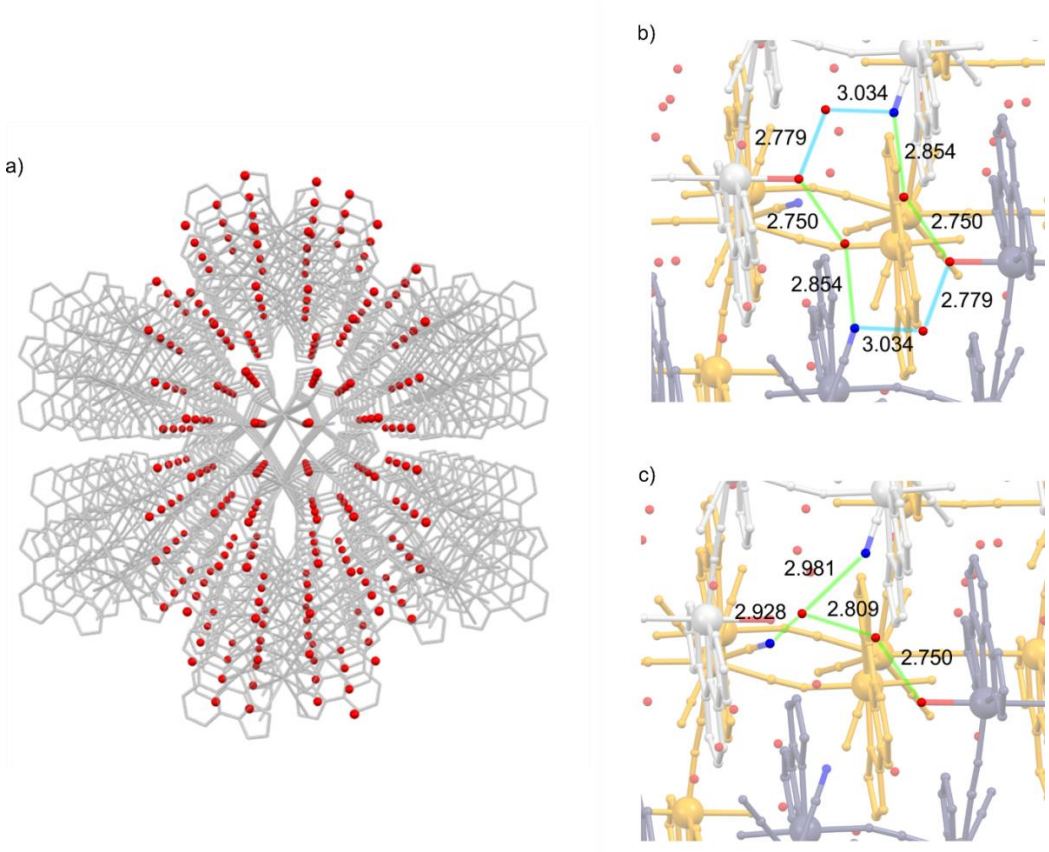

Fig. S7 Arrangement of water of crystallization within the crystal structure of **1** presented along *c* crystallographic axis (a) and two representative structural fragments showing the existing hydrogen bonding network (b and c). In the visualization of hydrogen bonding network, the O atoms of water molecules are shown as red balls, the N-atoms of cyanido ligands as deep blue balls, while interchain and intrachain H-bonds are represented by green and light blue colours, respectively. The N–O or O–O distances representing the hydrogen bonds were depicted in the figure.

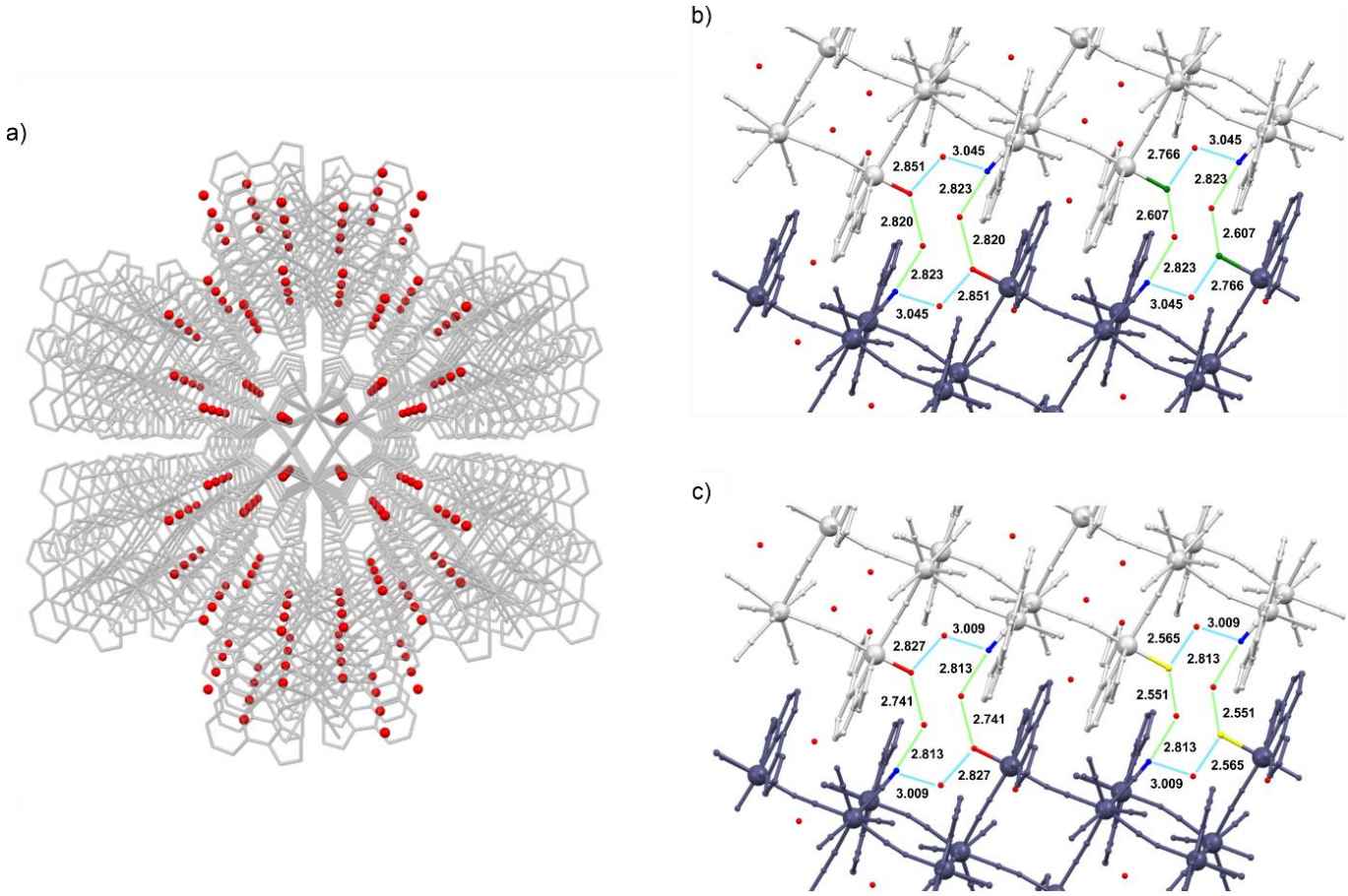

Fig. S8 Arrangement of water of crystallization within the crystal structure of **1** presented along *c* crystallographic axis (a) and two representative structural fragments showing the existing hydrogen bonding network (b and c). In the visualization of hydrogen bonding network, the O atoms of water molecules are shown as red balls, the N-atoms of cyanido ligands as deep blue balls, the Cl-atoms as dark green balls, the Br-atoms as yellow balls, while interchain and intrachain H-bonds are represented by green and light blue colours, respectively. The N–O/O–O/O-Cl/O-Br distances representing the hydrogen bonds were depicted in the figure.

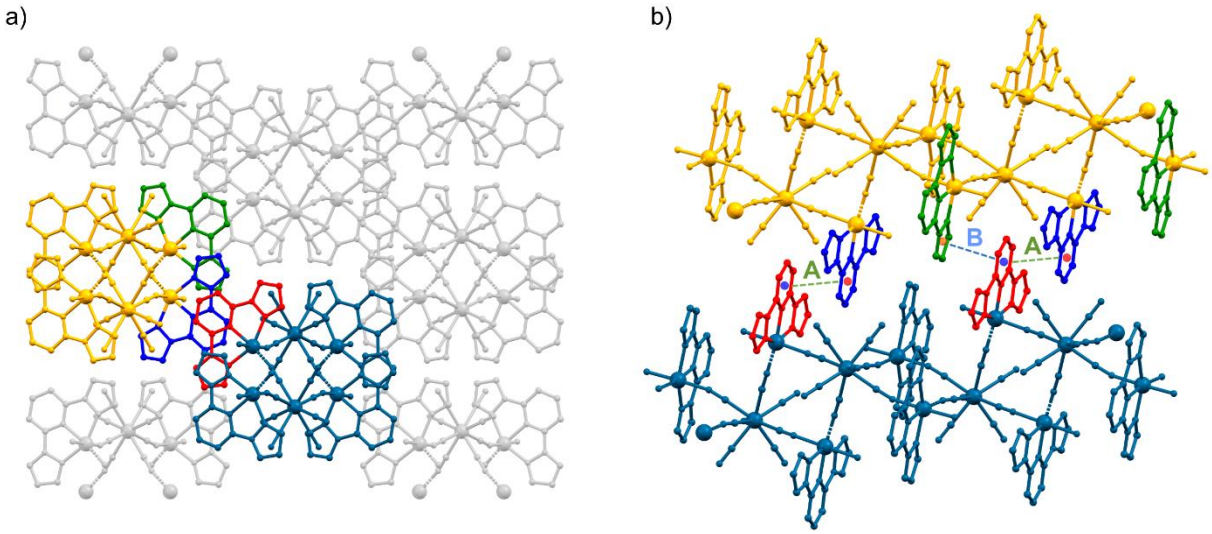

c)

Interaction	1	2	3
A / Å	3.75	4.077	3.985
B / Å	4.069	3.974	4.018

Fig. S9 The visualization of supramolecular π-π interactions involving aromatic rings of bpp ligands that exist in the crystal structure of **1**–**3** (presented on the example of **1**, a and b) together with the respective distances between aromatic rings for two types of observed interactions (c).

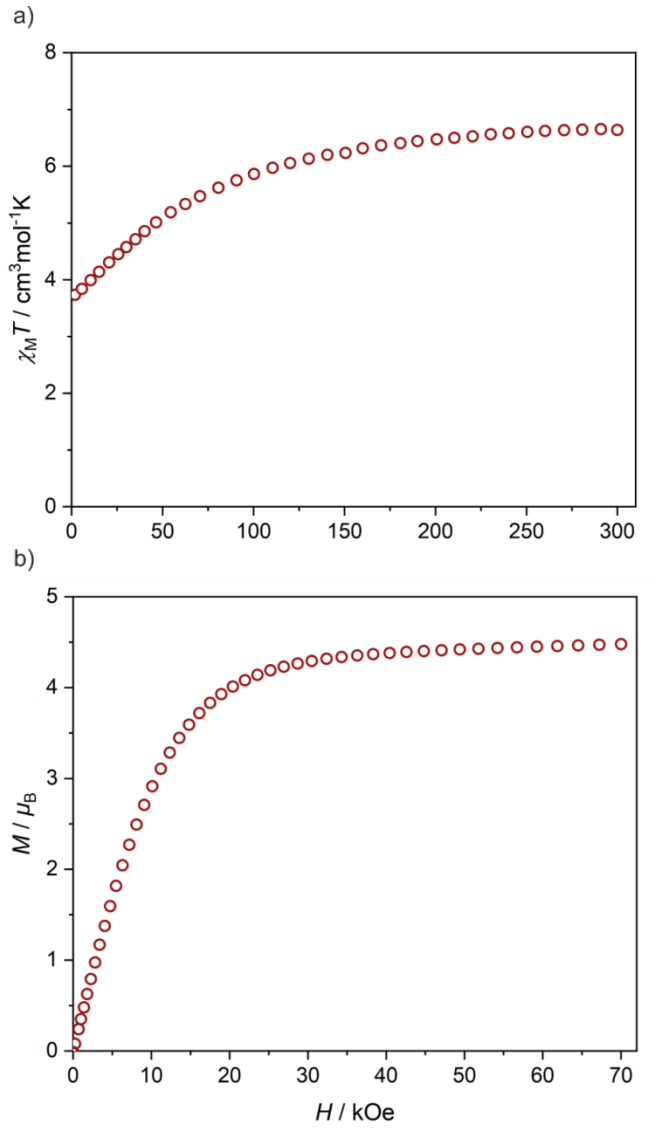

Fig. S10 Direct-current (*dc*) magnetic characteristics of **1** including the temperature dependence of the $\chi_M T$ product recorded in the 1.8–300 K range under H_{dc} = 1000 Oe (a), and the field dependence of the molar magnetization measured at T = 1.8 K (b).

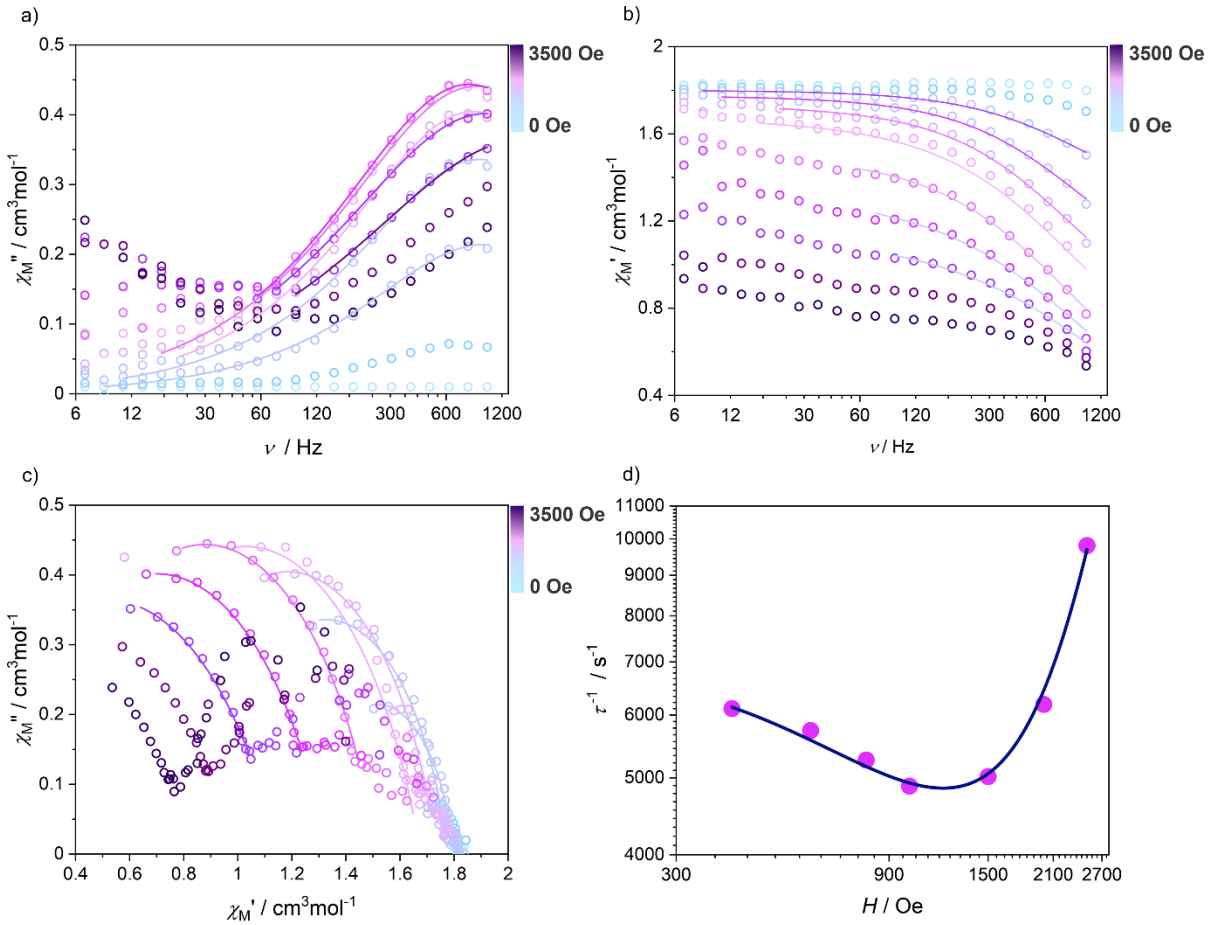

Fig. S11 Magnetic-field-variable alternate-current (*ac*) magnetic susceptibility characteristics of **1** performed at T = 1.8 K under H_{ac} = 2 Oe including the frequency dependences of the out-of-phase susceptibility, χ_M'' (a) and the frequency dependences of the in-phase susceptibility, χ_M' (b) at various *dc* magnetic fields, the related Cole-Cole (Argand) plots (c), and the field dependence of the resulting relaxation times (d). Solid lines in (a–c) represent the fitting following the generalized Debye model while the solid line in (d) represents the best-fit curve taking into account three magnetic relaxation pathways: QTM, Direct and Raman processes (see main text for details).

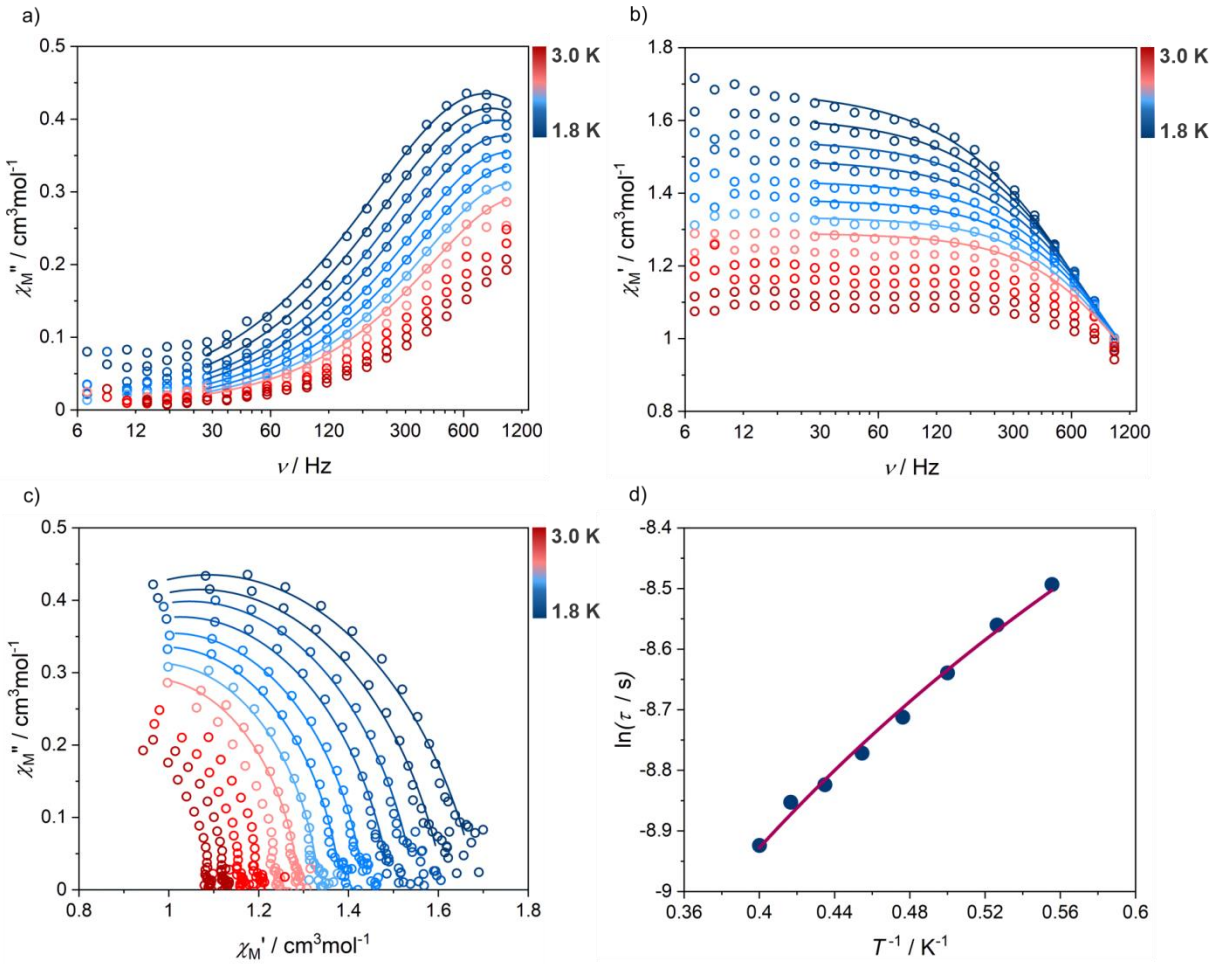

Fig. S12 Temperature-variable alternate-current (*ac*) magnetic susceptibility characteristics of **1** performed under H_{ac} = 2 Oe and H_{dc} = 1000 Oe including the frequency dependences of the out-of-phase susceptibility, χ_M'' (a) and the frequency dependences of the in-phase susceptibility, χ_M' (b) measured in the 1.8–3.0 K range, the related Cole-Cole (Argand) plots (c), and the temperature dependence of the resulting relaxation times (d). Solid lines in (a–c) represent the fitting following the generalized Debye model while the solid line in (d) represents the best-fit curve taking into account three magnetic relaxation pathways: QTM, Direct and Raman processes (see main text for details).

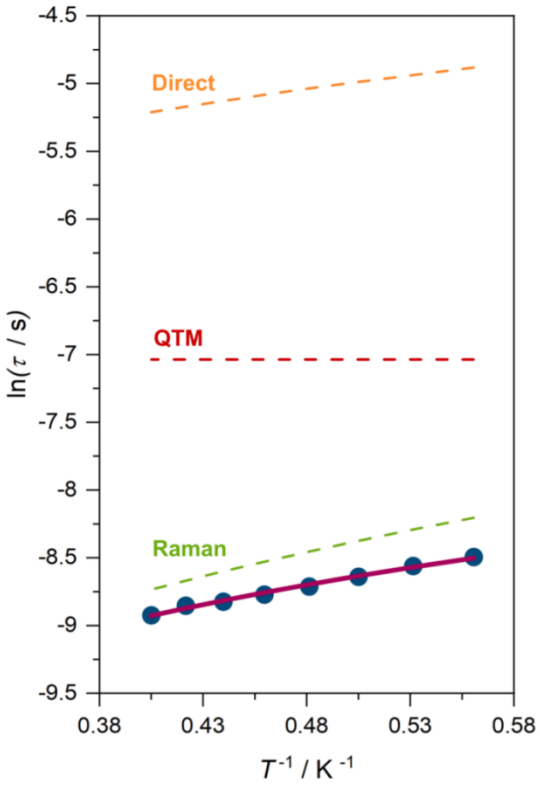

Fig. S13 Temperature dependence of magnetic relaxation time for **1** obtained from the *ac* measurements at the optimal *dc* field of 1000 Oe presented with the best-fit curves taking into account three relaxation processes (Direct, QTM, Raman). Blue circles represent the experimental data while the dark purple solid line shows the best-fit resulting from the combined contribution from three different relaxation routes: QTM, a field-induced direct process, and a two-phonon Raman relaxation process. The contributions from each of these processes are shown by coloured dotted lines.

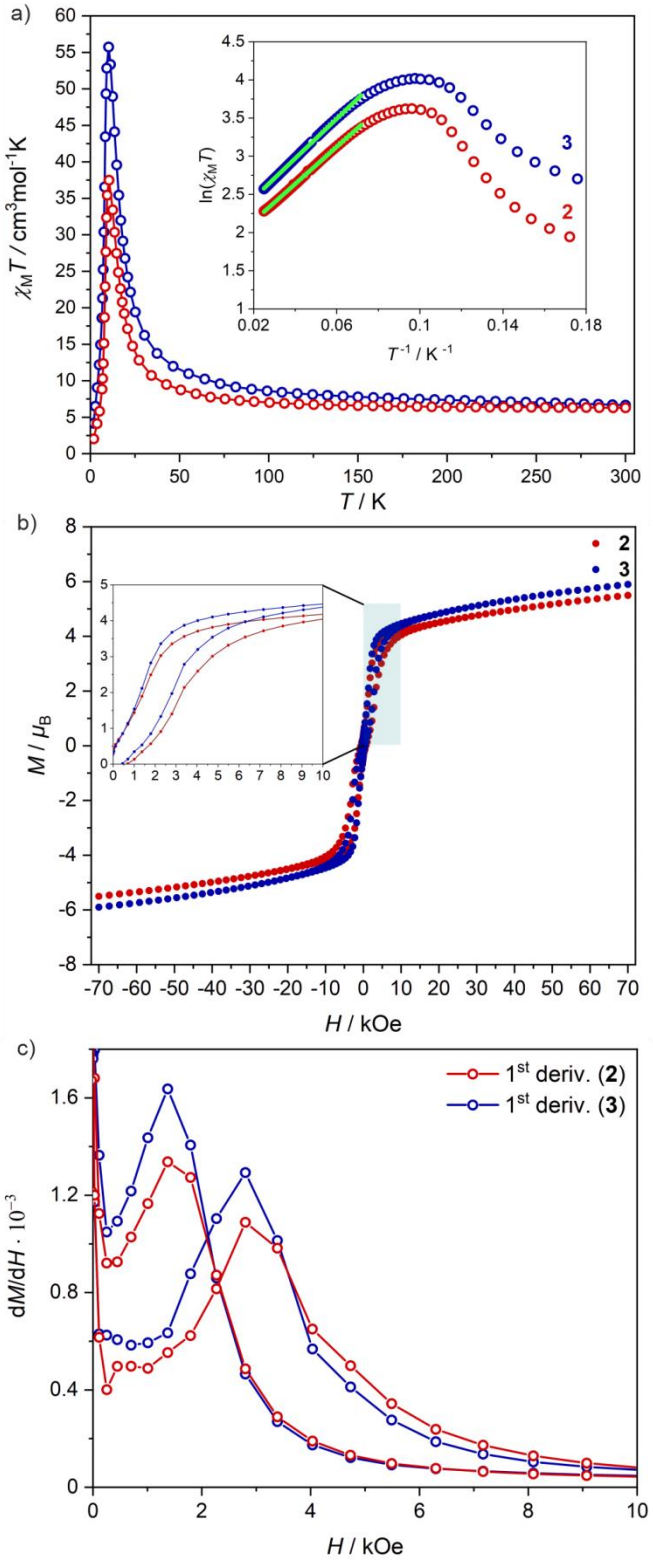

Fig. S14 Main direct-current (*dc*) magnetic characteristics of **2** and **3**: the temperature dependences of the magnetic susceptibility–temperature product, $\chi_M T$ gathered at H = 1 kOe (a), presented with the ln($\chi_M T$) versus inverse temperature, T^{-1} plots given in the inset (green lines represent the linear fitting for the limited 14–40 K range, see main text for details), the field dependences of magnetization, M at T = 1.8 K in the -70 to 70 kOe magnetic field (H) range (b), presented with the enlargement of the limited 0–10 kOe region in the inset, and the related dM/dH versus H plots (c).

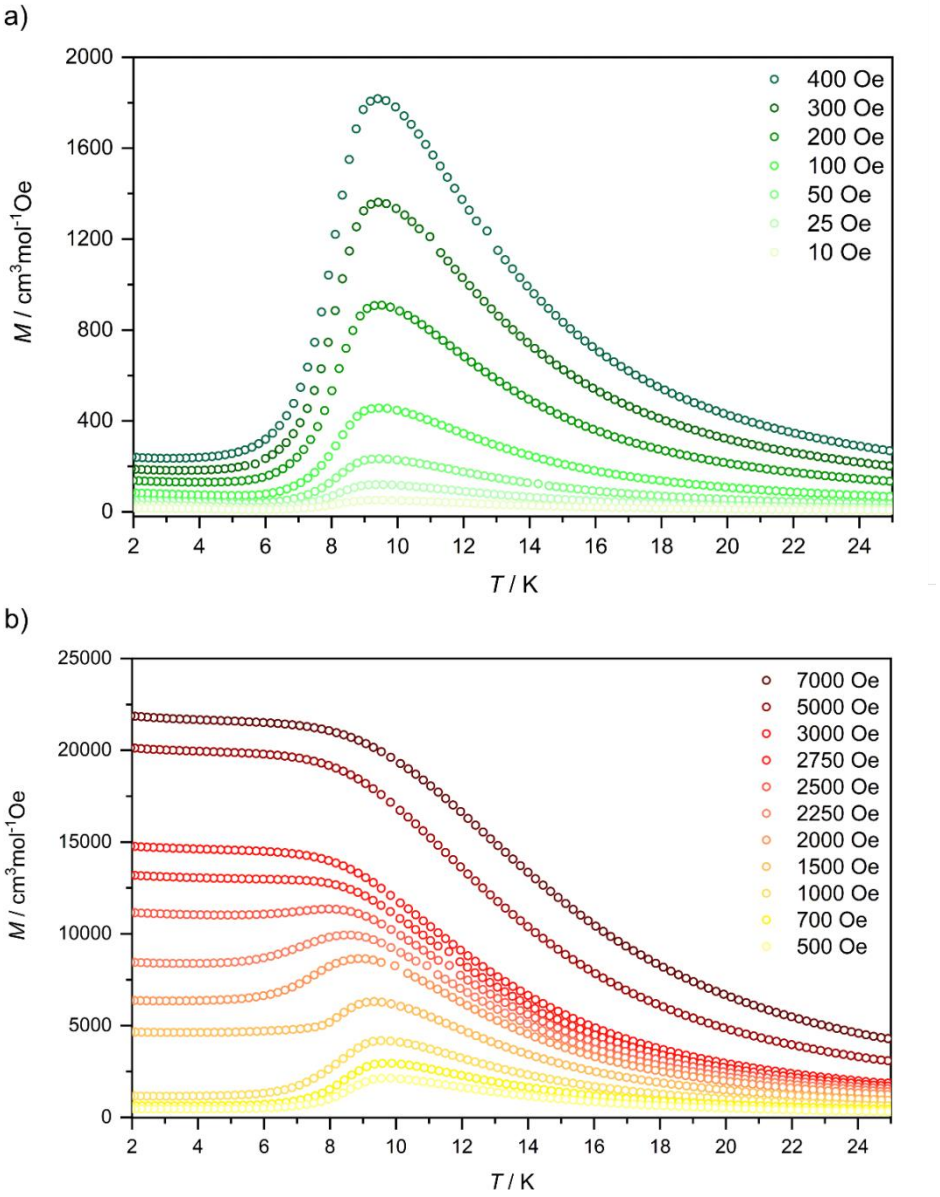

Fig. S15 Field-cooled magnetization curves for **2** recorded at various *dc* fields from the 10–7000 Oe range.

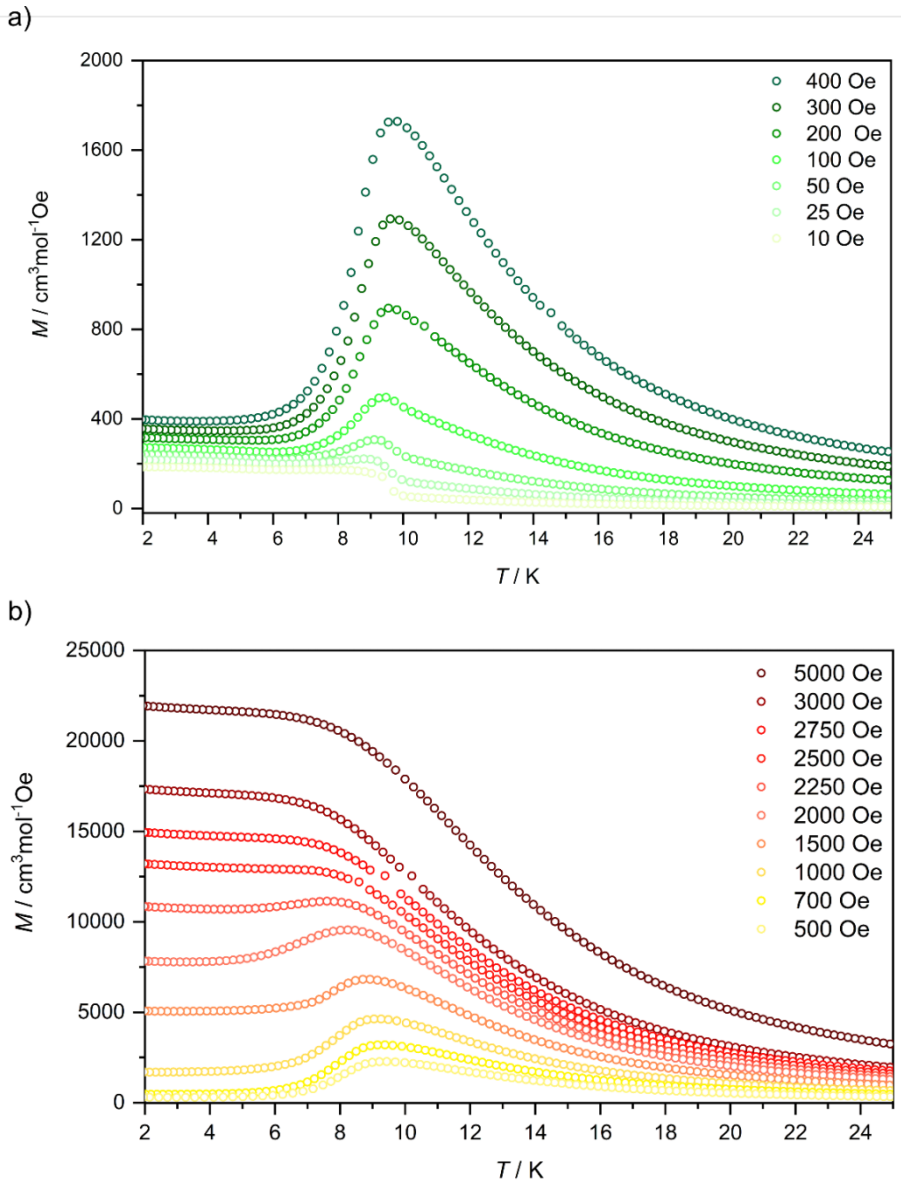

Fig. S16 Field-cooled magnetization curves for **3** recorded at various *dc* fields from the 10–5000 Oe range.

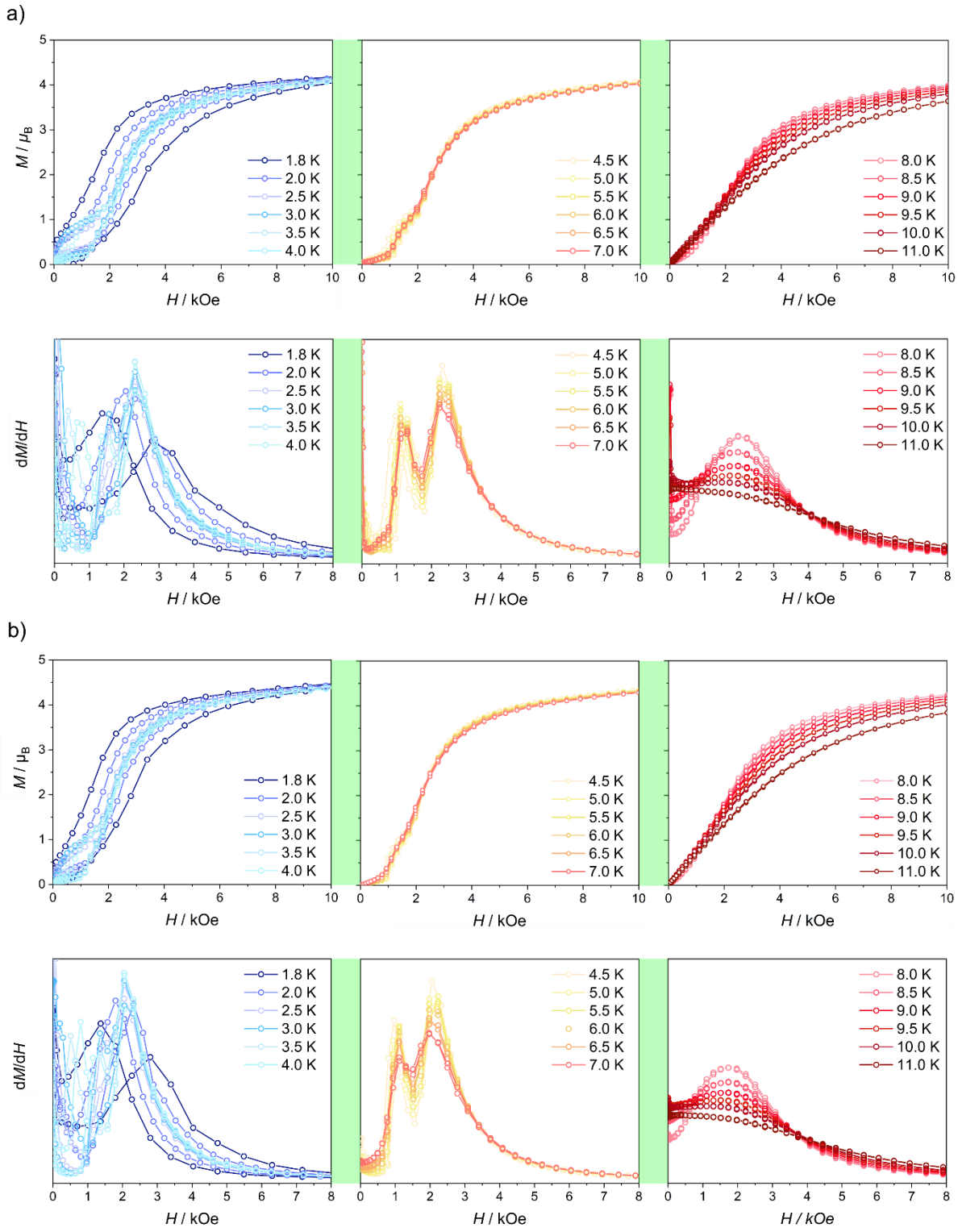

Fig. S17 The set of field dependences of magnetization gathered at various temperatures, presented together with the corresponding d*M*/d*H* versus *H* plots, for **2** (a) and **3** (b).

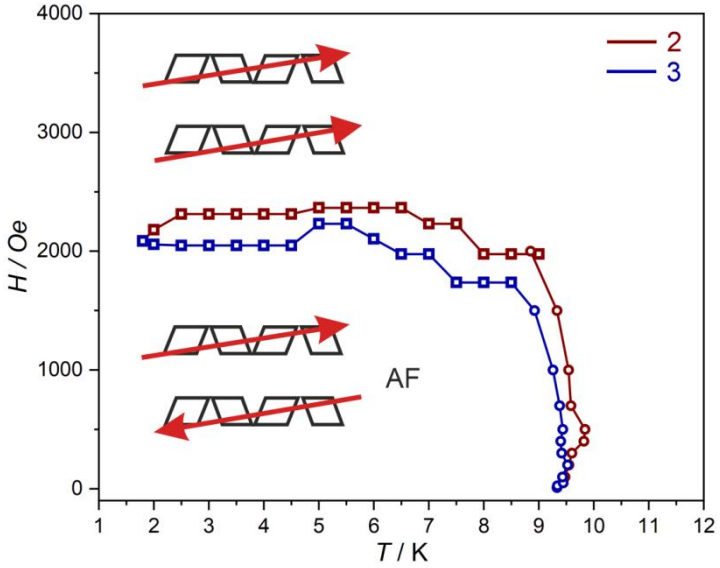

Fig. S18 Magnetic field-temperature, *H*–*T* phase diagram for **2** and **3** with the visualized antiferromagnetic phase realized by the antiparallel arrangement of magnetic moments resultant from the whole neighbouring chains (red arrows) and the field-induced ferromagnetic phase originating from the parallel alignment of these magnetic moments. The square points of the boundary between these magnetic phases were obtained from field dependences of magnetization, *M*(*H*) gathered at various temperatures (Fig. S17) while the circle points lying at higher temperatures were determined using the temperature dependences of magnetization gathered for various *dc* magnetic fields (Fig. S15 and Fig. S16 for **2** and **3**, respectively).

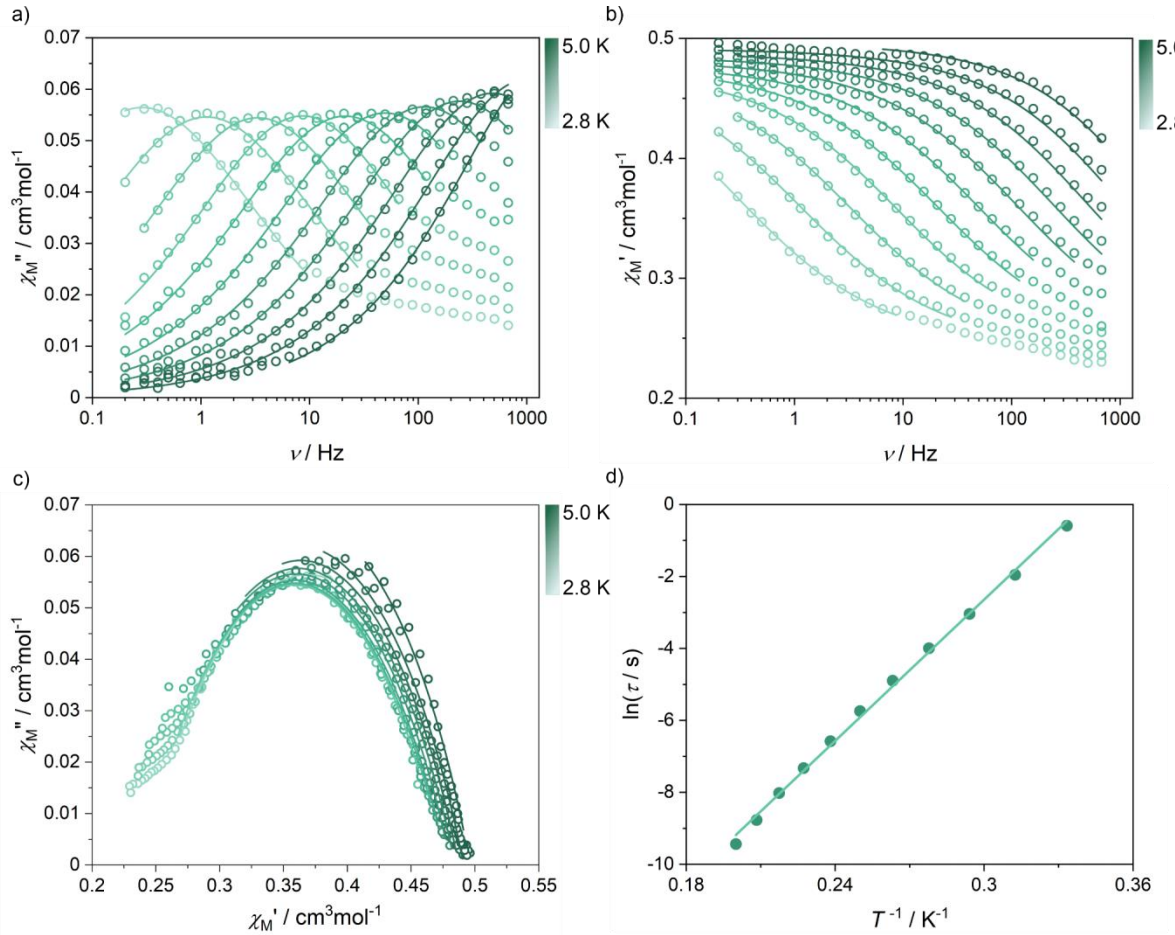

Fig. S19 Temperature-variable alternate-current (*ac*) magnetic susceptibility characteristics of **2** performed under H_{ac} = 2 Oe, H_{dc} = 1000 Oe, including the frequency dependences of the out-of-phase susceptibility, χ_M'' (a) and the frequency dependences of the in-phase susceptibility, χ_M' (b) measured in the 1.8–5.0 K range, the related Cole-Cole (Argand) plots (c), and the temperature dependence of the resulting relaxation times (d). Solid lines in (a–c) represent the fitting following the generalized Debye model while the solid line in (d) represents the linear fitting according to the Arrhenius-type process (see main text for details).

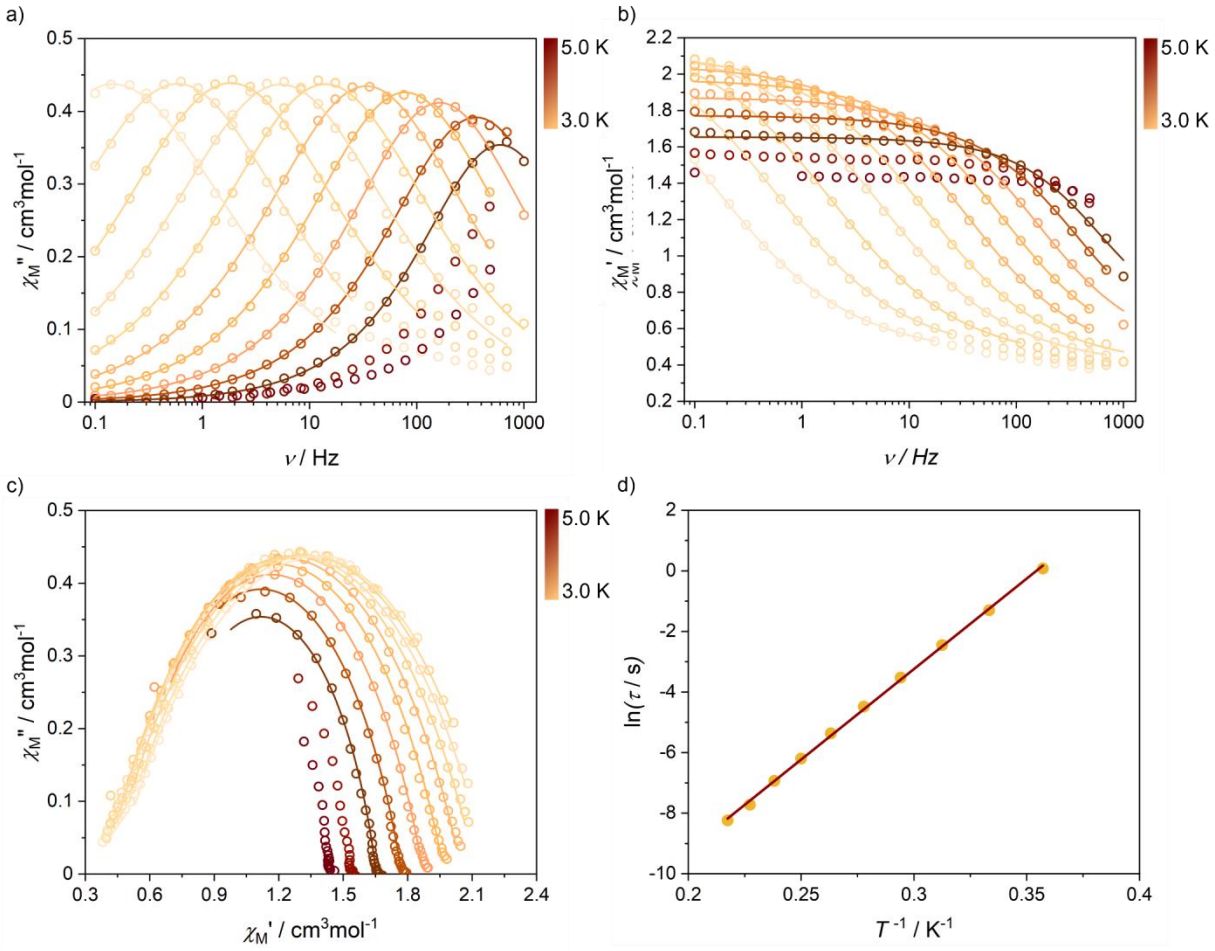

Fig. S20 Temperature-variable alternate-current (*ac*) magnetic susceptibility characteristics of **3** performed under H_{ac} = 2 Oe, H_{dc} = 1000 Oe, including the frequency dependences of the out-of-phase susceptibility, χ_M'' (a) and the frequency dependences of the in-phase susceptibility, χ_M' (b) measured in the 1.8–5.0 K range, the related Cole-Cole (Argand) plots (c), and the temperature dependence of the resulting relaxation times (d). Solid lines in (a–c) represent the fitting following the generalized Debye model while the solid line in (d) represents the linear fitting according to the Arrhenius-type process (see main text for details).

Table S5 Description of the basis sets for two models: **S** (small) and **L** (large) employed in the *ab initio* calculations of the Co^{II} crystal field effect and magnetic properties of **1**, **2**, and **3**.

model **S**	**L**
Co.ANO-RCC-VDZP 5S4P2D1F	Co.ANO-RCC-VTZP 6S5P3D2F1G
Ta.ANO-RCC-VDZ 7S6P4D2F	Ta.ANO-RCC-VDZ 7S6P4D2F
Cl.ANO-RCC-VDZ 4S3P	Cl.ANO-RCC-VDZP 4S3P1D
Br.ANO-RCC-VDZ 5S4P1D	Br.ANO-RCC-VDZP 5S4P2D
N.ANO-RCC-VDZ 3S2P	N.ANO-RCC-VDZP 3S2P1D (first coordination sphere) N.ANO-RCC-VDZ 3S2P (other)
O.ANO-RCC-VDZ 3S2P	O.ANO-RCC-VDZP 3S2P1D
C.ANO-RCC-VDZ 3S2P	C.ANO-RCC-VDZ 3S2P
H.ANO-RCC-VDZ 2S	H.ANO-RCC-VDZ 2S

Table S6 The energy splitting of six ground Kramers doublets (KDs) of the $^4T_{1g}$ multiplet (rising from the ^4F term), shown together with g_x, g_y, and g_z components of the pseudo-*g*-tensors in the basis of each KD, for Co(II) (Co1) complexes of **1**, obtained using the **S** and **L** *ab initio* models (Table S5).

KD	Co1 (compound **1**), model **S**				Co1 (compound **1**), model **L**			
	energy / cm^{-1}	g_x	g_y	g_z	energy / cm^{-1}	g_x	g_y	g_z
1	0	2.324	4.025	6.438	0	2.304	3.864	6.561
2	207.079	0.902	1.170	5.206	204.627	1.035	1.276	5.221
3	597.139	1.788	2.817	5.021	598.974	1.745	2.915	4.893
4	946.900	0.494	0.923	3.397	942.268	0.471	0.821	3.460
5	1119.377	0.748	1.904	3.465	1128.203	0.803	2.056	3.449
6	1226.576	0.765	0.861	3.542	1235.427	0.662	0.746	3.592

Table S7 The energy splitting of six ground Kramers doublets (KDs) of the $^4T_{1g}$ multiplet (rising from the ^4F term), shown together with g_x, g_y, and g_z components of the pseudo-*g*-tensors in the basis of each KD, for Co(II) (Co1A) complexes of **2**, obtained using the **S** and **L** *ab initio* models (Table S5).

KD	Co1A (compound **2**), model **S**				Co1A (compound **2**), model **L**			
	energy / cm^{-1}	g_x	g_y	g_z	energy / cm^{-1}	g_x	g_y	g_z
1	0	1.856	2.649	7.407	0	1.759	2.373	7.624
2	145.465	2.103	2.113	5.432	151.678	2.287	2.346	5.267
3	722.704	1.108	2.429	5.842	695.353	0.979	2.418	5.701
4	986.275	1.208	1.336	3.639	958.358	1.185	1.283	3.598
5	1535.551	4.035	3.348	1.161	1579.933	4.152	3.351	1.239
6	1657.354	0.147	0.209	4.221	1695.868	0.197	0.252	4.317

Table S8 The energy splitting of six ground Kramers doublets (KDs) of the $^4T_{1g}$ multiplet (rising from the ^4F term), shown together with g_x, g_y, and g_z components of the pseudo-*g*-tensors in the basis of each KD, for Co(II) (Co1B) complexes of **2**, obtained using the **S** and **L** *ab initio* models (Table S5).

KD	Co1B (compound **2**), model **S**				Co1B (compound **2**), model **L**			
	energy / cm^{-1}	g_x	g_y	g_z	energy / cm^{-1}	g_x	g_y	g_z
1	0	1.860	2.327	7.734	0	1.842	2.321	7.722
2	180.122	2.081	2.589	4.989	176.833	2.111	2.562	5.024
3	613.838	4.511	3.060	0.766	621.712	4.557	3.090	0.798
4	906.083	0.521	0.573	3.419	909.494	0.524	0.580	3.443
5	1451.179	1.009	1.920	5.215	1459.559	1.011	1.910	5.228
6	1566.673	1.286	1.413	4.018	1574.281	1.294	1.427	4.031

Table S9 The energy splitting of six ground Kramers doublets (KDs) of the $^4T_{1g}$ multiplet (rising from the ^4F term), shown together with g_x, g_y, and g_z components of the pseudo-*g*-tensors in the basis of each KD, for Co(II) (Co1A) complexes of **3**, obtained using the **S** and **L** *ab initio* models (Table S5).

KD	Co1A (compound **3**), model **S**				Co1A (compound **3**), model **L**			
	energy / cm^{-1}	g_x	g_y	g_z	energy / cm^{-1}	g_x	g_y	g_z
1	0	1.964	2.911	7.262	0	1.918	2.681	7.423
2	154.825	1.914	1.938	5.447	158.412	2.053	2.143	5.328
3	700.686	1.218	2.481	5.703	673.492	1.090	2.467	5.565
4	978.994	1.097	1.261	3.613	951.891	1.078	1.211	3.581
5	1420.822	3.787	3.310	1.057	1445.039	3.939	3.289	1.118
6	1546.152	0.055	0.129	4.098	1567.143	0.123	0.190	4.158

Table S10 The energy splitting of six ground Kramers doublets (KDs) of the $^4T_{1g}$ multiplet (rising from the ^4F term), shown together with g_x, g_y, and g_z components of the pseudo-*g*-tensors in the basis of each KD, for Co(II) (Co1B) complexes of **3**, obtained using the **S** and **L** *ab initio* models (Table S5).

KD	Co1B (compound **3**), model **S**				Co1B (compound **3**), model **L**			
	energy / cm^{-1}	g_x	g_y	g_z	energy / cm^{-1}	g_x	g_y	g_z
1	0	2.071	3.036	7.117	0	2.050	2.974	7.147
2	164.452	1.715	1.893	5.416	161.837	1.763	1.925	5.413
3	669.088	1.233	2.773	5.337	671.668	1.214	2.758	5.355
4	969.534	0.843	1.014	3.442	967.394	0.862	1.027	3.466
5	1320.798	0.861	2.185	4.481	1335.413	0.884	2.218	4.517
6	1452.203	0.918	0.953	3.833	1465.779	0.916	0.949	3.867

Table S11 *Ab initio* calculated (model **L**) zero-field splitting parameters and the related *g*-tensor components for Co(II) complexes of **1**–**3** determined for the full spin Hamiltonian (equation 1, below the table) for effective pseudo-spin S = 3/2 compared with the *g*-tensor components corresponding to the lowest-lying Kramers doublet of the $^4T_{1g}$ multiplet (Tables S6–S10, model **L**).[S3–S7]

	Co1 complex of **1**	Co1A complex of **2**	Co1B complex of **2**	Co2A complex of **3**	Co2B complex of **3**
full spin Hamiltonian for effective pseudo-spin S = 3/2					
g_x	2.852	2.025	1.996	2.013	2.004
g_y	2.525	2.309	2.262	2.343	2.368
g_z	1.869	2.871	2.927	2.870	2.838
D / cm^{-1}	98.391	66.691	77.539	71.875	75.266
E / cm^{-1}	–16.199	20.848	24.531	19.215	17.154
$\lvert E/D \rvert$	0.165	0.313	0.316	0.267	0.228
lowest-lying Kramers doublet of the $^4T_{1g}$ multiplet (pseudo-spin 1/2)					
g_x	2.304	1.759	1.842	1.918	2.050
g_y	3.864	2.373	2.321	2.681	2.974
g_z	6.561	7.624	7.722	7.423	7.147

Equation 1 (full spin Hamiltonian for S = 3/2, hyperfine interactions omitted):[S3]

$$H = \beta\left(g_z B_z S_z + g_x B_x S_x + g_y B_y S_y\right) + D\left[S_z^2 - \frac{1}{3}S(S+1)\right] + E(S_x^2 - S_y^2)$$

where β is the Bohr magneton, g_x, g_y, and g_z are the principal values of the electronic *g*-tensor, D is the axial ZFS (zero-field splitting) parameter, while E is the rhombic ZFS parameter.

S3 E. Y. Misochko, A. V. Akimov, D. V. Korchagin, J. Nehrkorn, M. Ozerov, A. V Palii, J. M. Clemente-Juan and S. M. Aldoshin, Purely Spectroscopic Determination of the Spin Hamiltonian Parameters in High-Spin Six-Coordinated Cobalt(II) Complexes with Large Zero-Field Splitting, *Inorg. Chem*., 2019, **58**, 16434–16444.

S4 E. Ferentinos, M. Xu, A. Grigoropoulos, I. Bratsos, C. P. Raptopoulou, V. Psycharis, S.-D. Jiang and P. Kyritsis, Field-induced slow relaxation of magnetization in the S = 3/2 octahedral complexes *trans*-[Co{$(OPPh_2)(EPPh_2)N$}$_2$$(dmf)_2$], [E = S, Se: effects of Co–Se vs. Co–S coordination, *Inorg. Chem. Front*., 2019, **6**, 1405–1414.

S5 M. Böhme and W. Plass, How to link theory and experiment for single-chain magnets beyond the Ising model: magnetic properties modeled from *ab initio* calculations of molecular fragments, *Chem. Sci*., 2019, **10**, 9189–9202.

S6 L. F. Chibotaru and L. Ungur, *Ab initio* calculation of anisotropic magnetic properties of complexes. I. Unique definition of pseudospin Hamiltonians and their derivation, *J. Chem. Phys.,* 2012, **137**, 064112.

S7 I. F. Galvam, M. Vacher, A. Alavi, C. Angeli, F. Aquilant, J. Autschbach, J. J. Bao, S. I. Bokarev, N. A. Bogdanov, R. K. Carlson, L. F. Chibotaru, J. Creutzberg, N. Dattani, M. G. Delcey, S. S. Dong, A. Dreuw, L. Freitag, L. M. Frutos, L. Gagliardi, F. Gendron, A. Giussani, L. Gonzalez, G. Grell, M. Guo, C. E. Hoyer, M. Johansson, S. Keller, S. Knecht, G. Kovacevic, E. Kallman, G. L. Manni, M. Lundberg, Y. Ma, S. Mai, J. P. Malhado, P. A. Malmqvist, P. Marquetand, S. A. Mewes, J. Norell, M. Olivucci, M. Oppel, Q. M. Phung, K. Perloot, F. Plasser, M. Reiher, A. M. Sand, L. Schapiro, P. Sharma, C. J. Stein, L. K. Sorensen, D. G. Truhlar, M. Ugandi, L. Ungur, A. Valentini, S. Vancoillie, V. Veryazov, O. Weser, T. A. Wesołowski, P.-O. Widmark, S. Wouters, A. Zech, J. P. Zobel and R. Lindh, OpenMolcas: From Source Code to Insight, *J. Chem. Theory Comput.*, 2019, **15**, 5925–5964.

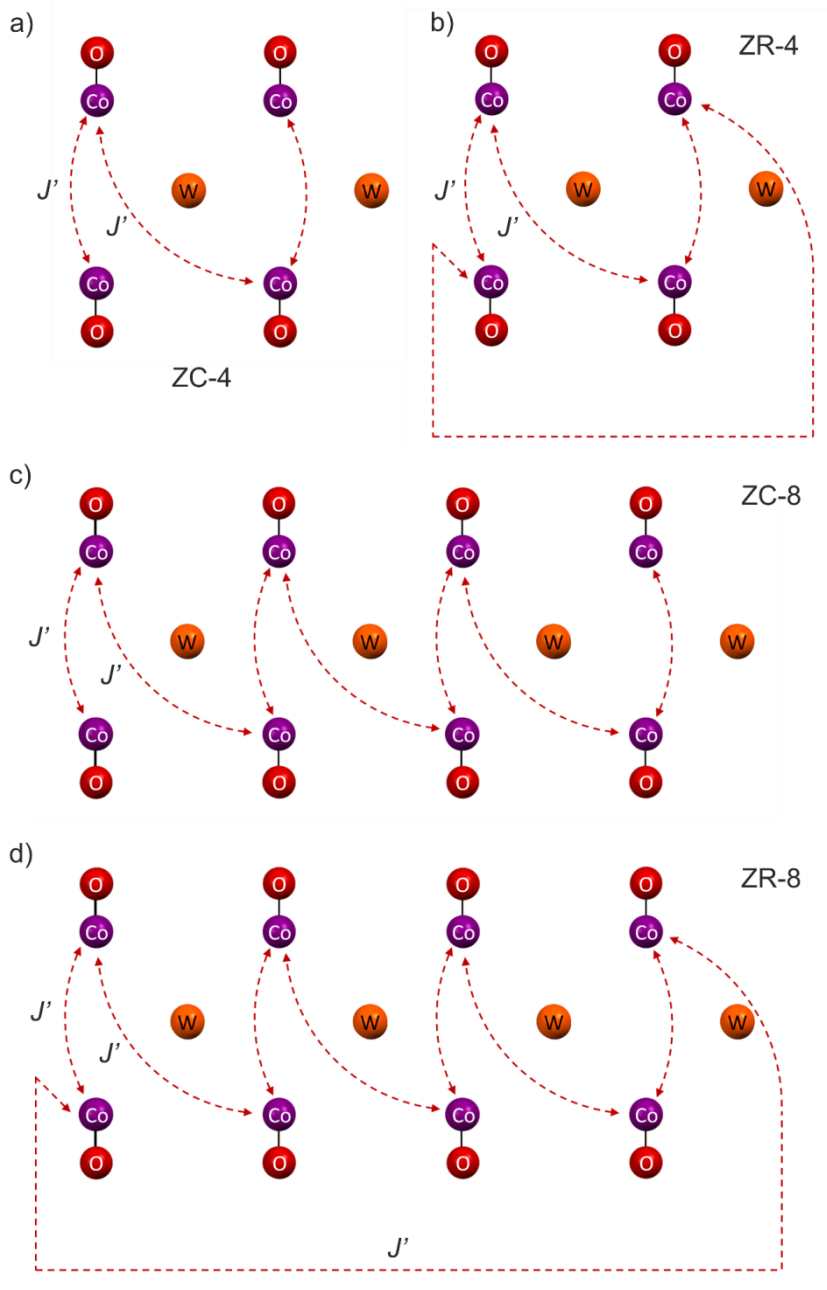

Fig. S21 Visualization of four additionally considered magneto-structural models for **1**, including a four-membered zig-zag chain (ZC-4) (a), a four-membered zig-zag ring (ZR-4) (b), an eight-membered zig-zag chains (ZC-8) (c), and an eight-membered zig-zag ring (ZR-8) (d). The *J'* stands for the intermetallic Co–Co magnetic coupling constant. Only the Co and W centres, together with the O-atoms attached to the Co centres, were shown while the other atoms of the coordination chains of **1** were omitted for clarity. The results of modelling of the magnetic properties of **1** obtained using these models are presented in Tables S13–S15, Fig. S26–S30, while the related best-fit curves to the experimental magnetic data are shown in Fig. S22–S23.

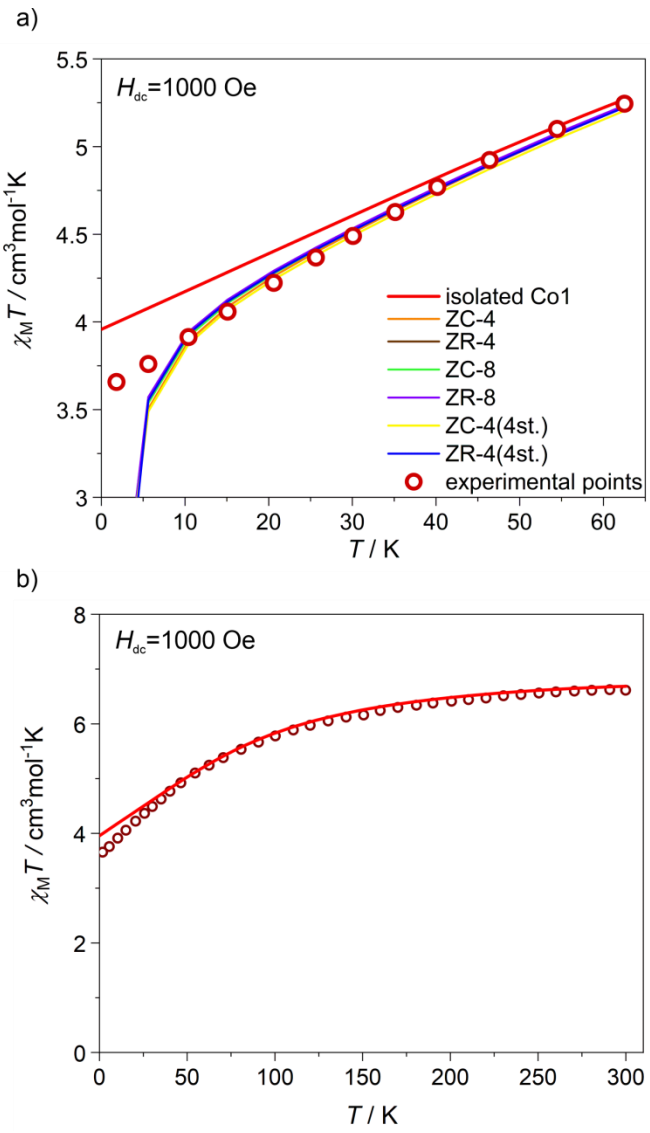

Fig. S22 Experimental temperature dependence of the $\chi_M T$ product under H_{dc} = 1000 Oe of **1** in the limited temperature range below 70 K, compared with the $\chi_M T(T)$ curve calculated for isolated Co1 complexes using the results of the *ab initio* calculations and the $\chi_M T(T)$ curves calculated using the results of the *ab initio* calculations combined with modelling the intrachain magnetic exchange (J' = –0.6 cm^{-1}) using the ZC-4, ZR-4, ZC-8, ZR-8, ZC-4(4st.), and ZR-4(4st.) magneto structural models (a), and the experimental $\chi_M T(T)$ curve in the broader 1.8–300 K range compared with the $\chi_M T(T)$ curve calculated for isolated Co1 complexes using the results of the *ab initio* calculations (b). The models labelled with the extension (4st.) represent the extended calculations employing four higher energy states of Co centre (Table S6), not only the ground one as for all other models labelled without this extension.

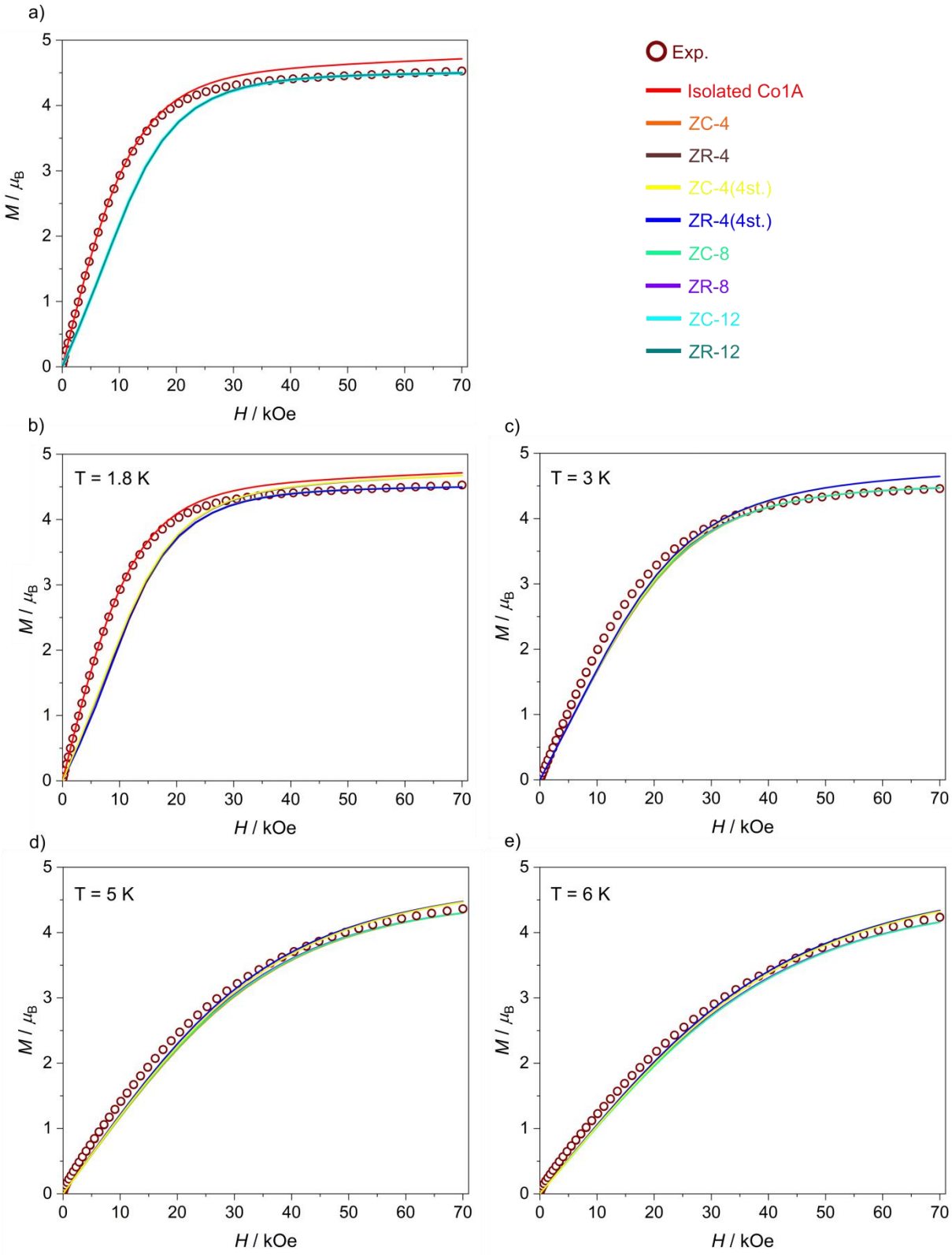

Fig. S23 Experimental field dependence of magnetization for **1** gathered at 1.8 K (a, b), 3 K (c), 5 K (d), and 6 K (e), and compared with the respective *M*(*H*) curves calculated for isolated Co1 complexes using the results of the *ab initio* calculations (red curve in b) or calculated using the results of the *ab initio* calculations combined with modelling the intrachain magnetic exchange (J' = –0.6 cm^{-1}) using the ZC-12 and ZR-12 magneto-structural models (a) or the ZC-4, ZR-4, ZC-8, ZR-8, ZC-4(4st.), and ZR-4(4st.) magneto structural models (b–e).

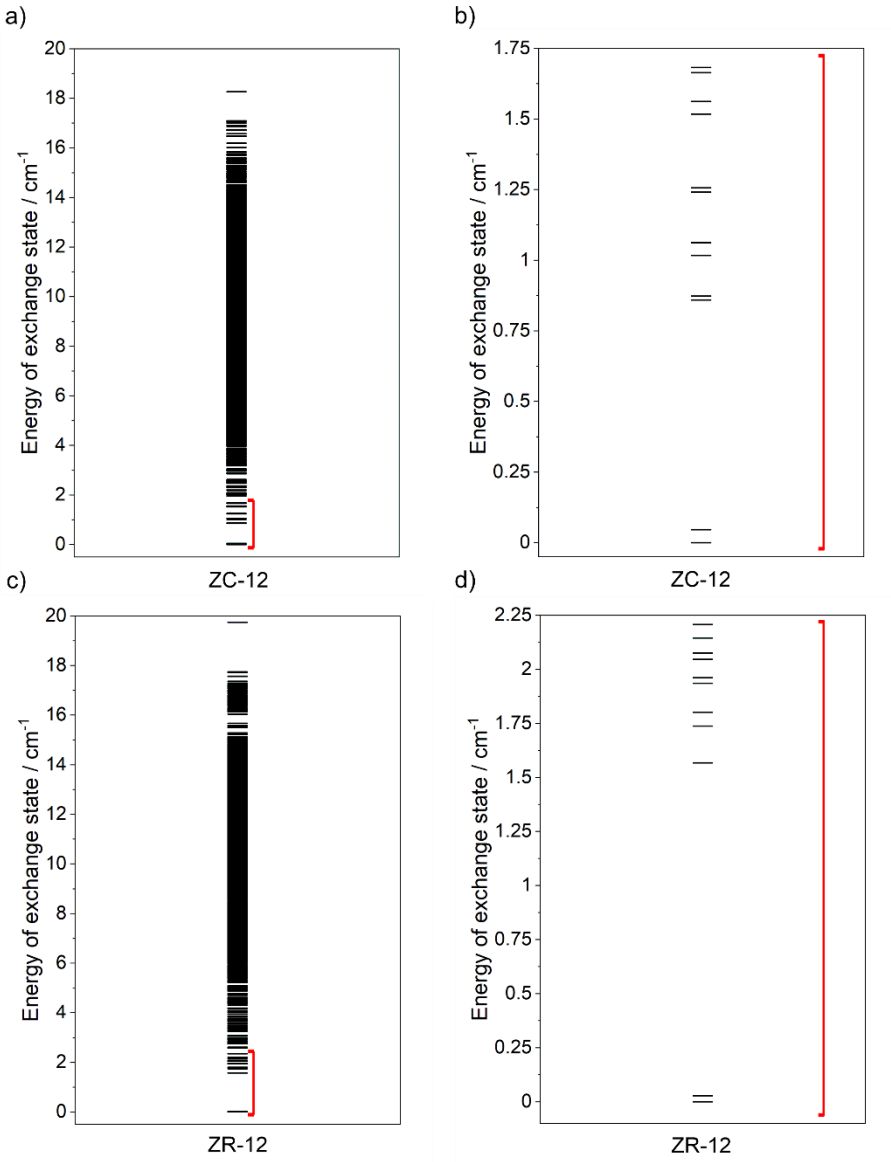

Fig. S24 The scheme of exchange states for **1** calculated using the results of the *ab initio* calculations (Table S6, Fig. 5–6) combined with the fitting of the exchange constant *J'* according to two different theoretical magneto-structural models of a twelve-membered zig-zag chain (model ZC-12, a and b, see also Fig. 6c) and a twelve-membered zig-zag ring (model ZR-12, c and d, see also Fig. 6c). The (a) and (c) parts show the full calculated pattern of 2048 exchange states while the (b) and (d) parts represent the enlarged view on the lowest energy regions.

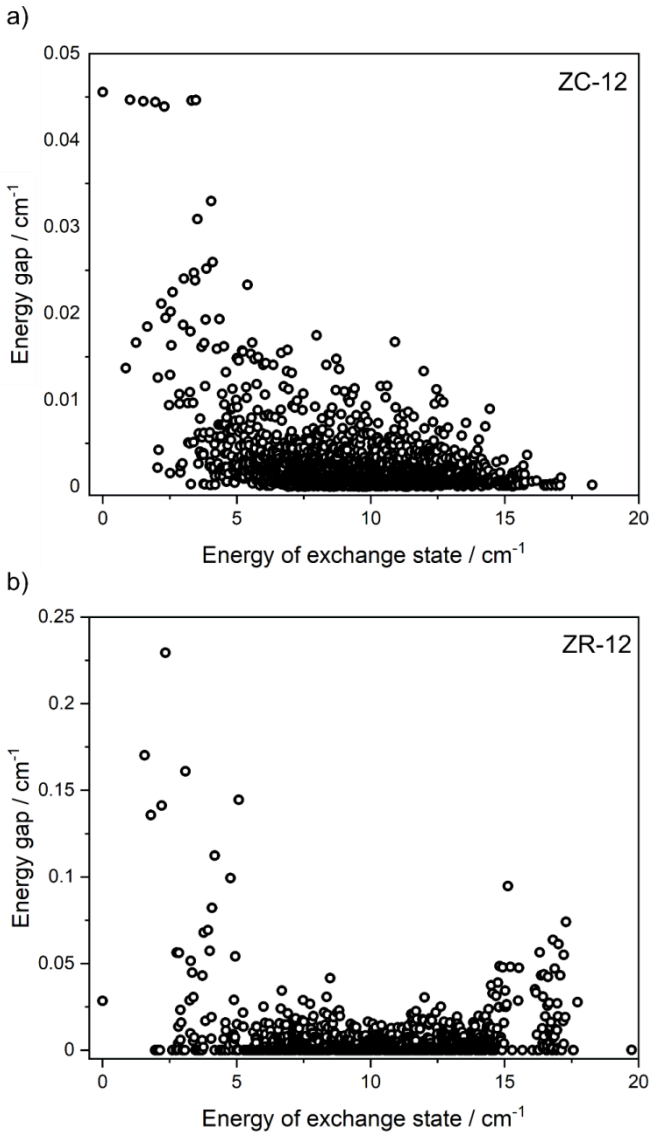

Fig. S25 The dependence between the average energy of the pairs of exchange states (pseudo-doublets) and the related energy gaps determined for **1** using the *ab initio* calculations combined with the fitting of the exchange constant according to two magneto-structural models, named ZC-12 (a) and ZR-12 (b). The models are visualized in Fig. 6 while the numerical data for the obtained exchange states are gathered in Tables 2 and S12.

Table S12 The extended set of selected parameters obtained from modelling the magnetic properties of **1** based on the results of the *ab initio* calculations combined with the fitting of the exchange constant *J*' according to two magneto-structural models, named ZC-12 and ZR-12 (Fig. 6). The presented results include the lists of 32 lowest lying exchange states (16 lowest lying pairs of exchange states, pseudo-doublets) and the respective energy gaps. The further, higher lying states are visualized in Fig. S24 and S25. The selected parameters are also shown in Table 2. The lowest lying pairs of states showing the relatively large energy gaps are emphasized by bold fonts.

No. of the pair of exchange states (pseudo-doublets)	Energy of a lower lying state / cm^{-1}	Energy of a higher lying state / cm^{-1}	Energy gap / cm^{-1}
model ZC-12 (Fig. 6c)			
1	**0.000**	**0.046**	**0.046**
2	0.859	0.873	0.014
3	1.017	1.062	0.045
4	1.241	1.257	0.017
5	1.517	1.562	0.045
6	1.664	1.682	0.018
7	1.961	2.005	0.044
8	2.044	2.047	0.003
9	2.053	2.066	0.013
10	2.089	2.093	0.004
11	2.184	2.205	0.021
12	2.302	2.346	0.044
13	2.346	2.366	0.020
14	2.477	2.486	0.009
15	2.514	2.516	0.002
16	2.519	2.532	0.013
model ZR-12 (Fig. 6c)			
1	0.000	0.028	0.028
2	1.567	1.737	0.170
3	1.801	1.936	0.136
4	1.961	1.961	0.0
5	2.046	2.046	0.0
6	2.075	20.75	0.0
7	2.145	2.145	0.0
8	2.207	2.348	0.141
9	**2.348**	**2.577**	**0.229**
10	2.610	2.610	0.0
11	2.749	2.749	0.0
12	2.770	2.826	0.056
13	2.826	2.830	0.004
14	2.830	2.833	0.003
15	2.833	2.846	0.013
16	2.846	2.847	0.001

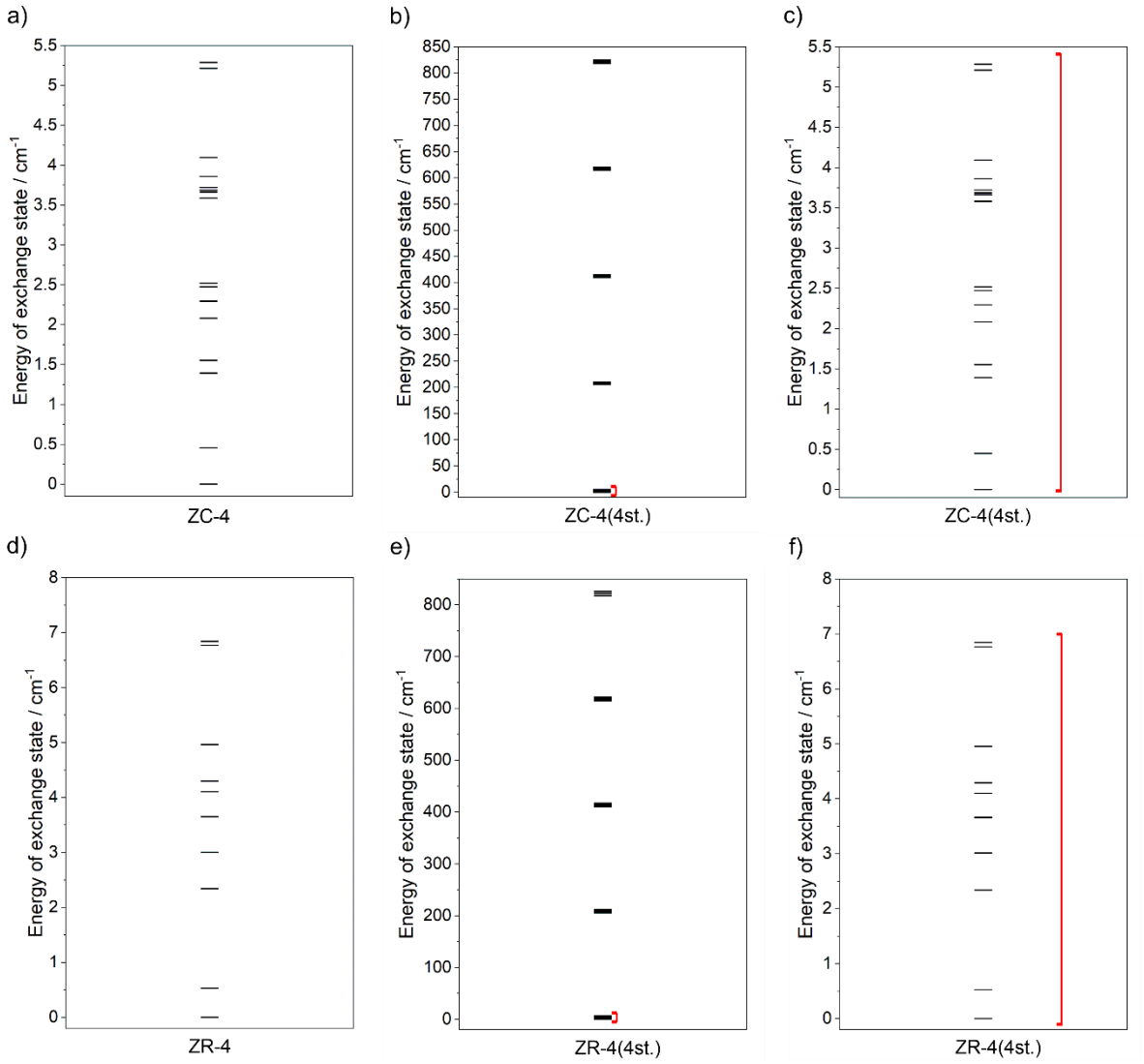

Fig. S26 The scheme of exchange states for **1** calculated using the results of the *ab initio* calculations (Table S6, Fig. 5–6) combined with the fitting of the exchange constant *J*' according to four different theoretical magneto-structural models of a four-membered zig-zag chain (model ZC-4, a, see also Fig. S21), a four-membered zig-zag chain with the extended set of employed *ab initio* energy states of Co centres to four higher-lying states (model ZC-4(4st.), b–c, see also Fig. S21), a four-membered zig-zag ring (model ZR-4, d, see also Fig. S21), and a four-membered zig-zag ring with the extended set of employed *ab initio* energy states of Co centres to four higher-lying states (model ZR-4(4st.), e–f, see also Fig. S21). The (a), (b), (d), and (e) parts show the full calculated pattern of exchange states while the (c) and (f) parts represent the enlarged view on the lowest energy regions within the indicated model.

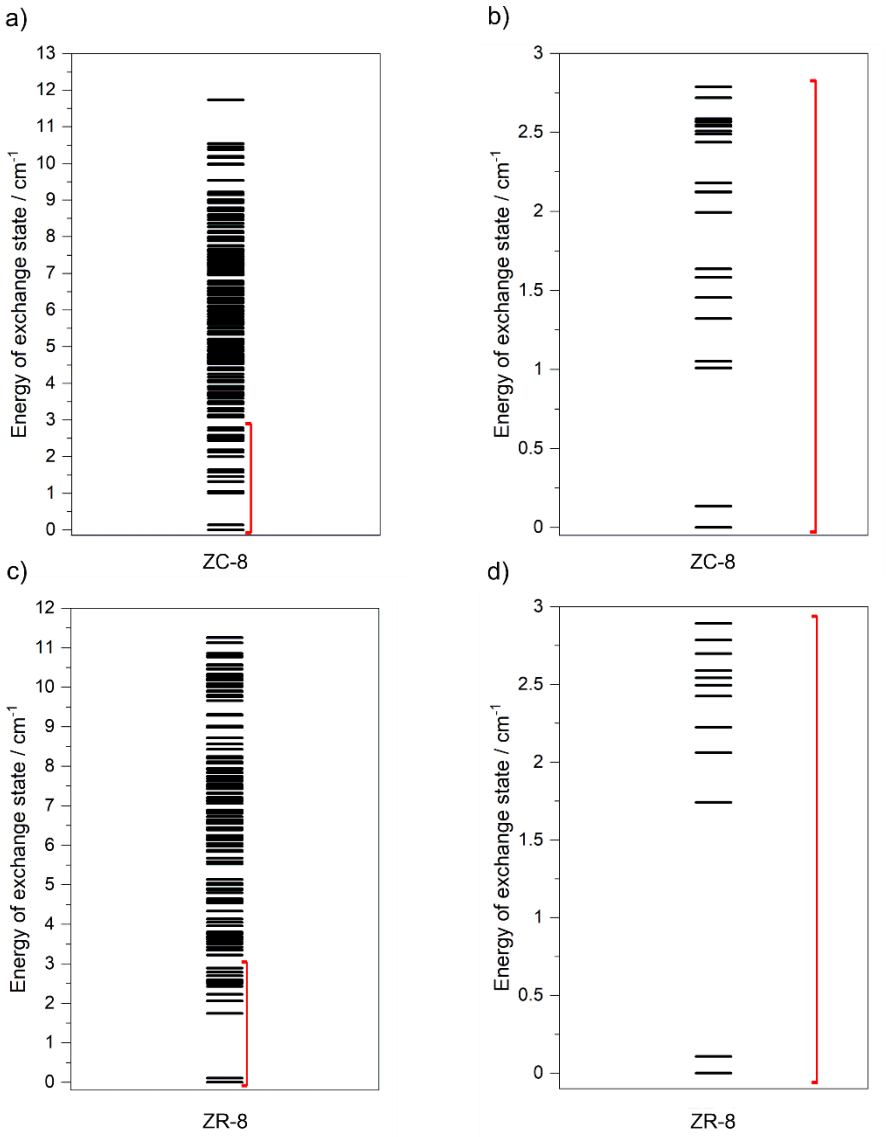

Fig. S27 The scheme of exchange states for **1** calculated using the results of the *ab initio* calculations (Table S6, Fig. 5–6) combined with the fitting of the exchange constant *J*' according to two different theoretical magneto-structural models of an eight-membered zig-zag chain (model ZC-8, a–b, see also Fig. S21) and an eight-membered zig-zag ring (model ZR-8, c–d, see also Fig. S21). The (a) and (c) parts show the full calculated pattern of exchange states while the (b) and (d) parts represent the enlarged view on the lowest energy regions within the indicated model.

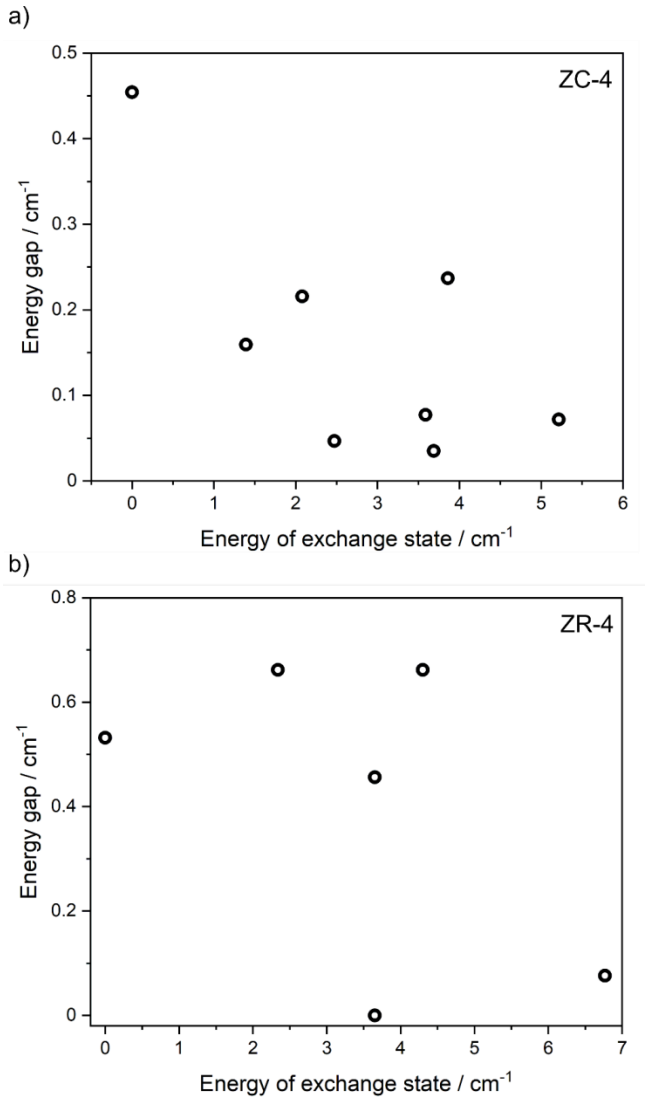

Fig. S28 The dependence between the average energy of the pairs of exchange states (pseudo-doublets) and the related energy gaps determined for **1** using the *ab initio* calculations combined with the fitting of the exchange constant according to two magneto-structural models, named ZC-4 (a) and ZR-4 (b). The models are visualized in Fig. S21 while the numerical data for the obtained exchange states are gathered in Table S13.

Table S13 The selected parameters obtained from modelling the magnetic properties of **1** based on the results of the *ab initio* calculations combined with the fitting of the exchange constant *J*' according to two magneto-structural models, named ZC-4 and ZR-4 (Fig. S21). The presented results include the lists of 16 lowest lying exchange states (8 lowest lying pairs of exchange states, pseudo-doublets) and the respective energy gaps. The lowest lying pairs of states showing the relatively large energy gaps are emphasized by bold fonts.

No. of the pair of exchange states (pseudo-doublets)	Energy of a lower lying state / cm^{-1}	Energy of a higher lying state / cm^{-1}	Energy gap / cm^{-1}
model ZC-4 (Fig. S21a)			
1	**0.000**	**0.454**	**0.454**
2	1.392	1.551	0.159
3	2.08	2.295	0.215
4	2.474	2.521	0.047
5	3.586	3.664	0.078
6	3.688	3.722	0.034
7	3.859	4.096	0.237
8	5.215	5.287	0.072
model ZR-4 (Fig. S21b)			
1	0.000	0.532	0.532
2	**2.338**	**3.000**	**0.662**
3	3.650	3.650	0.000
4	3.650	3.650	0.000
5	3.650	3.650	0.000
6	3.650	4.106	0.456
7	**4.299**	**4.961**	**0.662**
8	6.767	6.843	0.076

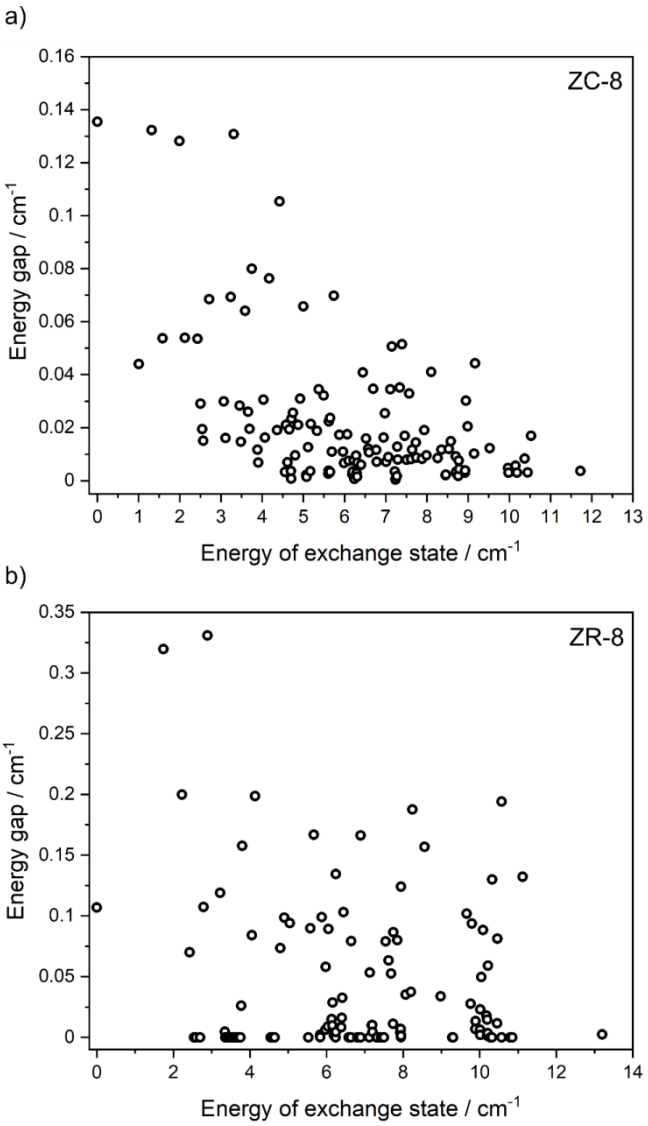

Fig. S29 The dependence between the average energy of the pairs of exchange states (pseudo-doublets) and the related energy gaps determined for **1** using the *ab initio* calculations combined with the fitting of the exchange constant according to two magneto-structural models, named ZC-8 (a) and ZR-8 (b). The models are visualized in Fig. S21 while the numerical data for the obtained exchange states are gathered in Tables S14.

Table S14 The selected parameters obtained from modelling the magnetic properties of **1** based on the results of the *ab initio* calculations combined with the fitting of the exchange constant *J*' according to two magneto-structural models, named ZC-8 and ZR-8 (Fig. S21). The presented results include the lists of 32 lowest lying exchange states (16 lowest lying pairs of exchange states, pseudo-doublets) and the respective energy gaps. The further, higher lying states are visualized in Fig. S27 and S29. The lowest lying pairs of states showing the relatively large energy gaps are emphasized by bold fonts.

No. of the pair of exchange states (pseudo-doublets)	Energy of a lower lying state / cm^{-1}	Energy of a higher lying state / cm^{-1}	Energy gap / cm^{-1}
model ZC-8 (Fig. S21c)			
1	**0.000**	**0.135**	**0.135**
2	1.008	1.052	0.044
3	1.322	1.454	0.132
4	1.582	1.635	0.053
5	1.993	2.121	0.128
6	2.125	2.179	0.054
7	2.436	2.489	0.053
8	2.508	2.537	0.029
9	2.548	2.567	0.019
10	2.571	2.586	0.015
11	2.718	2.787	0.069
12	3.072	3.102	0.030
13	3.115	3.131	0.016
14	3.241	3.31	0.070
15	3.312	3.442	0.130
16	3.457	3.485	0.028
model ZR-8 (Fig. S21d)			
1	0.000	0.107	0.107
2	1.742	2.061	0.319
3	2.224	2.424	0.200
4	2.424	2.494	0.070
5	2.541	2.541	0.000
6	2.589	2.589	0.000
7	2.697	2.697	0.000
8	2.785	2.892	0.107
9	**2.892**	**3.223**	**0.331**
10	3.223	3.342	0.119
11	3.342	3.347	0.005
12	3.355	3.355	0.0
13	3.420	3.420	0.0
14	3.502	3.502	0.0
15	3.568	3.568	0.0
16	3.623	3.623	0.0

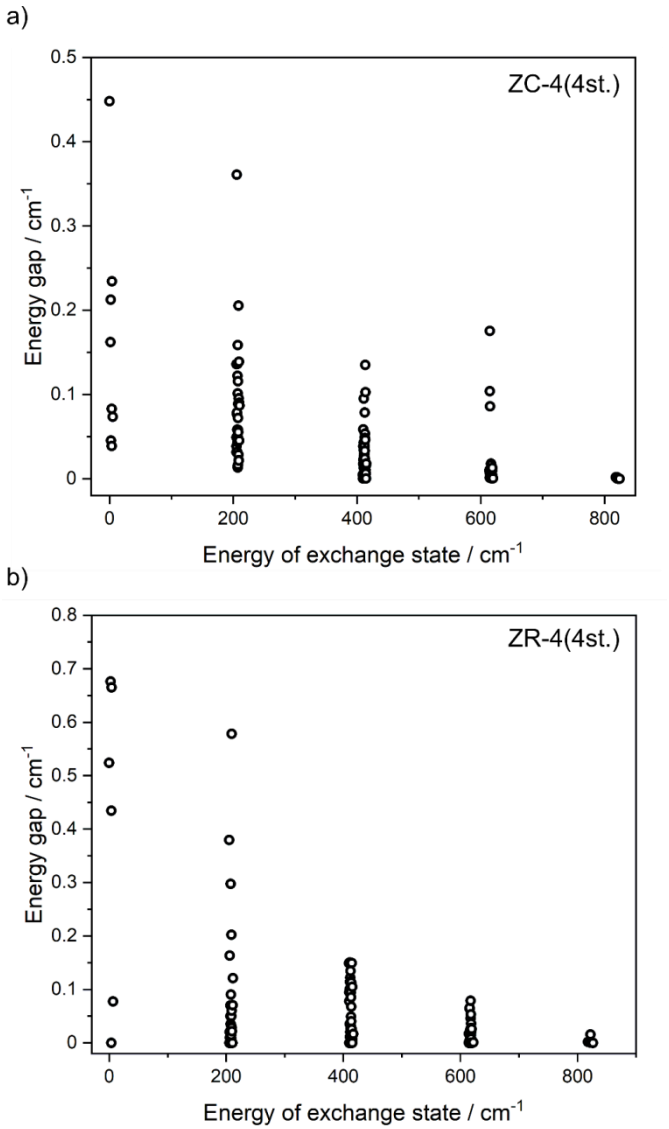

Fig. S30 The dependence between the average energy of the pairs of exchange states (pseudo-doublets) and the related energy gaps determined for **1** using the *ab initio* calculations combined with the fitting of the exchange constant according to two magneto-structural models, named ZC-4(4st.) (a) and ZR-4(4st.) (b). The models are visualized in Fig. S21 while the numerical data for the obtained exchange states are gathered in Table S15. The labels (4st.) represent the extended calculations employing four higher energy states of each Co centre.

Table S15 The selected parameters obtained from modelling the magnetic properties of **1** based on the results of the *ab initio* calculations combined with the fitting of the exchange constant *J*' according to two magneto-structural models, named ZC-4(4st.) and ZR-4(4st.) (Fig. S21). The presented results include the lists of 32 lowest lying exchange states (16 lowest lying pairs of exchange states, pseudo-doublets) and the respective energy gaps. The further, higher lying states are visualized in Fig. S26 and S30. The lowest lying pairs of states showing the relatively large energy gaps are emphasized by bold fonts. The labels (4st.) represent the extended calculations employing four higher energy states of each Co centre.

No. of the pair of exchange states (pseudo-doublets)	Energy of a lower lying state / cm^{-1}	Energy of a higher lying state / cm^{-1}	Energy gap / cm^{-1}
model ZC-4(4st.) (Fig. S21a)			
1	**0.000**	**0.448**	**0.448**
2	1.392	1.554	0.162
3	2.081	2.294	0.213
4	2.472	2.517	0.045
5	3.58	3.663	0.083
6	3.686	3.725	0.039
7	3.859	4.093	0.234
8	5.211	5.285	0.074
9	205.088	205.224	0.136
10	205.342	205.380	0.038
11	205.386	205.435	0.049
12	205.450	205.481	0.031
13	205.491	205.852	0.361
14	205.936	206.012	0.076
15	206.207	206.286	0.079
16	206.537	206.595	0.058
model ZR-4(4st.) (Fig. S21b)			
1	0.000	0.524	0.524
2	**2.338**	**3.014**	**0.676**
3	3.653	3.653	0.000
4	3.658	3.658	0.000
5	3.661	3.661	0.000
6	3.667	4.101	0.434
7	4.290	4.956	0.666
8	6.764	6.842	0.078
9	205.261	205.641	0.380
10	205.712	205.712	0.000
11	205.928	206.091	0.163
12	206.091	206.111	0.020
13	206.248	206.258	0.010
14	206.421	206.421	0.000
15	206.550	206.550	0.000
16	207.174	207.244	0.070

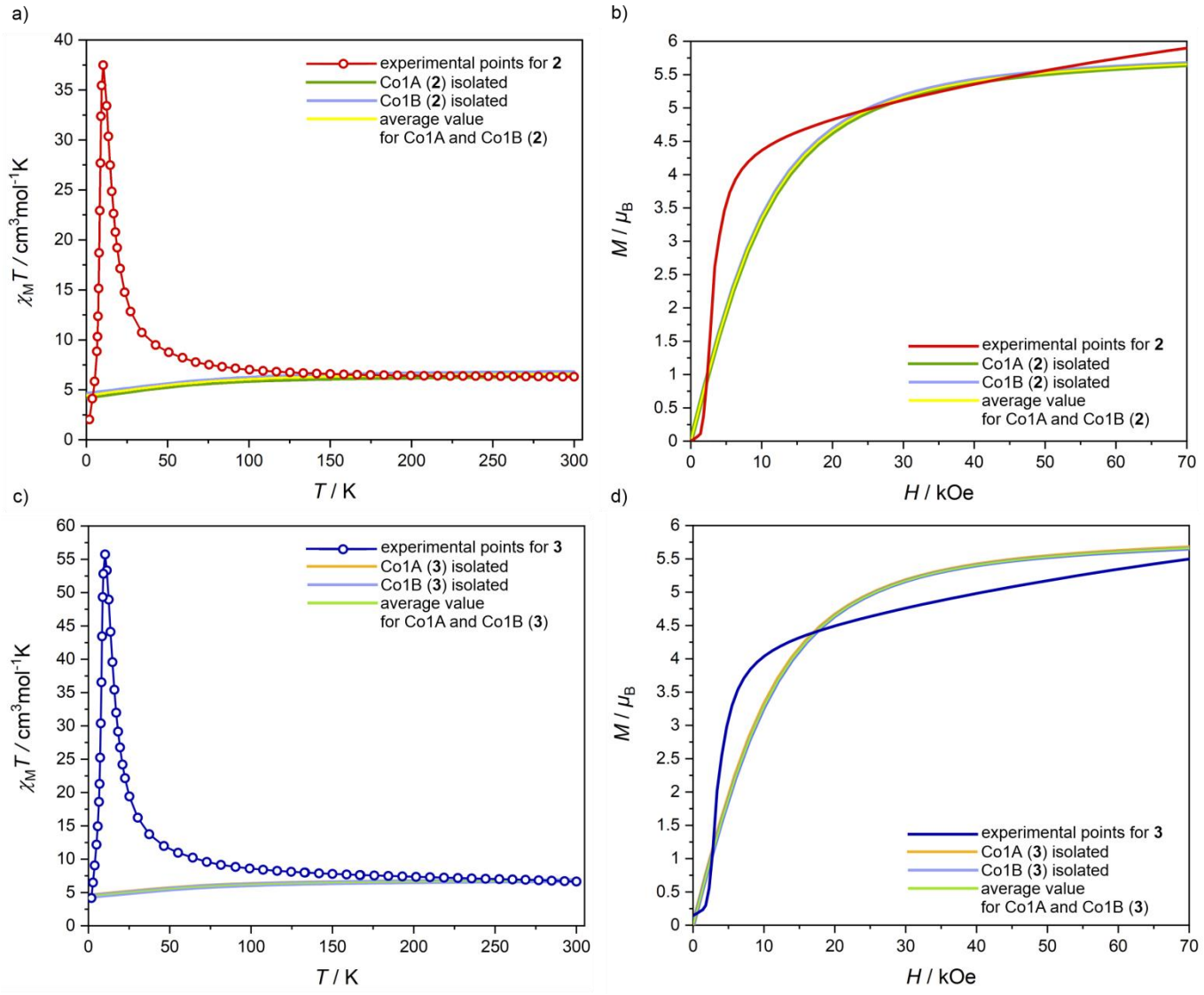

Fig. S31 Comparison of the experimental *dc* magnetic data for **2** (a, b) and **3** (c, d) with the respective magnetic curves calculated based on the results of the *ab initio* calculations performed for isolated Co centres. The presented comparison includes the experimental temperature dependence of the $\chi_M T$ product under H_{dc} = 1000 Oe of **2** compared with the $\chi_M T(T)$ plot calculated for isolated Co1A and Co1B complexes of **2** (Tables S7–S8), together with the average value of the $\chi_M T$ for Co1A and Co1B (a), the experimental field dependence of the molar magnetization for **2** compared with the molar magnetization curve calculated for isolated Co1A and Co1B complexes of **2**, together with the average value of the molar magnetization for Co1A and Co1B (b), the experimental temperature dependence of the $\chi_M T$ product under H_{dc} = 1000 Oe of **3** compared with the $\chi_M T(T)$ plot calculated for isolated Co1A and Co1B complexes of **3** (Tables S9–S10), together with the average value of the $\chi_M T$ for Co1A and Co1B (c), and the experimental field dependence of the molar magnetization for **3** compared with the molar magnetization calculated for isolated Co1A and Co1B complexes of **3**, together with the average value of the molar magnetization for Co1A and Co1B (d).

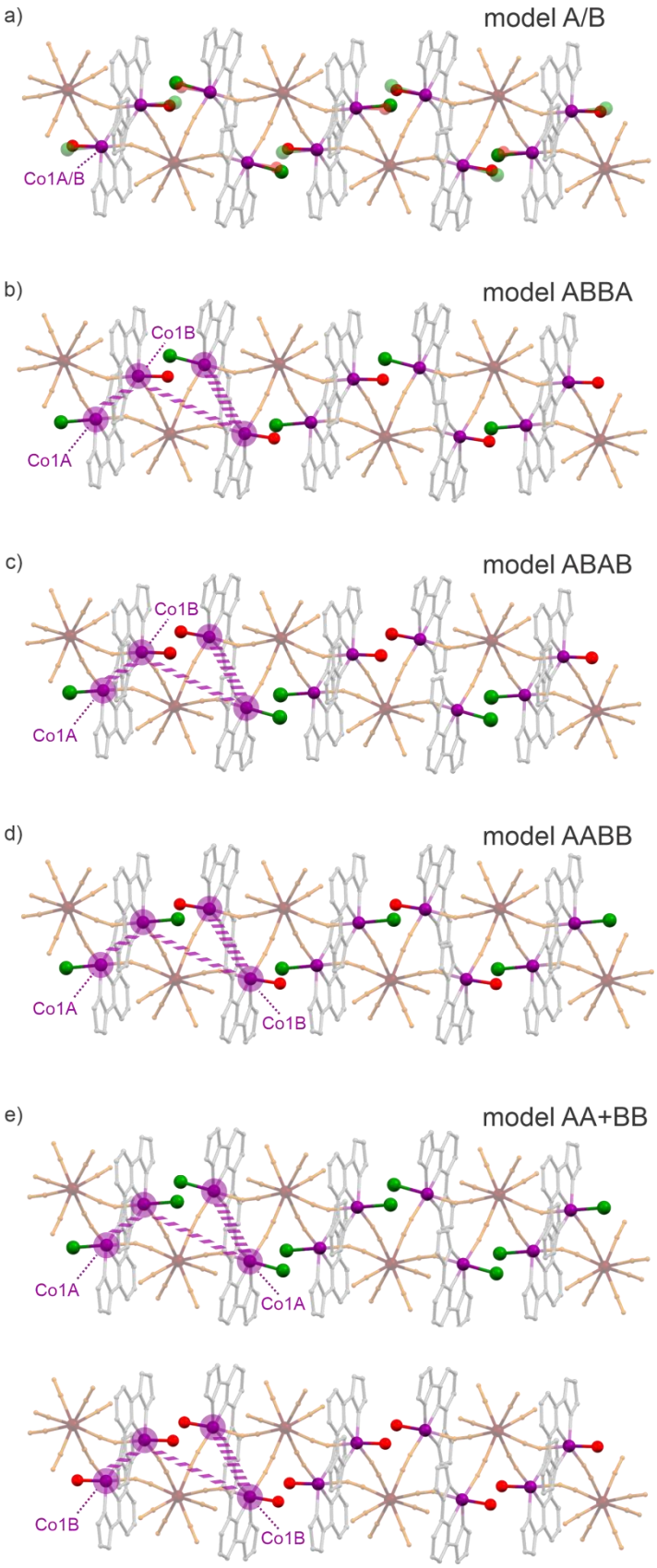

Fig. S32 The set of possible arrangements of H_2O and Cl^- ligands attached to the Co centres within the neighbouring tetrametallic molecular squares of the cyanido-bridged chains of **2** which constitute five magneto-structural models (a–e) that could be considered for the modelling of the magnetic properties, including model A/B (a, partial occupancy of H_2O and Cl^- ligands on the same positions, not realizable within the modelling procedure), model ABBA (b, the Co1A/Co1B/Co1B/Co1A sequence of centres), model ABAB (c, the Co1A/Co1B/Co1A/Co1B sequence of centres), model AABB (d, the Co1A/Co1A/Co1B/Co1B sequence of centres), and model AA+BB (e, two co-existing chains with only Co1A and Co1B centres, respectively). The directions of dominant Co–Co magnetic interactions (mediated by W^V centres) are emphasized by the purple colour. Colour code for selected atoms: purple – Co, red – O, and green – Cl. The analogous arrangements of H_2O and Br^- ligands were considered for **3**.

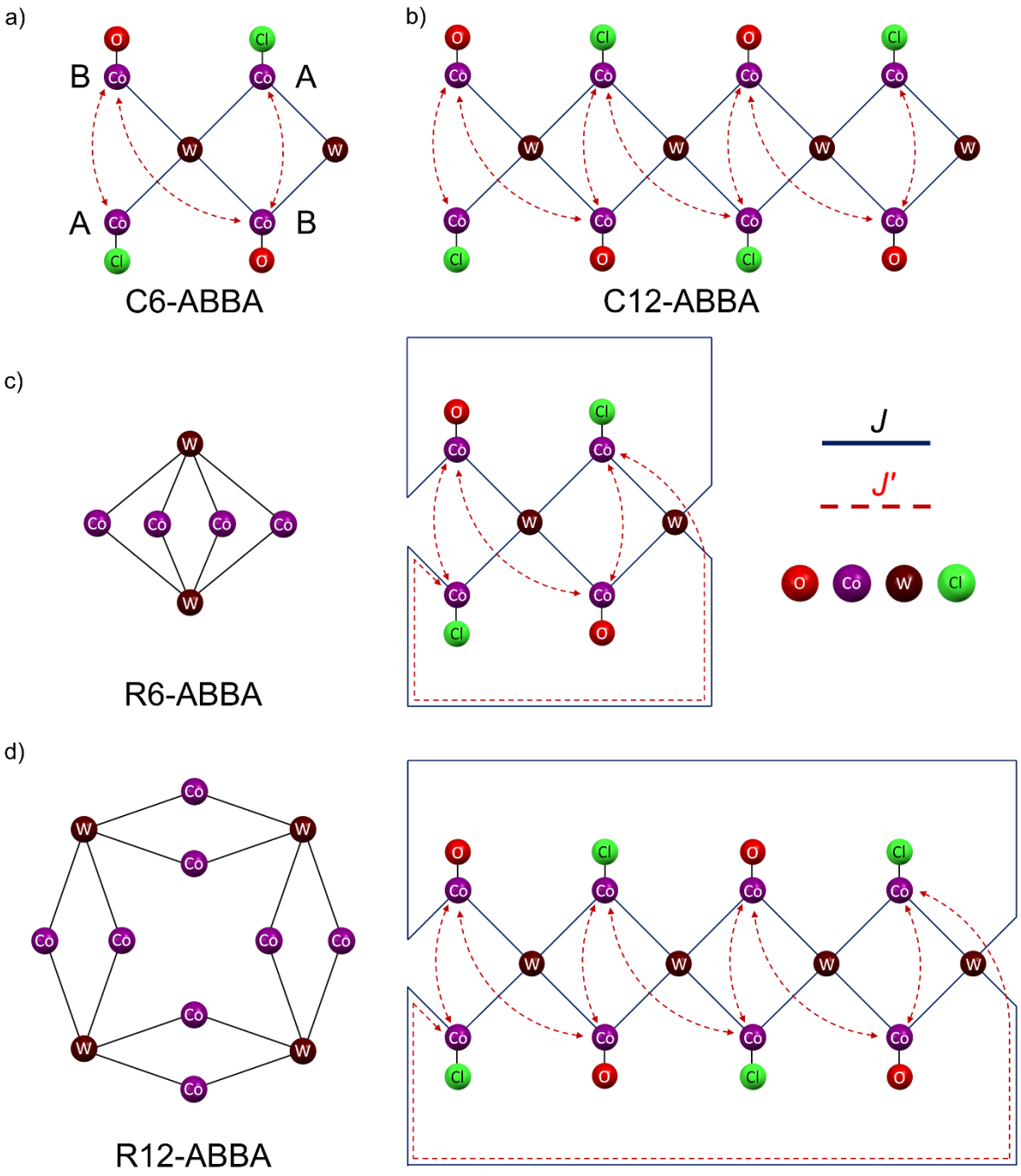

Fig. S33 Visualization of the ABBA-type models (with the Co1A/Co1B/Co1B/Co1A sequence of Co centres) for the modelling of the magnetic properties of **2**, including a six-membered chain (model C6-ABBA) (a), a twelve-membered chain (model C12-ABBA) (b), a six-membered ring (model R6-ABBA) (c), and a twelve-membered ring (model R12-ABBA) (d). The Co–W magnetic exchange is represented by the *J* coupling constant while the Co–Co magnetic interactions are represented by the *J*′ coupling constant. The analogous ABBA-type models were also considered for compound **3**.

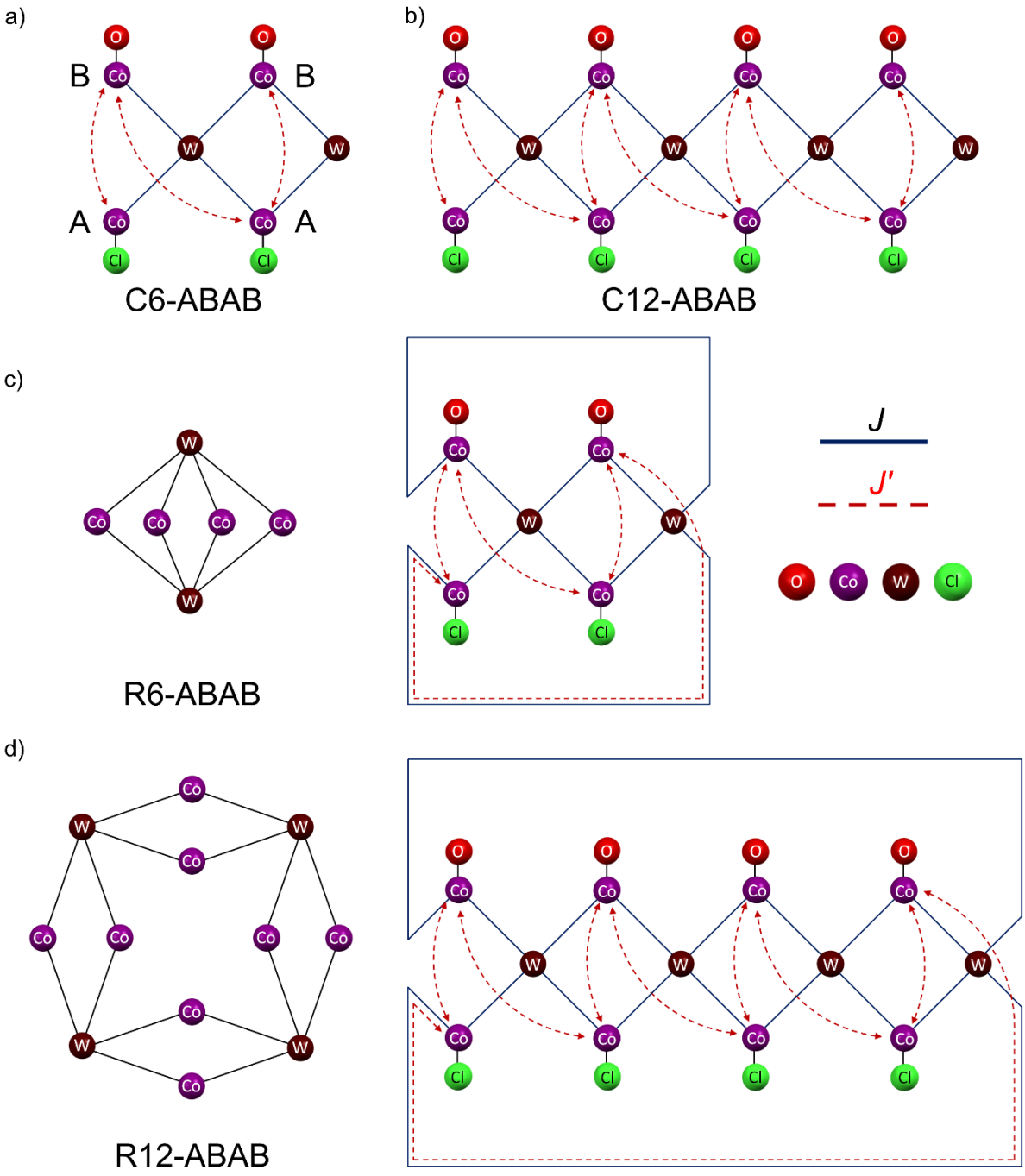

Fig. S34 Visualization of the ABAB-type models (with the Co1A/Co1B/Co1A/Co1B sequence of Co centres) for the modelling of the magnetic properties of **2**, including a six-membered chain (model C6-ABAB) (a), a twelve-membered chain (model C12-ABAB) (b), a six-membered ring (model R6-ABAB) (c), and a twelve-membered ring (model R12-ABAB) (d). The Co–W magnetic exchange is represented by the *J* coupling constant while the Co–Co magnetic interactions are represented by the *J*′ coupling constant. The analogous ABAB-type models were also considered for compound **3**.

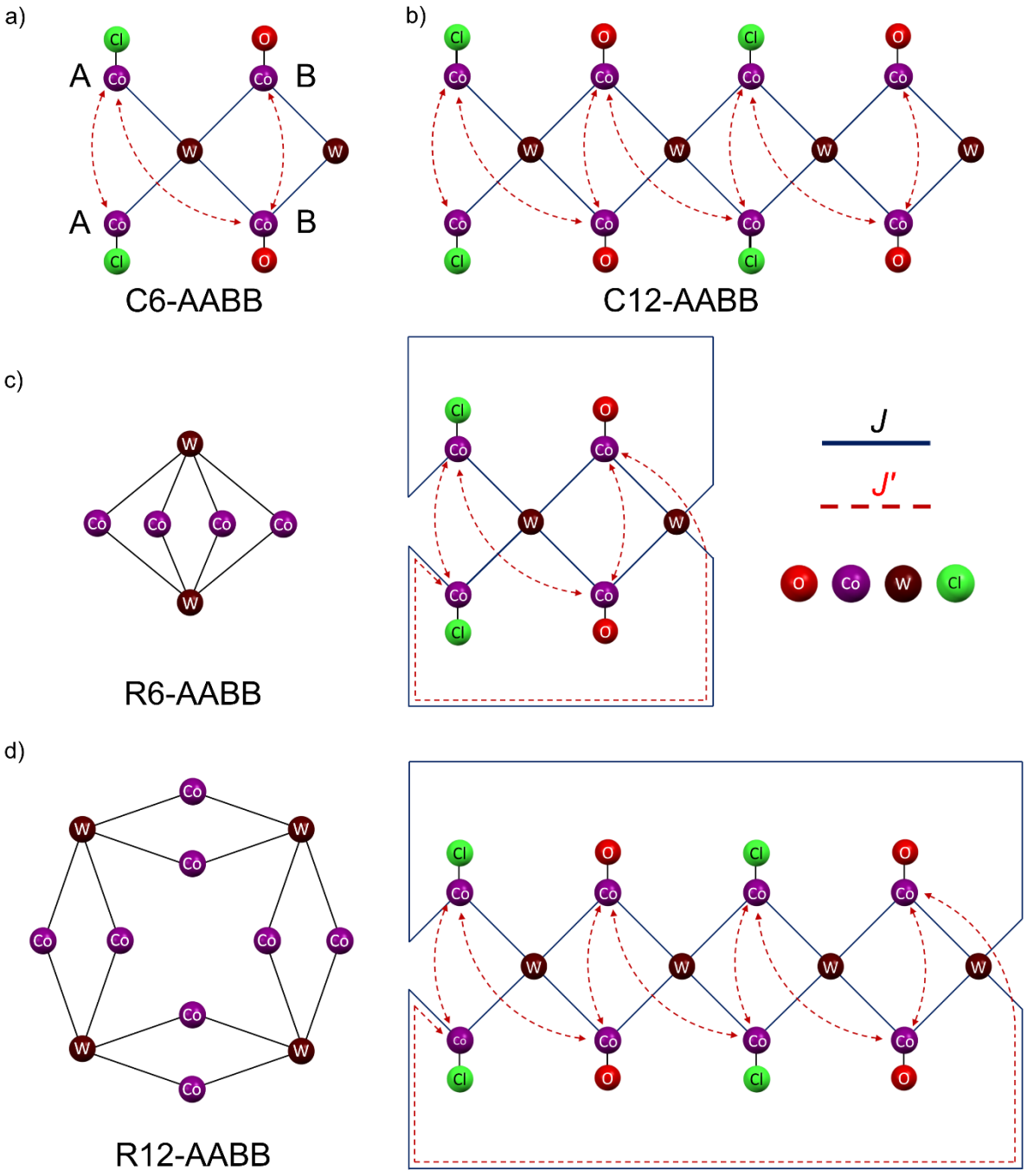

Fig. S35 Visualization of the AABB-type models (with the Co1A/Co1A/Co1B/Co1B sequence of Co centres) for the modelling of the magnetic properties of **2**, including a six-membered chain (model C6-AABB) (a), a twelve-membered chain (model C12-AABB) (b), a six-membered ring (model R6-AABB) (c), and a twelve-membered ring (model R12-AABB) (d). The Co–W magnetic exchange is represented by the *J* coupling constant while the Co–Co magnetic interactions are represented by the *J*' coupling constant. The analogous AABB-type models were also considered for compound **3**.

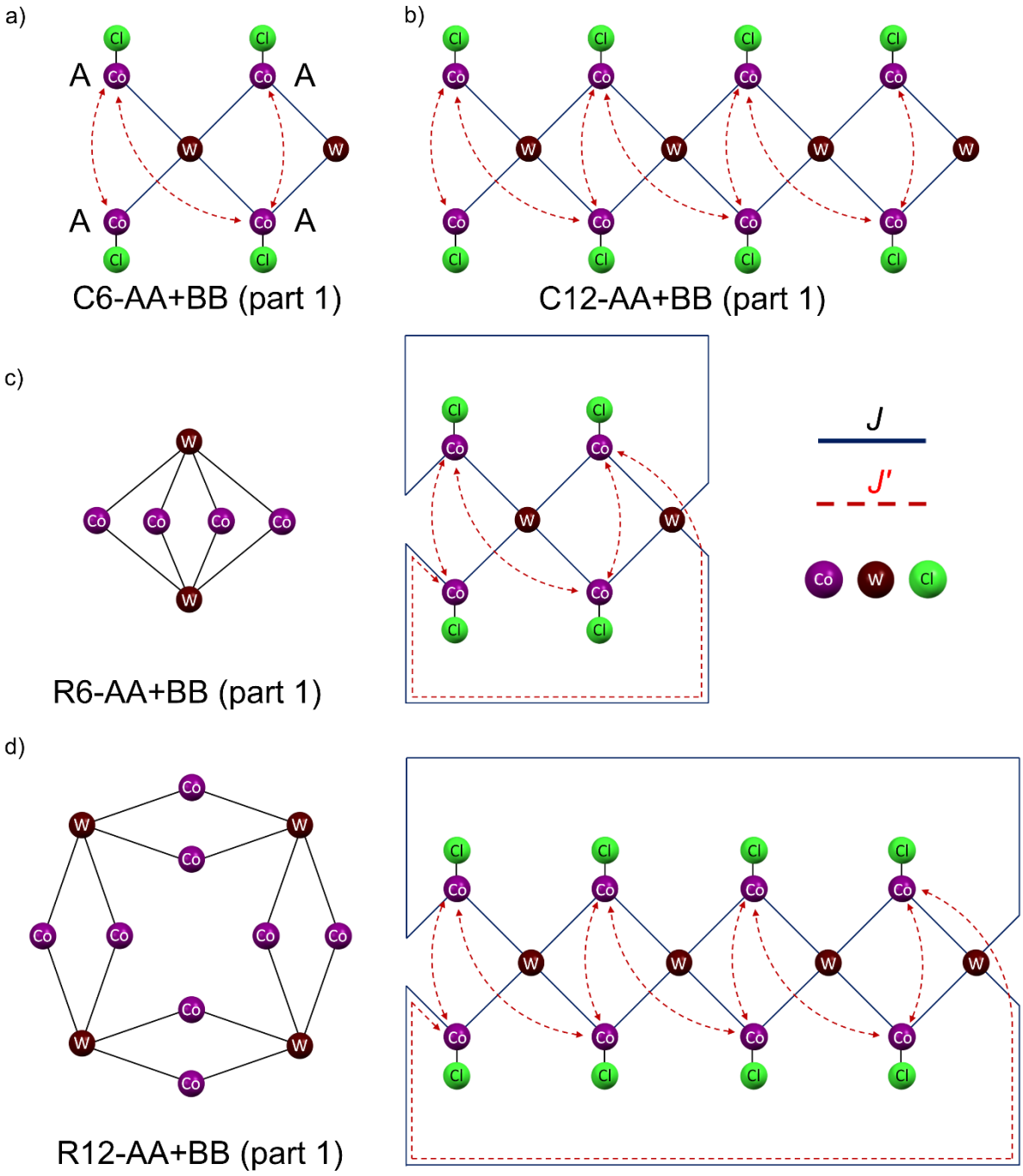

Fig. S36 Visualization of the (AA+BB)-type models, part 1 (with the separated chains of Co1A and Co1B centres, in the part only the Co1A centres modelling of the magnetic properties of **2**, including a six-membered chain (model C6-AA+BB, part 1) (a), a twelve-membered chain (model C12-AA+BB, part 1) (b), a six-membered ring (model R6-AA+BB, part 1) (c), and a twelve-membered ring (model R12-AA+BB, part 1) (d). The Co–W magnetic exchange is represented by the *J* coupling constant while the Co–Co magnetic interactions are represented by the *J*′ coupling constant. The analogous AABB-type models were also considered for compound **3**. The second part of this model is shown in Fig. S37.

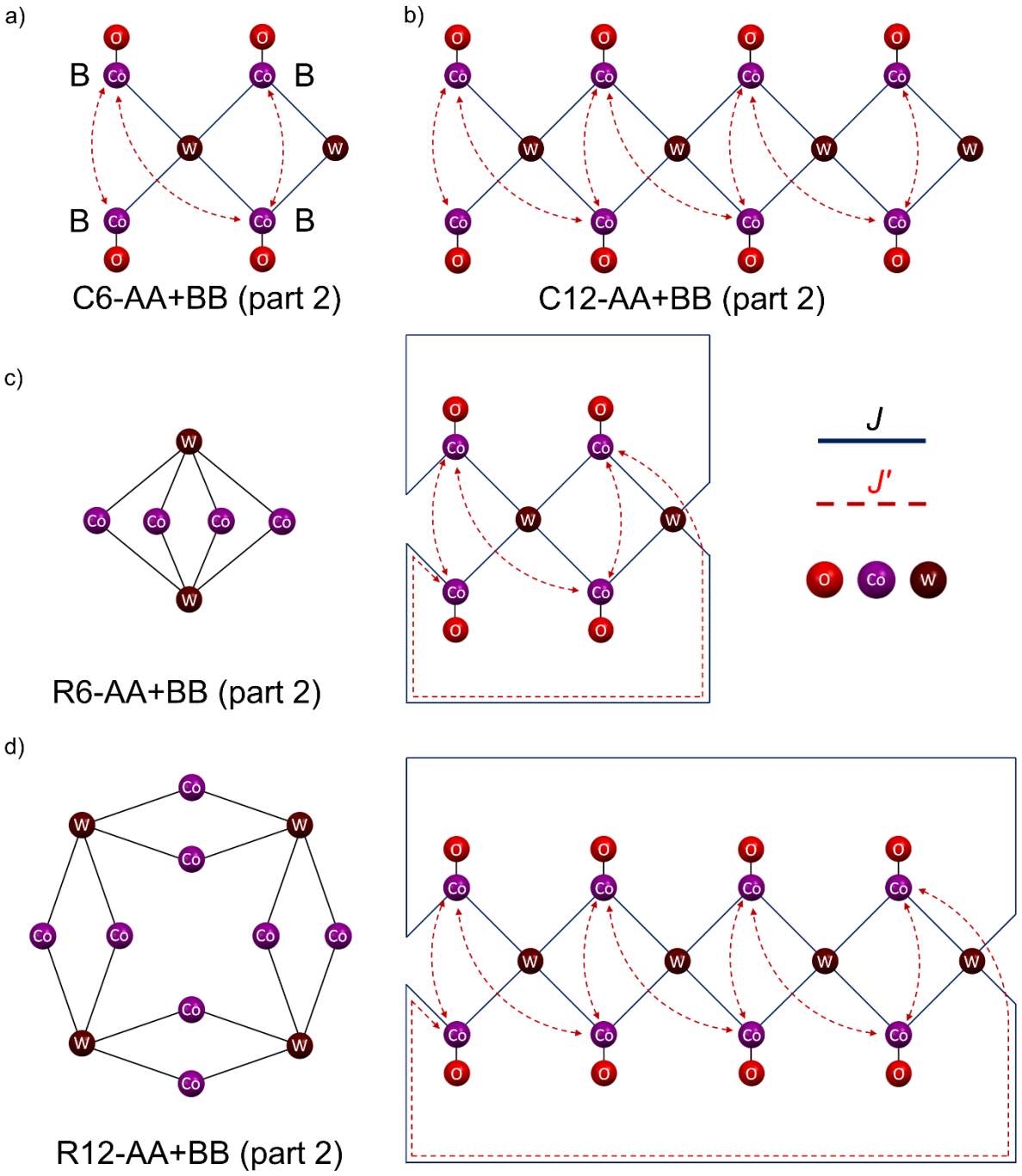

Fig. S37 Visualization of the (AA+BB)-type models, part 2 (with the separated chains of Co1A and Co1B centres, in the part only the Co1B centres modelling of the magnetic properties of **2**, including a six-membered chain (model C6-AA+BB, part 2) (a), a twelve-membered chain (model C12-AA+BB, part 2) (b), a six-membered ring (model R6-AA+BB, part 2) (c), and a twelve-membered ring (model R12-AA+BB, part 2) (d). The Co–W magnetic exchange is represented by the *J* coupling constant while the Co–Co magnetic interactions are represented by the *J*′ coupling constant. The analogous AABB-type models were also considered for compound **3**. The first part of this model is shown in Fig. S36.

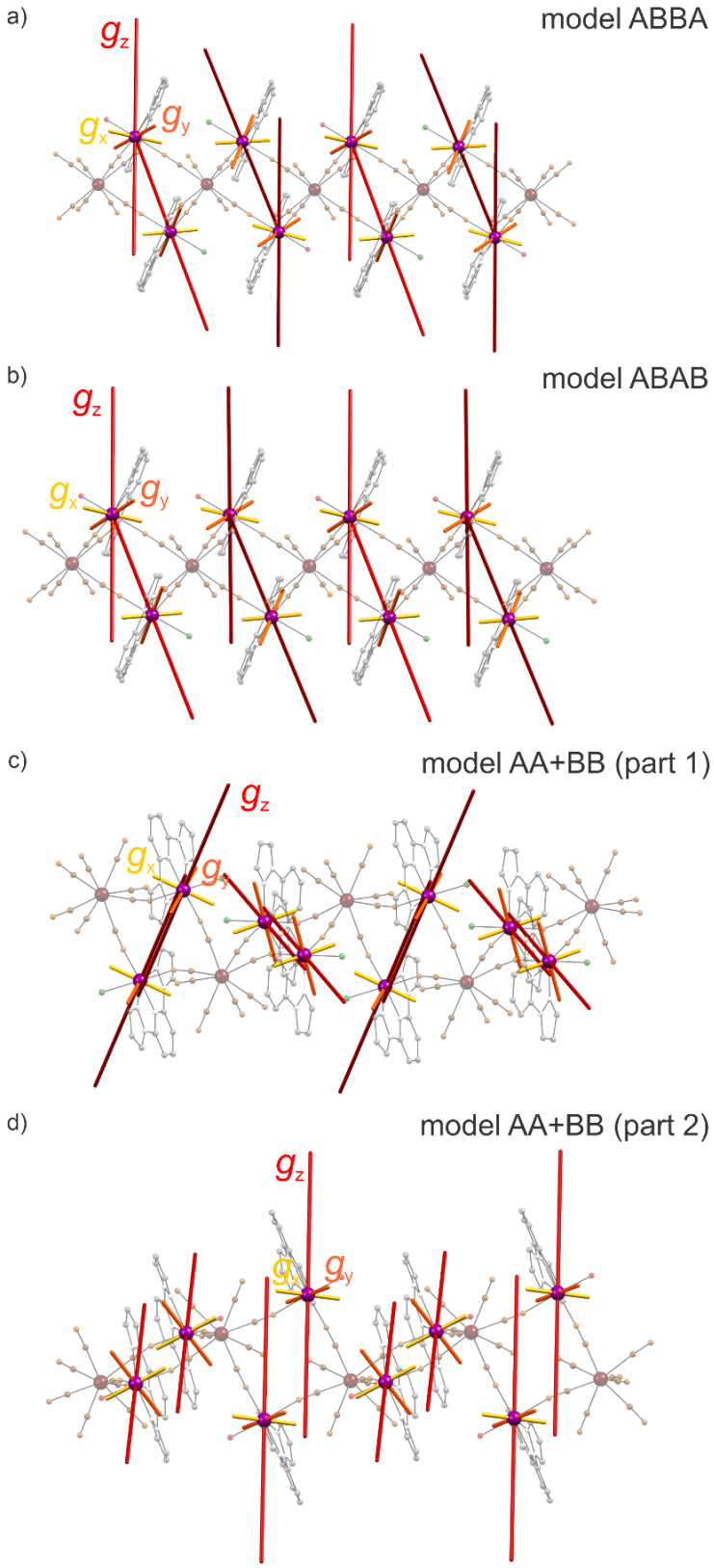

Fig. S38 The alignment of pseudo-*g*-tensor components in the chains of **2** within the indicated magneto-structural models of ABBA (a), ABAB (b), AA+BB (part 1) (c, only Co1A centres in the chain), and AA+BB (part 2) (d, only Co1B centres in the chain). The related visualization of the pseudo-*g*-tensor components for the AABB model is presented in Fig. 7b.

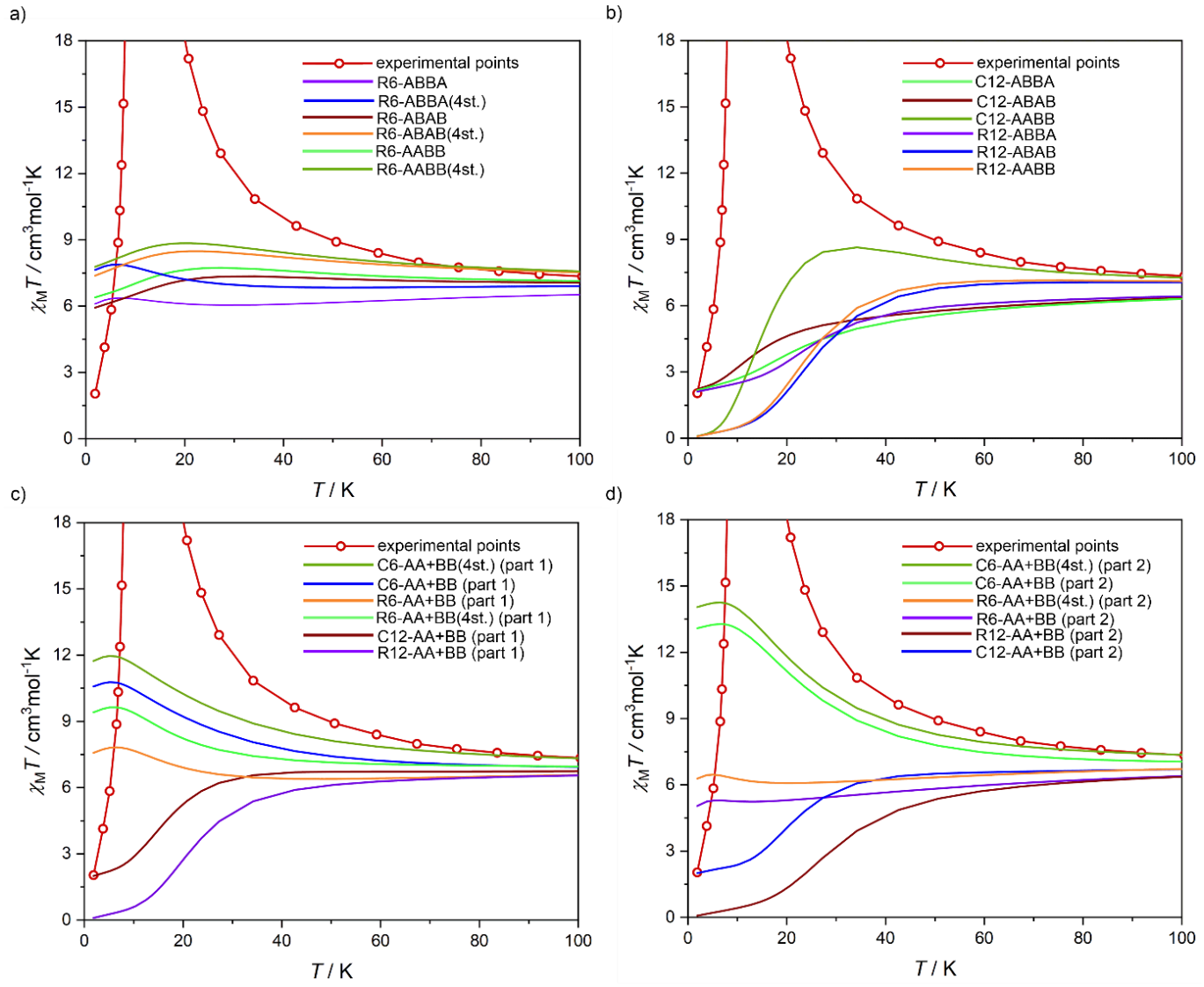

Fig. S39 Experimental temperature dependence of the $\chi_M T$ product under H_{dc} = 1000 Oe for **2** compared with the $\chi_M T(T)$ curves calculated using the results of the *ab initio* calculations combined with the simulations of magnetic exchange employing various R6-type models (R6-ABBA, R6-ABBA(4st.), R6-ABAB, R6-ABAB(4st.), R6-AABB, and R6-AABB(4st.)) (a), various C12- and R12-type models (C12-ABBA, C12-ABAB, C12-AABB, R12-ABBA, R12-ABAB, and R12-AABB) (b), the 1st parts of various (AA+BB)-type models (C6-AA+BB(4st.), C6-AA+BB, R6-AA+BB(4st.), R6-AA+BB, C12-AA+BB, and R12-AA+BB) (c), and the 2nd parts of various (AA+BB)-type models (C6-AA+BB(4st.), C6-AA+BB, R6-AA+BB(4st.), R6-AA+BB, C12-AA+BB, and R12-AA+BB) (d). The respective results for selected best models were presented in Fig. 7d. All simulations are shown for the best-fit using the *J* value of 25.1 cm^{-1} and the *J*′ of –0.6 cm^{-1} taken from the modelling of the magnetic properties of **1** (Fig. 6). The extension (4st.) used for the part of the presented models represent the extended calculations employing four higher lying energy states of each Co centre while only the lowest ones are used for all other calculations.

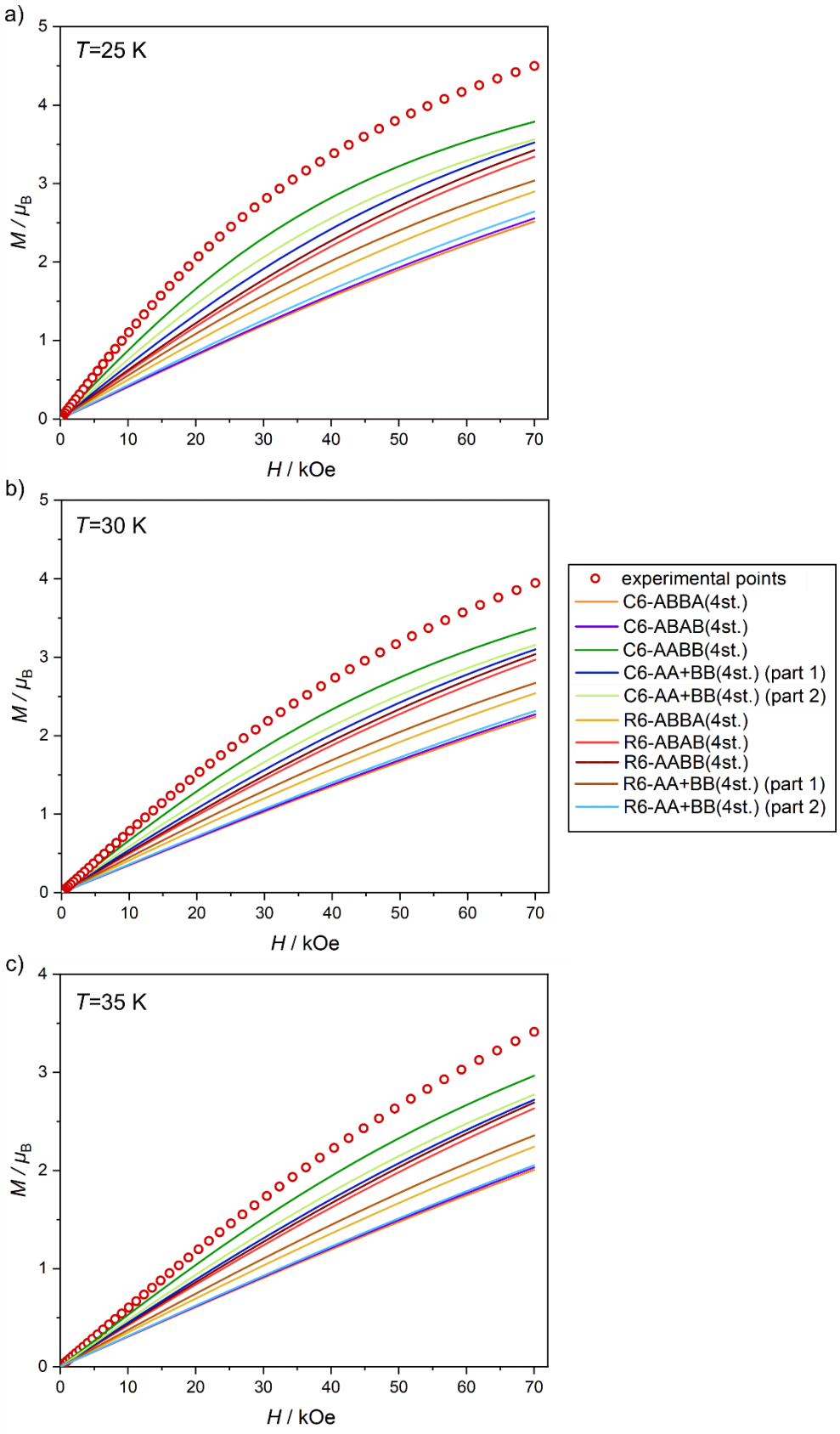

Fig. S40 Experimental field dependence of the molar magnetization for **2** at the indicated temperatures of 25 K (a), 30 K (b), and 35 K (c) compared with the respective molar magnetization curves calculated using the results of the *ab initio* calculations combined with the simulations of magnetic exchange employing using magneto-structural models, including C6-ABBA(4st.), C6-ABAB(4st.), C6-AABB(4st.), C6-AA+BB(4st.) (part 1), C6-AA+BB(4st.) (part 2), R6-ABBA(4st.), R6-ABAB(4st.), R6-AABB(4st.), R6-AA+BB(4st.) (part 1), and R6-AA+BB(4st.) (part 2).

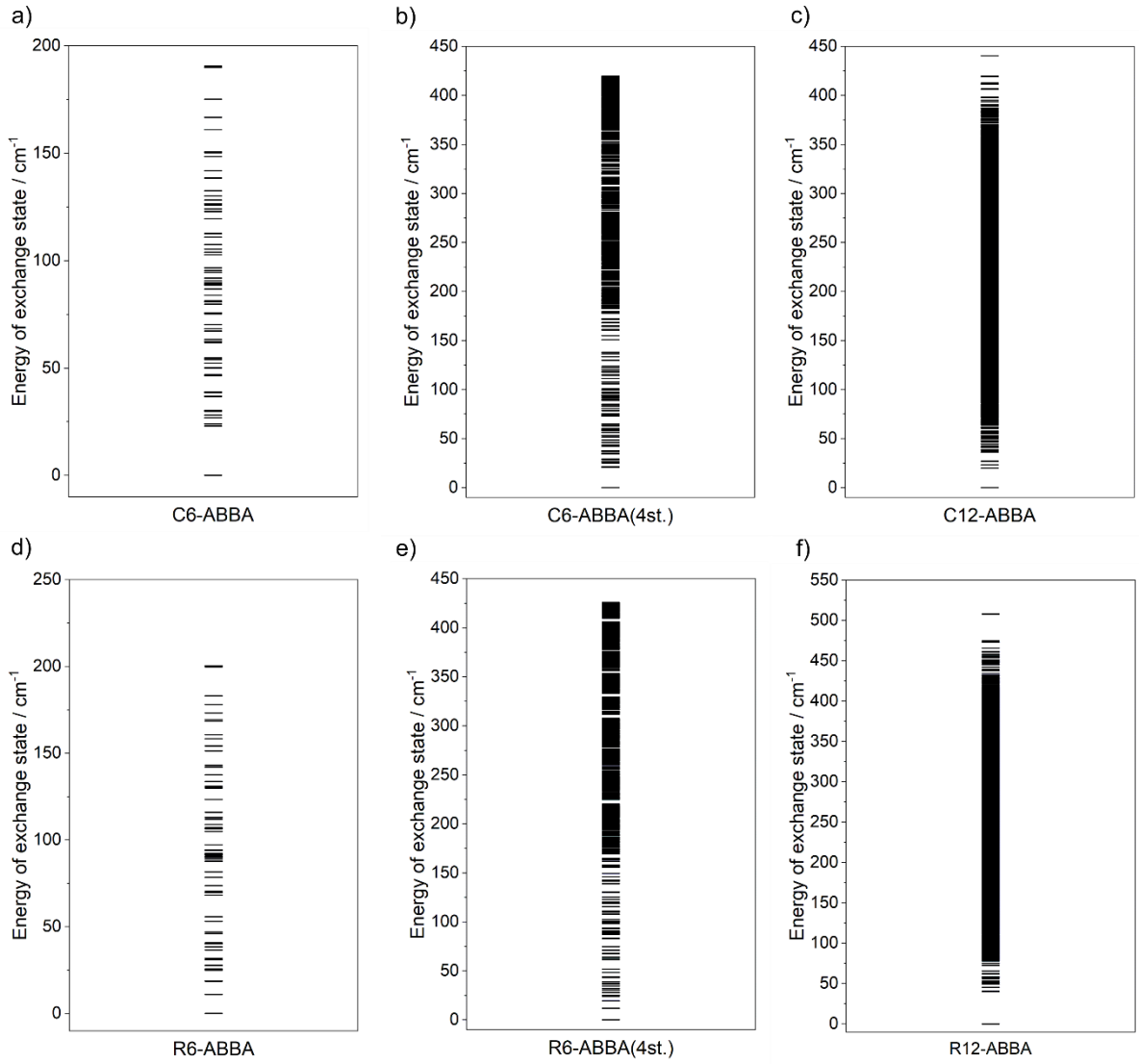

Fig. S41 The scheme of exchange states for **2** calculated using the results of the *ab initio* calculations (Tables S7–S8, Fig. 5, and Fig. 7) combined with the fitting of the exchange coupling pathways according to six different magneto-structural models of C6-ABBA (a), C6-ABBA(4st.) (b), C12-ABBA (c), R6-ABBA (d), R6-ABBA(4st.) (e), and R12-ABBA (f). The extension (4st.) used for the part of the presented models represent the extended calculations employing four higher lying energy states of each Co centre while only the lowest ones are used for all other calculations. For the visualization of all the indicated models see Fig. S33. The results are for the optimized set of exchange coupling constants of J = 25.1 cm^{-1}, J' = –0.6 cm^{-1}.

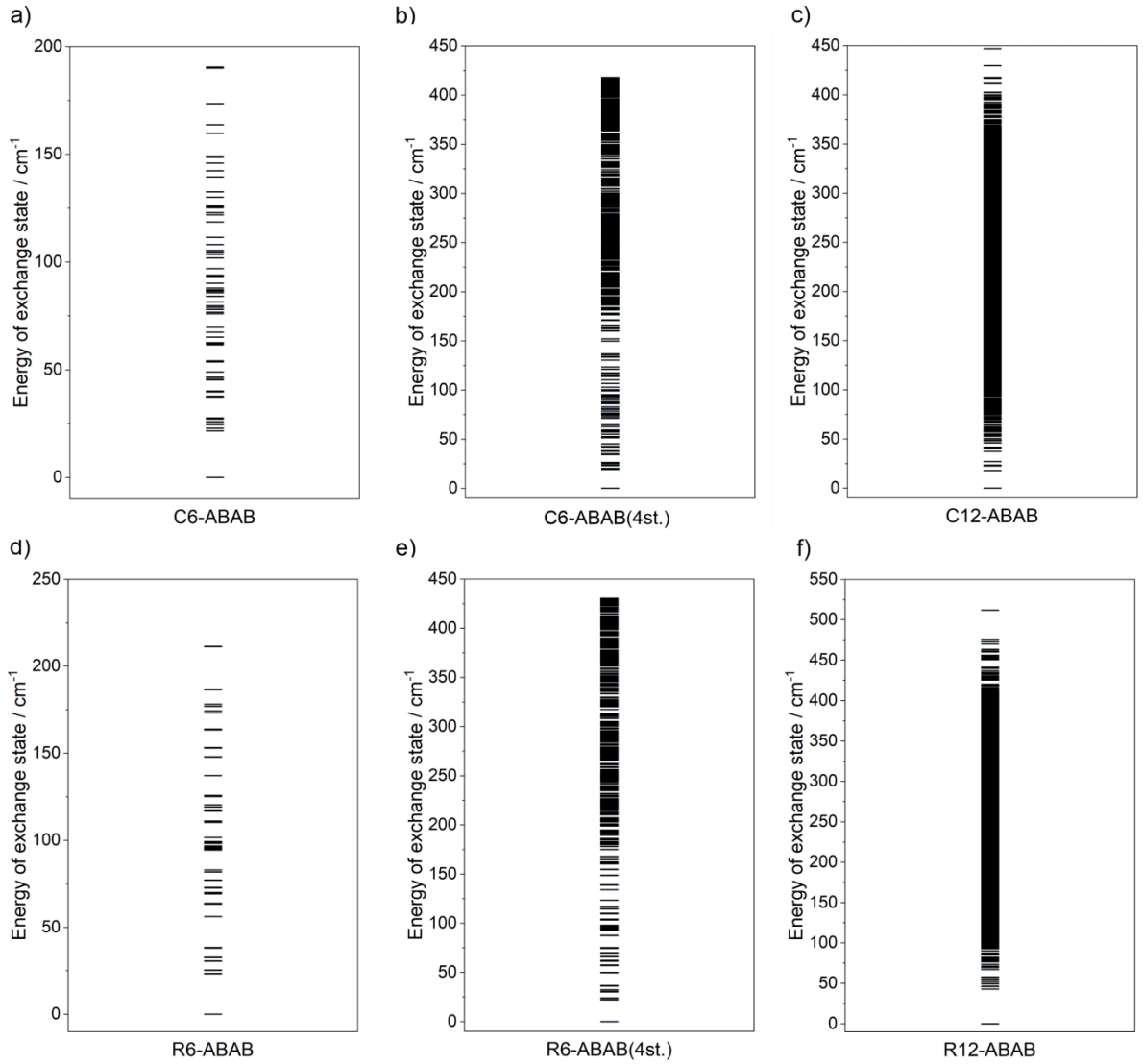

Fig. S42 The scheme of exchange states for **2** calculated using the results of the *ab initio* calculations (Tables S7–S8, Fig. 5, and Fig. 7) combined with the fitting of the exchange coupling pathways according to six different magneto-structural models of C6-ABAB (a), C6-ABAB(4st.) (b), C12-ABAB (c), R6-ABAB (d), R6-ABAB(4st.) (e), and R12-ABAB (f). The extension (4st.) used for the part of the presented models represent the extended calculations employing four higher lying energy states of each Co centre while only the lowest ones are used for all other calculations. For the visualization of all the indicated models see Fig. S34. The results are for the optimized set of exchange coupling constants of J = 25.1 cm^{-1}, J' = –0.6 cm^{-1}.

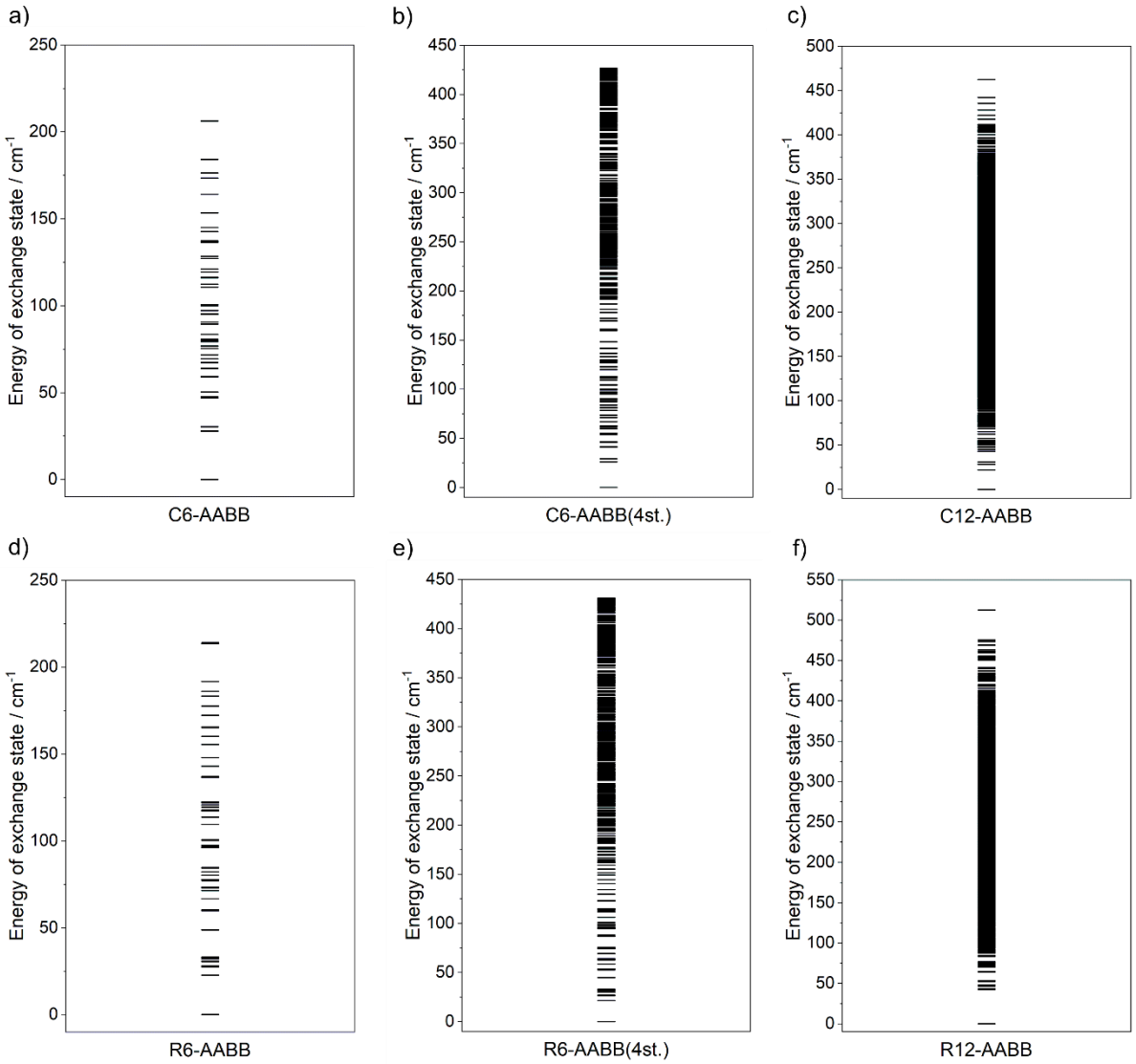

Fig. S43 The scheme of exchange states for **2** calculated using the results of the *ab initio* calculations (Tables S7–S8, Fig. 5, and Fig. 7) combined with the fitting of the exchange coupling pathways according to six different magneto-structural models of C6-AABB (a), C6-AABB(4st.) (b), C12-AABB (c), R6-AABB (d), R6-AABB(4st.) (e), and R12-AABB (f). The extension (4st.) used for the part of the presented models represent the extended calculations employing four higher lying energy states of each Co centre while only the lowest ones are used for all other calculations. For the visualization of all the indicated models see Fig. S35. The results are for the optimized set of exchange coupling constants of J = 25.1 cm^{-1}, J' = –0.6 cm^{-1}.

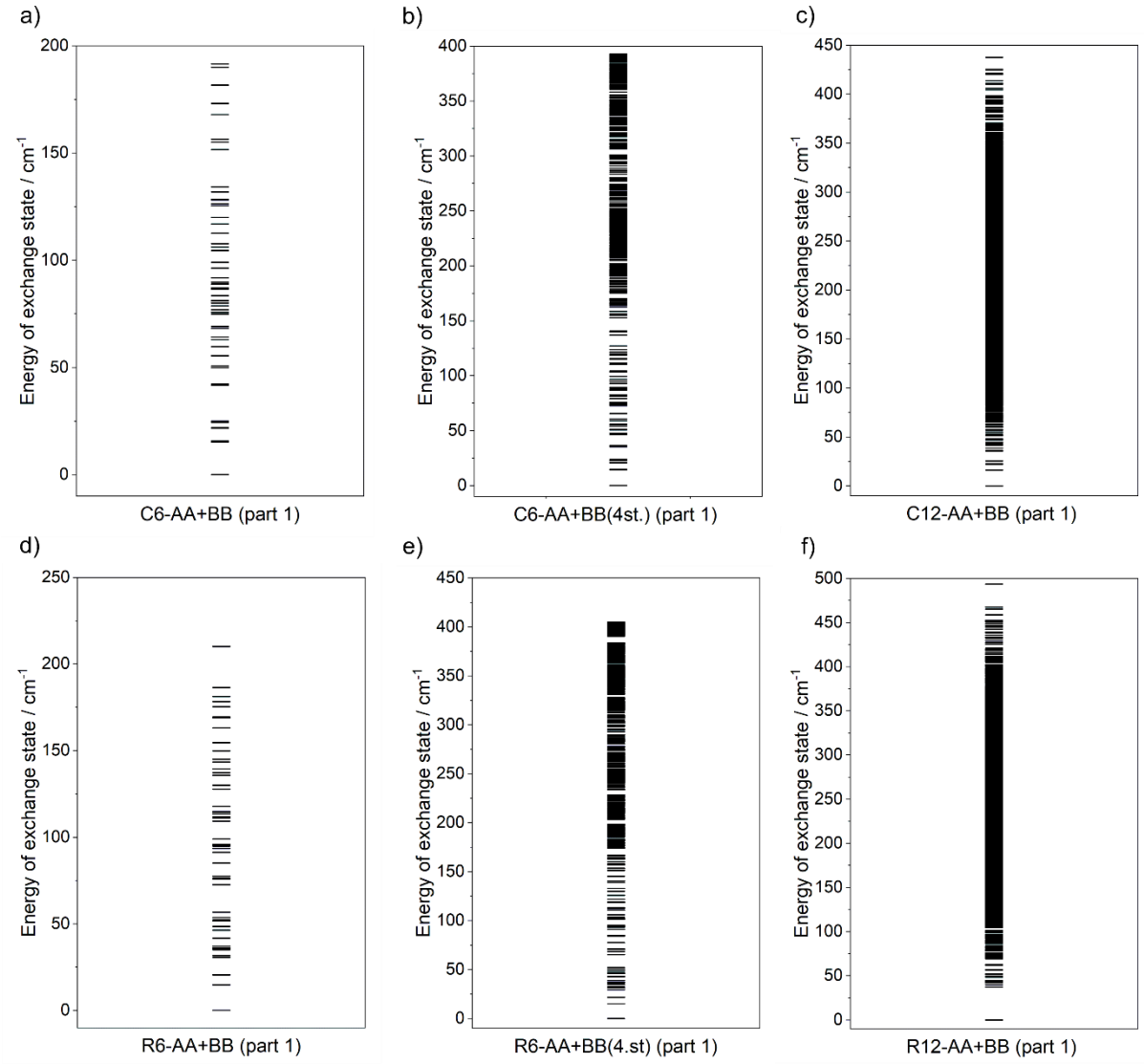

Fig. S44 The scheme of exchange states for **2** calculated using the results of the *ab initio* calculations (Tables S7–S8, Fig. 5, and Fig. 7) combined with the fitting of the exchange coupling pathways according to six different magneto-structural models of C6-AA+BB (part 1) (a), C6-AA+BB(4st.) (part 1) (b), C12-AA+BB (part 1) (c), R6-AA+BB (part 1) (d), R6-AA+BB(4st.) (part 1) (e), and R12-AA+BB (part 1) (f). The extension (4st.) used for the part of the presented models represent the extended calculations employing four higher lying energy states of each Co centre while only the lowest ones are used for all other calculations. For the visualization of all the indicated models see Fig. S36. The results are for the optimized set of exchange coupling constants of J = 25.1 cm^{-1}, J' = –0.6 cm^{-1}.

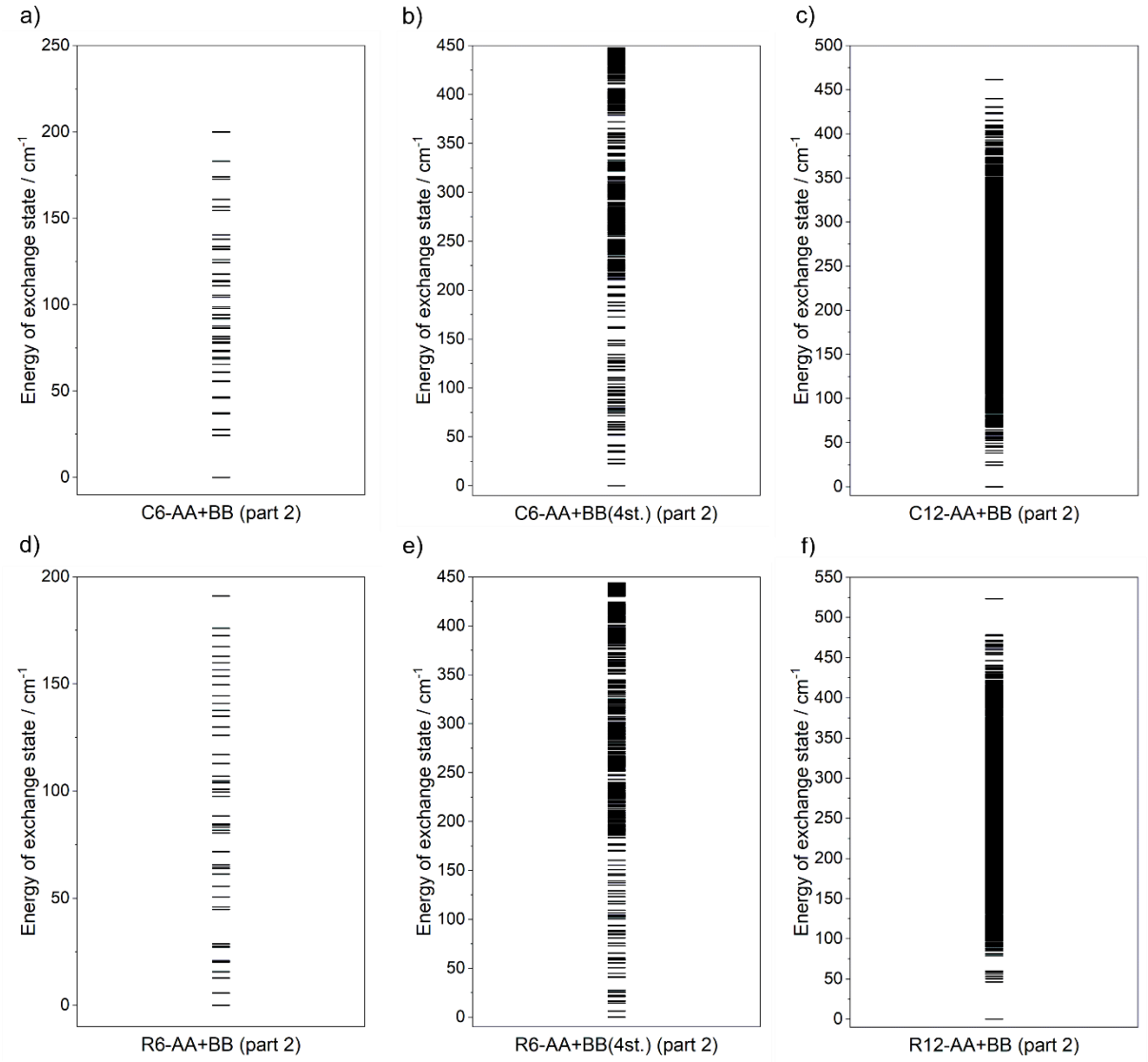

Fig. S45 The scheme of exchange states for **2** calculated using the results of the *ab initio* calculations (Tables S7–S8, Fig. 5, and Fig. 7) combined with the fitting of the exchange coupling pathways according to six different magneto-structural models of C6-AA+BB (part 2) (a), C6-AA+BB(4st.) (part 2) (b), C12-AA+BB (part 2) (c), R6-AA+BB (part 2) (d), R6-AA+BB(4st.) (part 2) (e), and R12-AA+BB (part 2) (f). The extension (4st.) used for the part of the presented models represent the extended calculations employing four higher lying energy states of each Co centre while only the lowest ones are used for all other calculations. For the visualization of all the indicated models see Fig. S37. The results are for the optimized set of exchange coupling constants of J = 25.1 cm^{-1}, J' = –0.6 cm^{-1}.

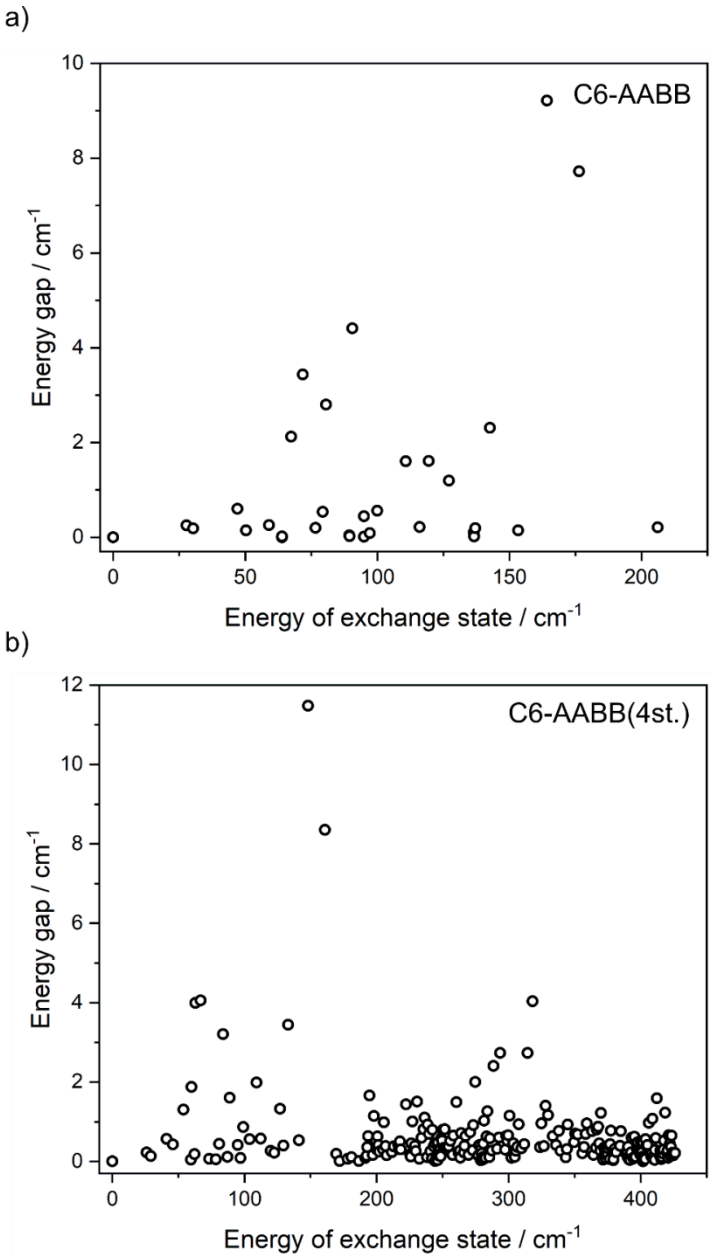

Fig. S46 The dependence between the average energy of the pairs of exchange states (pseudo-doublets) and the related energy gaps determined for **2** using the *ab initio* calculations combined with the fitting of the exchange constant according to two selected magneto-structural models, named C6-AABB (a) and C6-AABB(4st.) (b) (these models produced the best-fit to the experimental data, see Fig. 7d). The models are visualized in Fig. 7 and Fig. S35 while the numerical data for the obtained exchange states are gathered in Table 3 and Table S20.

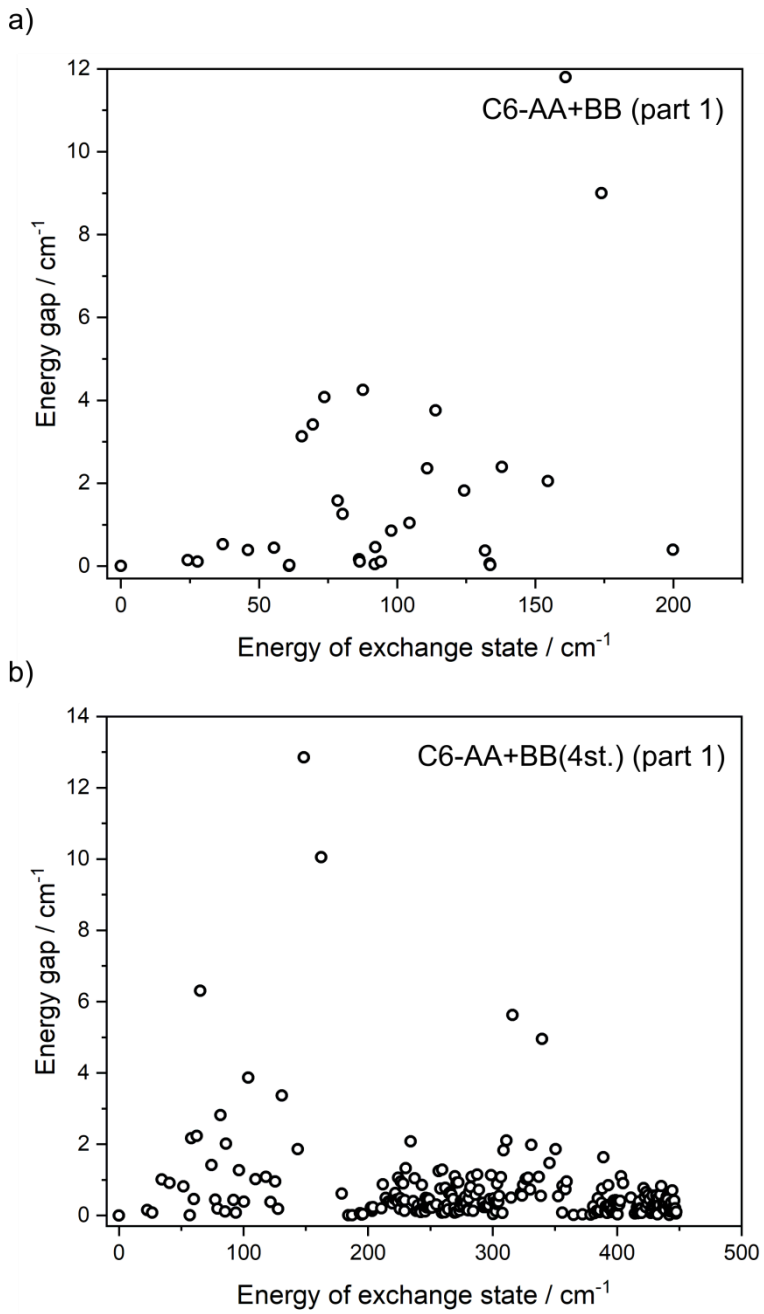

Fig. S47 The dependence between the average energy of the pairs of exchange states (pseudo-doublets) and the related energy gaps determined for **2** using the *ab initio* calculations combined with the fitting of the exchange constant according to two selected magneto-structural models, named C6-AA+BB (part 1) (a) and C6-AA+BB(4st.) (part 1) (b) (these models produced the relatively good fits to the experimental data, see Fig. 7d). The models are visualized in Fig. 7 and Fig. S36 while the numerical data for the obtained exchange states are gathered in Table S22.

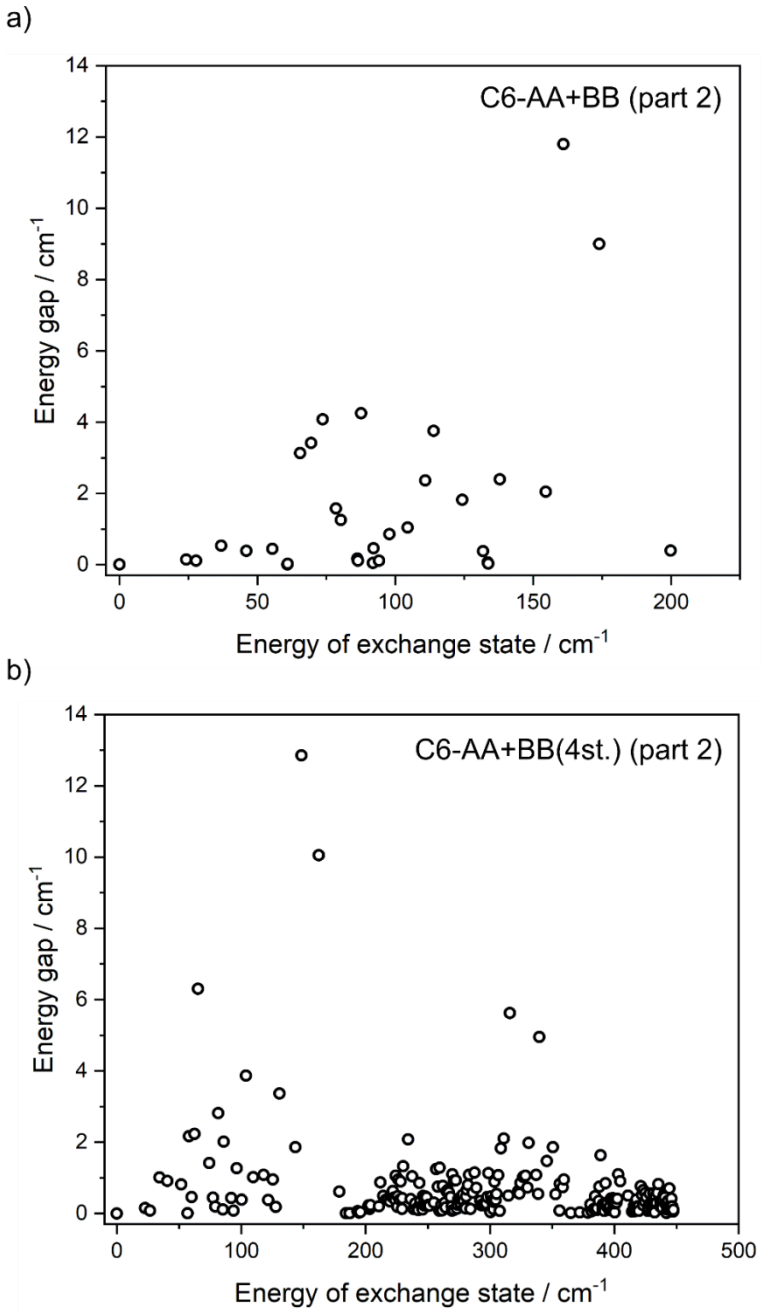

Fig. S48 The dependence between the average energy of the pairs of exchange states (pseudo-doublets) and the related energy gaps determined for **2** using the *ab initio* calculations combined with the fitting of the exchange constant according to two selected magneto-structural models, named C6-AA+BB (part 2) (a) and C6-AA+BB(4st.) (part 2) (b) (these models produced the relatively good fits to the experimental data, see Fig. 7d). The models are visualized in Fig. 7 and Fig. S37 while the numerical data for the obtained exchange states are gathered in Table S24.

Table S16 The selected parameters obtained from modelling the magnetic properties of **2** based on the results of the *ab initio* calculations combined with the fitting of the exchange coupling according to three magneto-structural models, named C6-ABBA, C6-ABBA(4st.), and C12-ABBA (Fig. S33 and Fig. S41). The presented results include the lists of 16 lowest lying exchange states (8 lowest lying pairs of exchange states, pseudo-doublets) and the respective energy gaps. The further, higher lying states are visualized in Fig. S41. The lowest lying pairs of states showing the relatively large energy gaps are emphasized by bold fonts. The labels (4st.) represent the extended calculations employing four higher energy states of each Co centre.

No. of the pair of exchange states (pseudo-doublets)	Energy of a lower lying state / cm^{-1}	Energy of a higher lying state / cm^{-1}	Energy gap / cm^{-1}
model C6-ABBA (Fig. S33a and Fig. S41a)			
1	0.0	0.010	0.010
2	22.976	24.037	1.061
3	26.821	28.002	1.181
4	29.805	30.274	0.469
5	36.719	36.920	0.201
6	38.542	38.923	0.381
7	46.512	46.898	0.386
8	**50.061**	**52.255**	**2.194**
model C6-ABBA(4st.) (Fig. S33a and Fig. S41b)			
1	0.0	0.008	0.008
2	20.590	21.416	0.826
3	25.293	26.587	1.294
4	28.761	29.113	0.352
5	34.381	34.818	0.437
6	36.866	37.510	0.644
7	42.293	43.317	1.024
8	**45.989**	**48.531**	**2.542**
model C12-ABBA (Fig. S33b and Fig. S41c)			
1	0.0	0.0	0.0
2	19.837	19.837	0.0
3	23.203	23.204	0.001
4	26.93	26.93	0.0
5	35.865	35.872	0.007
6	37.277	37.285	0.008
7	38.570	38.588	0.018
8	**40.828**	**40.848**	**0.020**

Table S17 The selected parameters obtained from modelling the magnetic properties of **2** based on the results of the *ab initio* calculations combined with the fitting of the exchange coupling according to three magneto-structural models, named R6-ABBA, R6-ABBA(4st.), and R12-ABBA (Fig. S33 and Fig. S41). The presented results include the lists of 16 lowest lying exchange states (8 lowest lying pairs of exchange states, pseudo-doublets) and the respective energy gaps. The further, higher lying states are visualized in Fig. S41. The lowest lying pairs of states showing the relatively large energy gaps are emphasized by bold fonts. The labels (4st.) represent the extended calculations employing four higher energy states of each Co centre.

No. of the pair of exchange states (pseudo-doublets)	Energy of a lower lying state / cm^{-1}	Energy of a higher lying state / cm^{-1}	Energy gap / cm^{-1}
model R6-ABBA (Fig. S33c and Fig. S41d)			
1	0.0	0.016	0.016
2	10.943	10.996	0.053
3	18.630	18.746	0.116
4	25.036	25.787	0.751
5	27.666	27.749	0.083
6	31.014	31.718	0.704
7	**36.695**	**38.466**	**1.771**
8	40.110	40.753	0.643
model R6-ABBA(4st.) (Fig. S33c and Fig. S41e)			
1	0.0	0.016	0.016
2	11.835	11.886	0.051
3	19.422	19.539	0.117
4	24.009	25.054	1.045
5	27.740	27.916	0.176
6	30.299	31.964	1.665
7	**34.492**	**36.734**	**2.242**
8	36.923	38.747	1.824
model R12-ABBA (Fig. S33d and Fig. S41f)			
1	0.0	0.0	0.0
2	40.160	40.162	0.002
3	45.287	45.289	0.002
4	49.282	49.284	0.002
5	50.861	50.876	0.015
6	52.864	52.873	0.009
7	**56.098**	**56.149**	**0.051**
8	57.677	57.699	0.022

Table S18 The selected parameters obtained from modelling the magnetic properties of **2** based on the results of the *ab initio* calculations combined with the fitting of the exchange coupling according to three magneto-structural models, named C6-ABAB, C6-ABAB(4st.), and C12-ABAB (Fig. S34 and Fig. S42). The presented results include the lists of 16 lowest lying exchange states (8 lowest lying pairs of exchange states, pseudo-doublets) and the respective energy gaps. The further, higher lying states are visualized in Fig. S42. The lowest lying pairs of states showing the relatively large energy gaps are emphasized by bold fonts. The labels (4st.) represent the extended calculations employing four higher energy states of each Co centre.

No. of the pair of exchange states (pseudo-doublets)	Energy of a lower lying state / cm^{-1}	Energy of a higher lying state / cm^{-1}	Energy gap / cm^{-1}
model C6-ABAB (Fig. S34a and Fig. S42a)			
1	0.0	0.012	0.012
2	21.620	22.853	1.233
3	24.563	25.762	1.199
4	27.176	27.612	0.436
5	37.313	37.669	0.356
6	39.749	40.107	0.358
7	45.313	45.609	0.296
8	**46.494**	**49.033**	**2.539**
model C6-ABAB(4st.) (Fig. S34a and Fig. S42b)			
1	0.0	0.009	0.009
2	19.290	20.274	0.984
3	23.020	24.270	1.250
4	25.857	26.198	0.341
5	34.269	35.176	0.907
6	37.814	38.276	0.462
7	41.012	42.305	1.293
8	**42.538**	**45.215**	**2.677**
model C12-ABAB (Fig. S34b and Fig. S42c)			
1	0.0	0.0	0.0
2	17.844	17.844	0.0
3	22.571	22.571	0.0
4	23.421	23.421	0.0
5	27.152	27.152	0.0
6	37.350	37.351	0.001
7	39.945	39.945	0.0
8	**41.234**	**41.236**	**0.002**

Table S19 The selected parameters obtained from modelling the magnetic properties of **2** based on the results of the *ab initio* calculations combined with the fitting of the exchange coupling according to three magneto-structural models, named R6-ABAB, R6-ABAB(4st.), and R12-ABAB (Fig. S34 and Fig. S42). The presented results include the lists of 16 lowest lying exchange states (8 lowest lying pairs of exchange states, pseudo-doublets) and the respective energy gaps. The further, higher lying states are visualized in Fig. S42. The lowest lying pairs of states showing the relatively large energy gaps are emphasized by bold fonts. The labels (4st.) represent the extended calculations employing four higher energy states of each Co centre.

No. of the pair of exchange states (pseudo-doublets)	Energy of a lower lying state / cm^{-1}	Energy of a higher lying state / cm^{-1}	Energy gap / cm^{-1}
model R6-ABAB (Fig. S34c and Fig. S42d)			
1	0.0	0.0	0.0
2	23.285	23.379	0.094
3	25.201	25.351	0.150
4	**30.488**	**30.647**	**0.159**
5	32.577	32.696	0.119
6	37.962	38.066	0.104
7	38.277	38.342	0.065
8	56.093	56.189	0.096
model R6-ABAB(4st.) (Fig. S34c and Fig. S42e)			
1	0.0	0.0	0.0
2	22.181	22.273	0.092
3	23.844	23.974	0.130
4	30.200	30.386	0.186
5	32.056	32.210	0.154
6	**36.253**	**36.514**	**0.261**
7	36.585	36.764	0.179
8	49.724	49.846	0.122
model R12-ABAB (Fig. S34d and Fig. S42f)			
1	0.0	0.0	0.0
2	42.963	42.985	0.022
3	46.085	46.306	0.221
4	**46.425**	**46.602**	**0.177**
5	49.510	49.541	0.031
6	52.108	52.109	0.001
7	54.481	54.483	0.002
8	55.111	55.116	0.005

Table S20 The selected parameters obtained from modelling the magnetic properties of **2** based on the results of the *ab initio* calculations combined with the fitting of the exchange coupling according to three magneto-structural models, named C6-AABB, C6-AABB(4st.), and C12-AABB (Fig. S35 and Fig. S43). The presented results include the lists of 16 lowest lying exchange states (8 lowest lying pairs of exchange states, pseudo-doublets) and the respective energy gaps. The further, higher lying states are visualized in Fig. S43. The lowest lying pairs of states showing the relatively large energy gaps are emphasized by bold fonts. The labels (4st.) represent the extended calculations employing four higher energy states of each Co centre.

No. of the pair of exchange states (pseudo-doublets)	Energy of a lower lying state / cm^{-1}	Energy of a higher lying state / cm^{-1}	Energy gap / cm^{-1}
model C6-AABB (Fig. S35a and Fig. S43a)			
1	0	0.003	0.003
2	27.778	28.031	0.253
3	30.335	30.522	0.187
4	**47.023**	**47.627**	**0.604**
5	50.289	50.435	0.146
6	59.050	59.309	0.259
7	63.899	63.901	0.002
8	63.925	63.944	0.019
model C6-AABB(4st.) (Fig. S35a and Fig. S43b)			
1	0.0	0.002	0.002
2	25.906	26.132	0.226
3	29.093	29.227	0.134
4	41.157	41.723	0.566
5	45.841	46.273	0.432
6	**53.910**	**55.218**	**1.308**
7	59.488	59.536	0.048
8	59.880	61.756	1.876
model C12-AABB (Fig. S35b and Fig. S43c)			
1	0.0	0.0	0.0
2	21.882	21.882	0.0
3	28.070	28.070	0.0
4	30.668	30.668	0.0
5	43.009	43.019	0.010
6	44.878	44.930	0.052
7	47.179	47.442	0.263
8	**48.171**	**48.510**	**0.339**

Table S21 The selected parameters obtained from modelling the magnetic properties of **2** based on the results of the *ab initio* calculations combined with the fitting of the exchange coupling according to three magneto-structural models, named R6-AABB, R6-AABB(4st.), and R12-AABB (Fig. S35 and Fig. S43). The presented results include the lists of 16 lowest lying exchange states (8 lowest lying pairs of exchange states, pseudo-doublets) and the respective energy gaps. The further, higher lying states are visualized in Fig. S43. The lowest lying pairs of states showing the relatively large energy gaps are emphasized by bold fonts. The labels (4st.) represent the extended calculations employing four higher energy states of each Co centre.

No. of the pair of exchange states (pseudo-doublets)	Energy of a lower lying state / cm^{-1}	Energy of a higher lying state / cm^{-1}	Energy gap / cm^{-1}
model R6-AABB (Fig. S35c and Fig. S43d)			
1	0.0	0.005	0.005
2	22.654	22.747	0.093
3	**27.637**	**27.973**	**0.336**
4	30.481	30.767	0.286
5	32.115	32.223	0.108
6	32.932	33.145	0.213
7	48.785	48.862	0.077
8	59.769	60.274	0.505
model R6-AABB(4st.) (Fig. S35c and Fig. S43e)			
1	0.0	0.005	0.005
2	21.297	21.367	0.060
3	26.373	26.796	0.423
4	29.781	30.151	0.370
5	31.661	31.867	0.206
6	32.482	32.737	0.255
7	44.644	44.783	0.139
8	**52.482**	**53.671**	**1.189**
model R12-AABB (Fig. S35d and Fig. S43f)			
1	0.0	0.0	0.0
2	42.316	42.412	0.096
3	**43.240**	**43.382**	**0.142**
4	46.430	46.480	0.050
5	47.958	47.964	0.006
6	52.171	52.181	0.010
7	53.334	53.337	0.003

Table S22 The selected parameters obtained from modelling the magnetic properties of **2** based on the results of the *ab initio* calculations combined with the fitting of the exchange coupling according to three magneto-structural models, named C6-AA+BB (part 1), C6-AA+BB(4st.) (part 1), and C12-AA+BB (part 1) (Fig. S36 and Fig. S44). The presented results include the lists of 16 lowest lying exchange states (8 lowest lying pairs of exchange states, pseudo-doublets) and the respective energy gaps. The further, higher lying states are visualized in Fig. S44. The lowest lying pairs of states showing the relatively large energy gaps are emphasized by bold fonts. The labels (4st.) represent the extended calculations employing four higher energy states of each Co centre.

No. of the pair of exchange states (pseudo-doublets)	Energy of a lower lying state / cm^{-1}	Energy of a higher lying state / cm^{-1}	Energy gap / cm^{-1}
model C6-AA+BB (part 1) (Fig. S36a and Fig. S44a)			
1	0.0	0.024	0.024
2	15.256	15.649	0.393
3	21.621	21.830	0.209
4	24.405	24.991	0.586
5	41.683	42.218	0.535
6	**49.873**	**50.642**	**0.769**
7	55.357	55.362	0.005
8	55.472	55.514	0.042
model C6-AA+BB(4st.) (part 1) (Fig. S36a and Fig. S44b)			
1	0.0	0.022	0.022
2	14.136	14.592	0.456
3	20.723	20.908	0.185
4	**22.821**	**23.807**	**0.986**
5	35.389	36.564	1.175
6	46.445	47.546	1.101
7	50.642	50.644	0.002
8	51.061	53.939	2.878
model C12-AA+BB (part 1) (Fig. S36b and Fig. S44c)			
1	0.0	0.0	0.0
2	16.162	16.163	0.001
3	22.169	22.169	0.0
4	22.532	22.533	0.001
5	25.397	25.399	0.002
6	**35.516**	**35.760**	**0.244**
7	35.851	36.123	0.272
8	38.397	38.436	0.039

Table S23 The selected parameters obtained from modelling the magnetic properties of **2** based on the results of the *ab initio* calculations combined with the fitting of the exchange coupling according to three magneto-structural models, named R6-AA+BB (part 1), R6-AA+BB(4st.) (part 1), and R12-AA+BB (part 1) (Fig. S36 and Fig. S44). The presented results include the lists of 16 lowest lying exchange states (8 lowest lying pairs of exchange states, pseudo-doublets) and the respective energy gaps. The further, higher lying states are visualized in Fig. S44. The lowest lying pairs of states showing the relatively large energy gaps are emphasized by bold fonts. The labels (4st.) represent the extended calculations employing four higher energy states of each Co centre.

No. of the pair of exchange states (pseudo-doublets)	Energy of a lower lying state / cm^{-1}	Energy of a higher lying state / cm^{-1}	Energy gap / cm^{-1}
model R6-AA+BB (part 1) (Fig. S36c and Fig. S44d)			
1	0.0	0.010	0.010
2	14.700	14.818	0.118
3	20.515	20.656	0.141
4	30.635	31.762	1.127
5	35.124	35.492	0.368
6	36.228	37.089	0.861
7	**41.635**	**46.298**	**4.663**
8	46.394	48.446	2.052
model R6-AA+BB(4st.) (part 1) (Fig. S36c and Fig. S44e)			
1	0.0	0.006	0.006
2	14.952	15.011	0.059
3	21.650	21.735	0.085
4	**29.340**	**31.429**	**2.089**
5	32.583	34.821	2.238
6	36.191	37.276	1.085
7	38.658	42.626	3.968
8	43.113	45.705	2.592
model R12-AA+BB (part 1) (Fig. S36d and Fig. S44f)			
1	0.0	0.0	0.0
2	37.008	37.097	0.089
3	39.792	39.793	0.001
4	**42.161**	**42.804**	**0.643**
5	44.190	44.505	0.315
6	44.511	44.674	0.163
7	48.431	49.239	0.808
8	51.143	52.164	1.021

Table S24 The selected parameters obtained from modelling the magnetic properties of **2** based on the results of the *ab initio* calculations combined with the fitting of the exchange coupling according to three magneto-structural models, named C6-AA+BB (part 2), C6-AA+BB(4st.) (part 2), and C12-AA+BB (part 2) (Fig. S37 and Fig. S45). The presented results include the lists of 16 lowest lying exchange states (8 lowest lying pairs of exchange states, pseudo-doublets) and the respective energy gaps. The further, higher lying states are visualized in Fig. S45. The lowest lying pairs of states showing the relatively large energy gaps are emphasized by bold fonts. The labels (4st.) represent the extended calculations employing four higher energy states of each Co centre.

No. of the pair of exchange states (pseudo-doublets)	Energy of a lower lying state / cm^{-1}	Energy of a higher lying state / cm^{-1}	Energy gap / cm^{-1}
model C6-AA+BB (part 2) (Fig. S37a and Fig. S45a)			
1	0.0	0.002	0.002
2	24.264	24.409	0.145
3	27.787	27.897	0.110
4	**36.851**	**37.381**	**0.530**
5	46.044	46.434	0.390
6	55.449	55.892	0.443
7	60.898	60.901	0.003
8	61.040	61.065	0.025
model C6-AA+BB(4st.) (part 2) (Fig. S37a and Fig. S45b)			
1	0.0	0.001	0.001
2	22.650	22.800	0.150
3	26.683	26.760	0.077
4	**34.374**	**35.387**	**1.013**
5	40.616	41.525	0.909
6	51.663	52.477	0.814
7	56.981	56.988	0.007
8	57.928	60.095	2.167
model C12-AA+BB (part 2) (Fig. S37b and Fig. S45c)			
1	0.0	0.0	0.0
2	24.529	24.529	0.0
3	28.009	28.009	0.0
4	37.964	37.964	0.0
5	40.864	40.865	0.001
6	**44.925**	**44.934**	**0.009**
7	46.264	46.278	0.014
8	49.222	49.233	0.011

Table S25 The selected parameters obtained from modelling the magnetic properties of **2** based on the results of the *ab initio* calculations combined with the fitting of the exchange coupling according to three magneto-structural models, named R6-AA+BB (part 2), R6-AA+BB(4st.) (part 2), and R12-AA+BB (part 2) (Fig. S37 and Fig. S45). The presented results include the lists of 16 lowest lying exchange states (8 lowest lying pairs of exchange states, pseudo-doublets) and the respective energy gaps. The further, higher lying states are visualized in Fig. S45. The lowest lying pairs of states showing the relatively large energy gaps are emphasized by bold fonts. The labels (4st.) represent the extended calculations employing four higher energy states of each Co centre.

No. of the pair of exchange states (pseudo-doublets)	Energy of a lower lying state / cm^{-1}	Energy of a higher lying state / cm^{-1}	Energy gap / cm^{-1}
model R6-AA+BB (part 2) (Fig. S37c and Fig. S45d)			
1	0.0	0.033	0.033
2	5.572	5.686	0.114
3	12.620	12.762	0.142
4	15.558	15.729	0.171
5	20.091	20.211	0.120
6	20.618	20.859	0.241
7	**27.064**	**27.498**	**0.434**
8	28.537	28.668	0.131
model R6-AA+BB(4st.) (part 2) (Fig. S37c and Fig. S45e)			
1	0.0	0.023	0.023
2	6.307	6.373	0.066
3	14.174	14.255	0.081
4	16.230	16.502	0.272
5	20.695	20.792	0.097
6	21.829	22.068	0.239
7	**25.093**	**25.990**	**0.897**
8	27.452	27.577	0.125
model R12-AA+BB (part 2) (Fig. S37d and Fig. S45f)			
1	0.0	0.0	0.0
2	46.181	46.181	0.0
3	50.441	50.441	0.0
4	**53.124**	**53.125**	**0.001**
5	56.000	56.000	0.0
6	56.025	56.025	0.0
7	58.200	58.200	0.0
8	59.815	59.815	0.0

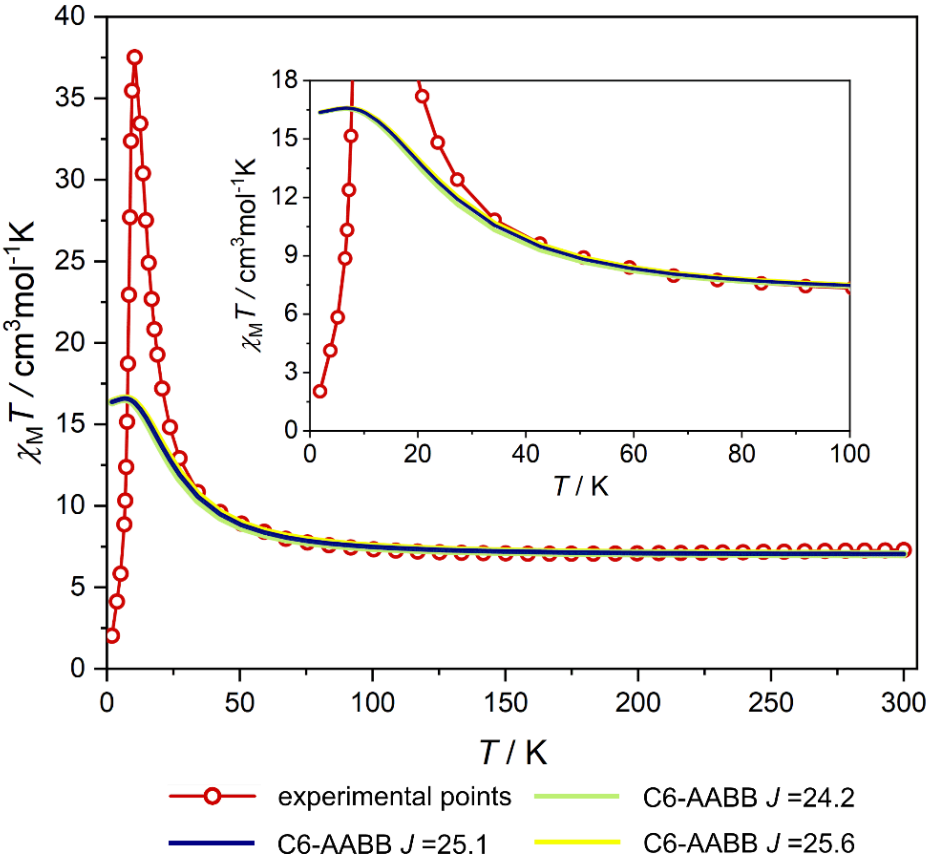

Fig. S49 Experimental temperature dependence of the $\chi_M T$ product under H_{dc} = 1000 Oe for **2** compared with the $\chi_M T(T)$ plots simulated using the results of the *ab initio* calculations combined with the fitting of the exchange coupling employing the magneto-structural model of C6-AABB with three different indicated coupling constants, *J* of 24.2, 25.1, and 25.6 cm^{-1} (*J'* was fixed to be –0.6 cm^{-1} following the analysis of the magnetic data for compound 1).

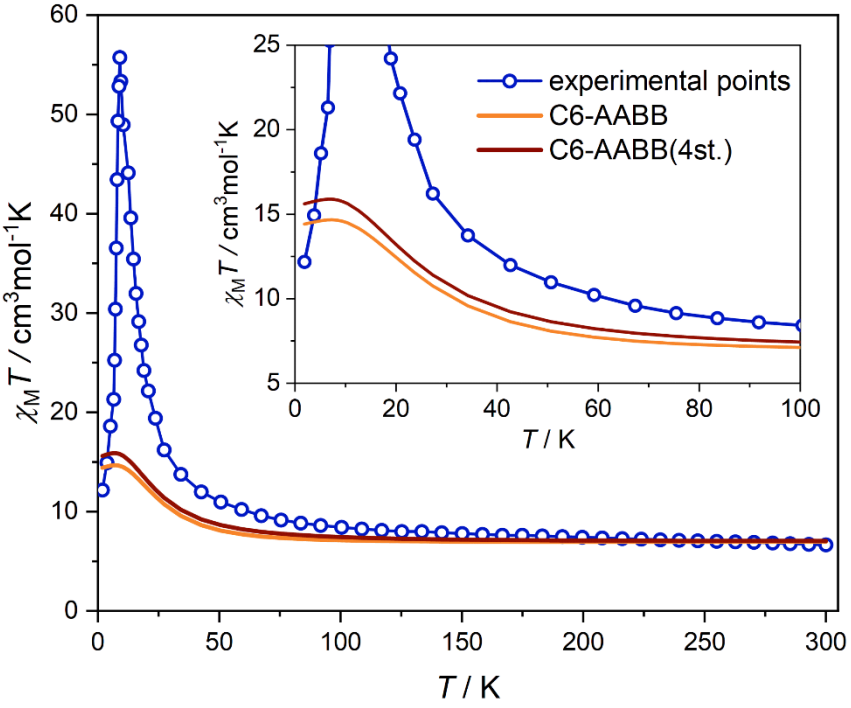

Fig. S50 Experimental temperature dependence of the $\chi_M T$ product under H_{dc} = 1000 Oe for **3** compared with the $\chi_M T(T)$ curves calculated using the results of the *ab initio* calculations combined with the simulations of magnetic exchange employing C6-AABB and C6-AABB(4st.) models. All simulations are shown for the best-fit using the J value of 25.1 cm^{-1} and the J' of –0.6 cm^{-1} taken from the modelling of the magnetic properties of **1** (Fig. 6). The extension (4st.) used for the part of the presented models represent the extended calculations employing four higher lying energy states of each Co centre while only the lowest ones are used for other calculations.

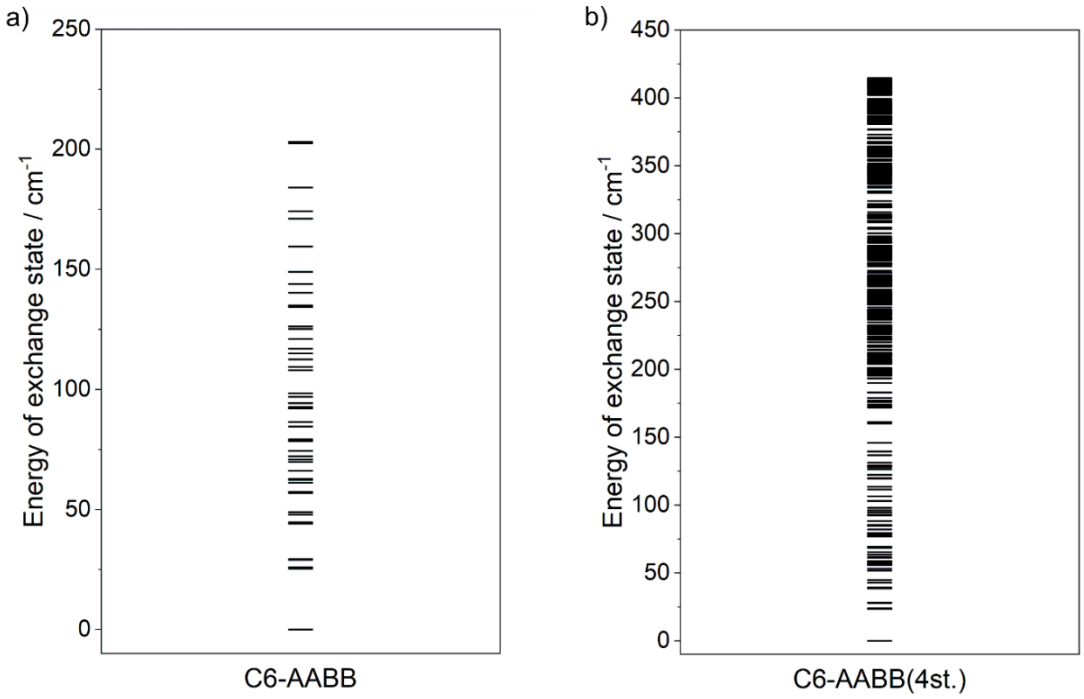

Fig. S51 The scheme of exchange states for **3** calculated using the results of the *ab initio* calculations (Tables S9–S10, Fig. 5, and Fig. 7) combined with the fitting of the exchange coupling pathways according to two selected magneto-structural models of C6-AABB and C6-AABB(4st.). The extension (4st.) used for the part of the presented models represent the extended calculations employing four higher lying energy states of each Co centre while only the lowest ones are used for other calculations. For the visualization of the indicated models see Fig. S35. The results are for the optimized set of exchange coupling constants of J = 25.1 cm^{-1}, J' = –0.6 cm^{-1}.

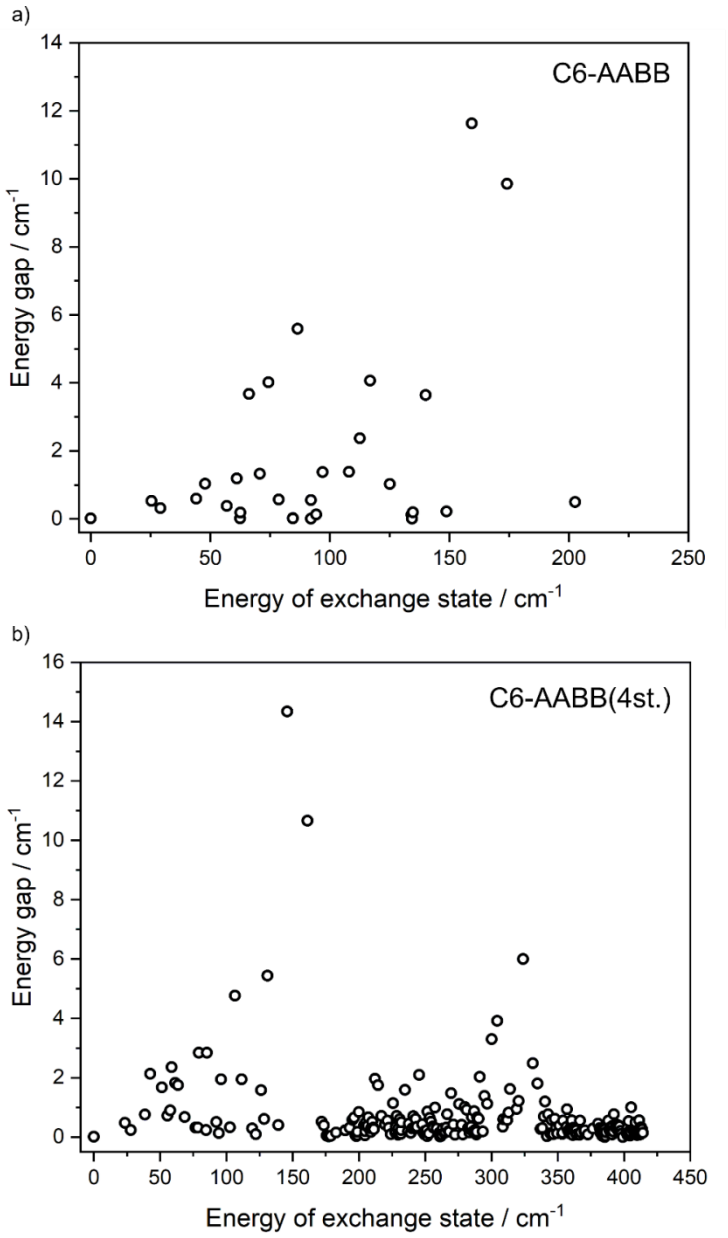

Fig. S52 The dependence between the average energy of the pairs of exchange states (pseudo-doublets) and the related energy gaps determined for **3** using the *ab initio* calculations combined with the fitting of the exchange constant according to two selected magneto-structural models, named C6-AABB (a) and C6-AABB(4st.) (b) (these models produced the best-fit to the experimental data). The models are visualized in Fig. 7 and Fig. S35 while the numerical data for the obtained exchange states are gathered in Table 3 and Table S26.

Table S26 The selected parameters obtained from modelling the magnetic properties of **3** based on the results of the *ab initio* calculations combined with the fitting of the exchange coupling according to two magneto-structural models, named C6-AABB and C6-AABB(4st.), and R12-AABB (Fig. S35 and Fig. S51). The presented results include the lists of 16 lowest lying exchange states (8 lowest lying pairs of exchange states, pseudo-doublets) and the respective energy gaps. The further, higher lying states are visualized in Fig. S51. The lowest lying pairs of states showing the relatively large energy gaps are emphasized by bold fonts. The labels (4st.) represent the extended calculations employing four higher energy states of each Co centres.

No. of the pair of exchange states (pseudo-doublets)	Energy of a lower lying state / cm^{-1}	Energy of a higher lying state / cm^{-1}	Energy gap / cm^{-1}
model C6-AABB (Fig. S35a and Fig. S51a)			
1	0.0	0.01	0.010
2	25.403	25.931	0.528
3	29.076	29.392	0.316
4	44.076	44.665	0.589
5	**47.867**	**48.904**	**1.037**
6	56.869	57.246	0.377
7	61.135	62.320	1.185
8	62.502	62.515	0.013
model C6-AABB(4st.) (Fig. S35a and Fig. S51b)			
1	0.0	0.008	0.008
2	23.392	23.874	0.482
3	27.929	28.161	0.232
4	38.602	39.361	0.759
5	**42.600**	**44.732**	**2.132**
6	51.396	53.066	1.670
7	55.624	56.347	0.723
8	57.604	58.505	0.901

(a) chains with Co/W = 1/1

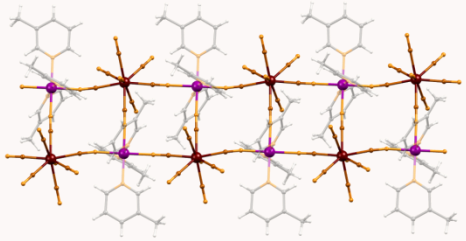

$(Ph_4P)[Co^{II}(3\text{-Mepy})_{2.7}(H_2O)_{0.3}W^{V}(CN)_8]]\cdot 0.6H_2O$

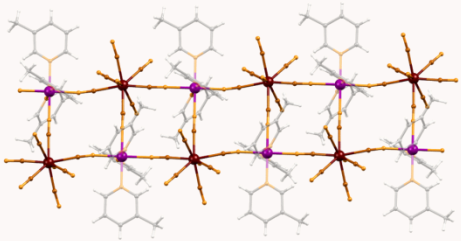

$\{(Ph_4As)[Co^{II}(3\text{-Mepy})_3W^{V}(CN)_8]\}$

(b) chains with Co/W = 3/2

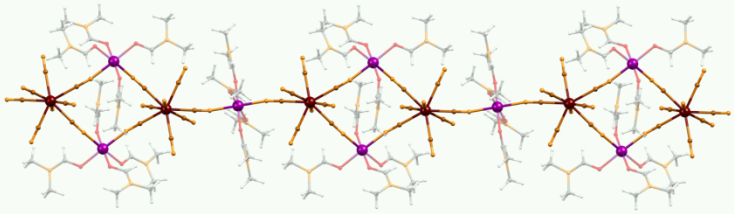

$\{[Co^{II}_3(DMF)_{12}][W^{V}(CN)_8]_2]\}$

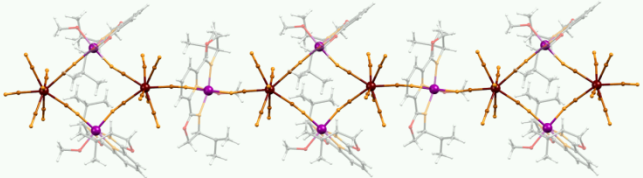

$\{[Co^{II}((S,S)\text{-iPrPybox})(MeOH)]_3[W^{V}(CN)_8]_2\}\cdot 5.5MeOH\cdot 0.5H_2O$

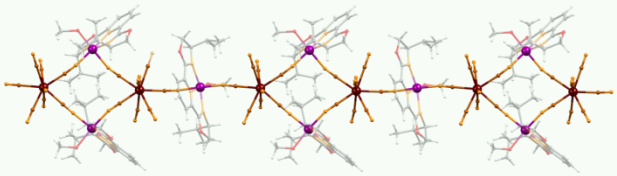

$\{[Co^{II}((R,R)\text{-iPrPybox})(MeOH)]_3[W^{V}(CN)_8]_2\}\cdot 5.5MeOH\cdot 0.5H_2O$

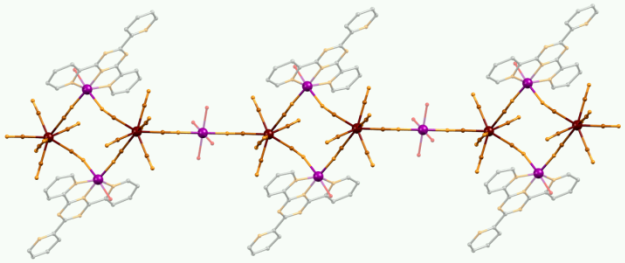

$\{[Co^{II}(tptz)(H_2O)]_2[Co^{II}(H_2O)_4][W^{V}(CN)_8]_2\}\cdot 2H_2O$

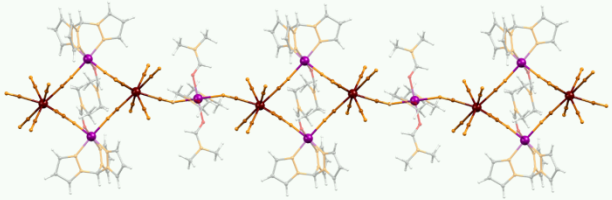

$\{[Co^{II}(tpm)(DMF)]_2[Co^{II}(DMF)_4][W^{V}(CN)_8]_2\}\cdot 2DMF$

(c) chains with Co/W = 2/1

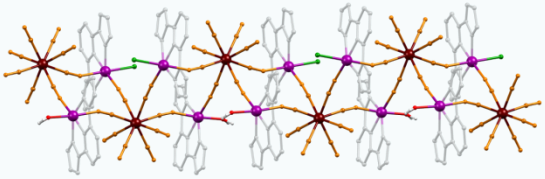

$\{[Co^{II}(bpp)Cl_{0.5}(H_2O)_{0.5}]_2[W^{V}(CN)_8]\}\cdot 2H_2O$

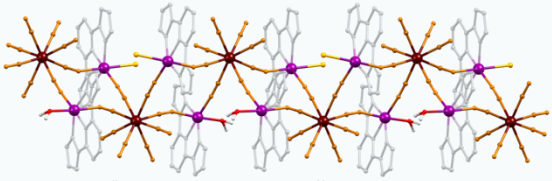

$\{[Co^{II}(bpp)Br_{0.5}(H_2O)_{0.5}]_2[W^{V}(CN)_8]\}\cdot 2H_2O$

Fig. S53 Comparison of the representative structural fragments of **2** and **3** with other reported cyanido-bridged Co^{II}–$[W^{V}(CN)_8]^{3-}$ chains, including the chains with Co/W ratio of 1/1 (*a*, reference S3), Co/W ratio of 3/2 (*b*, references S4–S7), and Co/W ratio of 2/1 (*c*, compounds **2** and **3**, this work). The formula of the respective compound is shown below each structural fragment. A more detailed comparison of structural features and magnetic properties of **2** and **3** with other reported Co–W chains is provided in Table S26. The abbreviations for ligands are gathered in Table S27.

Table S27 Comparison of structural features and magnetic properties of **2** and **3** with other reported Co^{II}–$[W^{V}(CN)_8]^{3-}$ chains.

I [S8]

$(Ph_4P)[Co^{II}(3\text{-Mepy})_{2.7}(H_2O)_{0.3}W^{V}(CN)_8]\cdot 0.6H_2O$ / 3-Mepy = 3-methylpyridine

Co/W ratio	Topology	Co^{II} complex	Magnetic properties
1:1	3,3-ladder	**O_h** $[Co^{II}(3\text{-Mepy})_{2.7}(H_2O)_{0.3}(NC)_3]^-$	**Ferromagnetic intrachain coupling** **Single-Chain Magnet (SCM)** Δ_τ (infinite-size chain) = 252(9) K (176(6) cm^{-1}) Δ_τ (finite-size chain) = 169(2) K (118(1) cm^{-1}) τ_0 values between 10^{-10} and 10^{-13} s **Magnetic hysteresis loop at T = 1.8 K** H_c = 26.2 kOe, M_r = 1.28 μ_B (along chain axis) H_c = 12.5 kOe, M_r = 3.1 μ_B (perpendicular to chain axis)

II [S8]

$(Ph_4As)[Co^{II}(3Mepy)_3W^{V}(CN)_8]$ / 3-Mepy = 3-methylpyridine

Co/W ratio	Topology	Co^{II} complex	Magnetic properties
1:1	3,3-ladder	**O_h** $[Co^{II}(3\text{-Mepy})_3(NC)_3]^-$	**Ferromagnetic intrachain coupling** **Single-Chain Magnet (SCM)** Δ_τ (infinite-size chain) = 224(7) K (156(5) cm^{-1}) Δ_τ (finite-size chain) = 154(1) K (107(1) cm^{-1}) τ_0 values between 10^{-10} and 10^{-13} s **Magnetic hysteresis loop at T = 1.8 K** H_c = 22.6 kOe, M_r = 1.27 μ_B (along chain axis) H_c = 7.9 kOe, M_r = 3.6 μ_B (perpendicular to chain axis)

III [S9]

$\{[Co^{II}_3(DMF)_{12}][W^{V}(CN)_8]_2]\}$ / DMF = N,N-Dimethylformamide

Co/W ratio	Topology	Co^{II} complex	Magnetic properties
3:2	3,2-chain	**O_h** $[Co^{II}(DMF)_4(NC)_2]$	**Ferromagnetic intrachain coupling** **Ferromagnetic long-range ordering** below T_C = 7.3 K **Magnetic hysteresis loop at T = 1.8 K** H_c = 907 Oe, M_r = 3.39 μ_B **Spin glass behaviour** with $\Delta E/k_B$ = 170(3) K and $\tau_0 = 2.3\cdot10^{-15}$ s

IV [S10]

$\{[Co^{II}((S,S)\text{-}i\text{PrPybox})(MeOH)]_3[W^{V}(CN)_8]_2\}\cdot 5.5MeOH\cdot 0.5H_2O$

*i*PrPybox = 2,2′-(2,6-pyridinediyl)bis(4-isopropyl-2-oxazoline)

Co/W ratio	Topology	Co^{II} complex	Magnetic properties
3:2	3,2-chain	**O_h** $[Co^{II}((S,S)\text{-}i\text{PrPybox})(MeOH)(NC)_2]$	**Mixed scheme of ferromagnetic and antiferromagnetic intrachain coupling** **Onset of SCM behaviour** with $\Delta E/k_B$ = 6 K (4.2 cm^{-1}) and $\tau_0 = 5\cdot10^{-7}$ s **Lack of magnetic hysteresis loop down to 1.8 K**

V [S10]

$\{[Co^{II}((R,R)\text{-}i\text{PrPybox})(MeOH)]_3[W^{V}(CN)_8]_2\}\cdot 5.5MeOH\cdot 0.5H_2O$

*i*PrPybox = 2,2′-(2,6-pyridinediyl)bis(4-isopropyl-2-oxazoline)

Co/W ratio	Topology	Co^{II} complex	Magnetic properties
3:2	3,2-chain	**O_h** $[Co^{II}((R,R)\text{-}i\text{PrPybox})(MeOH)(NC)_2]$	**Mixed scheme of ferromagnetic and antiferromagnetic intrachain coupling** **Onset of SCM behaviour, Lack of magnetic hysteresis loop down to 1.8 K**

VI [S11]

$\{[Co^{II}(tptz)(H_2O)]_2[Co^{II}(H_2O)_4][W^{V}(CN)_8]_2\}\cdot 2H_2O$ / tptz = 2,4,6-tris(2-pyridyl)-1,3,5-triazine

Co/W ratio	Topology	Co^{II} complex	Magnetic properties
3:2	3,2-chain	**O_h** $[Co^{II}(tptz)(H_2O)(NC)_2]$ and $[Co^{II}(H_2O)_4(NC)_2]$	**Ferromagnetic intrachain coupling** **Onset of SCM behaviour, Lack of magnetic hysteresis loop down to 1.8 K**

VII [S12]

{[Co^{II}(tpm)(DMF)]$_2$[Co^{II}(DMF)$_4$][W^{V}(CN)$_8$]$_2$}·2DMF / tmp = 1,1,1-trispyrazoylmethane

Co/W ratio	Topology	Co^{II} complex	Magnetic properties
3:2	3,2-chain	**O$_h$** [Co^{II}(tpm)(DMF)(NC)$_2$] and [Co^{II}(DMF)$_4$(NC)$_2$]	**Ferromagnetic intrachain coupling** **Antiferromagnetic interchain interactions** **Field-induced metamagnetic transition** with H_C = 300 Oe at T = 1.8 K **Antiferromagnetic long-range ordering** below T_N = 3.4 K **Single-Chain Magnet (SCM)** Δ_τ (infinite-size chain) = 57.1(4) K (38.3(2) cm^{-1}) Δ_τ (finite-size chain) = 45.8(3) K (25.1(7) cm^{-1}) τ_0 values between 10^{-7} and 10^{-10} s **Magnetic hysteresis loop at T = 1.8 K** H_c = 40 Oe, M_r = 0.6 μ_B

VIII [*]

{[Co^{II}(bpp)Cl$_{0.5}$(H$_2$O)$_{0.5}$]$_2$[W^{V}(CN)$_8$]}·2H$_2$O (**2**) / bpp = 2,6-di(1-pyrazolyl)pyridine

Co/W ratio	Topology	Co^{II} complex	Magnetic properties
2:1	chains of vertex- sharing squares	**O$_h$** [Co^{II}(bpp)(Cl)$_{0.5}$(H$_2$O)$_{0.5}$(CN)$_2$]$^{0.5-}$	**Ferromagnetic intrachain coupling** **Antiferromagnetic interchain interactions** **Field-induced metamagnetic transition** with H_C = 2180 Oe at T = 2 K (two-step transition in the 3–7 K) **Antiferromagnetic long-range ordering** below T_N = 9.5 K **Single-Chain Magnet (SCM)** Δ_τ (infinite-size chain) – not observed Δ_τ (finite-size chain) = 65(1) K (45.4(7) cm^{-1}) with τ_0 = 2.1(7)·10^{-10} s **Magnetic hysteresis loop at T = 1.8 K** H_c = 700 Oe, M_r = 0.4 μ_B

IX [*]

{[Co^{II}(bpp)Br$_{0.5}$(H$_2$O)$_{0.5}$]$_2$[W^{V}(CN)$_8$]}·2H$_2$O (**2**) / bpp = 2,6-di(1-pyrazolyl)pyridine

Co/W ratio	Topology	Co^{II} complex	Magnetic properties
2:1	chains of vertex- sharing squares	**O$_h$** [Co^{II}(bpp)(Br)$_{0.5}$(H$_2$O)$_{0.5}$(CN)$_2$]$^{0.5-}$	**Ferromagnetic intrachain coupling** **Antiferromagnetic interchain interactions** **Field-induced metamagnetic transition** with H_C = 2050 Oe at T = 2 K (two-step transition in the 3–7 K) **Antiferromagnetic long-range ordering** below T_N = 9.4 K **Single-Chain Magnet (SCM)** Δ_τ (infinite-size chain) – not observed Δ_τ (finite-size chain) = 59.7(8) K (41.5(4) cm^{-1}) with τ_0 = 5.6(8)·10^{-10} s **Magnetic hysteresis loop at T = 1.8 K** H_c = 450 Oe, M_r = 0.32 μ_B

*This work

S8 R.-M. Wei, F. Cao, J. Li, L. Yang, Y. Han, X.-L. Zhang, Z. Zhang, X.-Y. Wang, Y. Song, Single-Chain Magnets Based on Octacyanotungstate with the Highest Energy Barrier for Cyanide Compounds, *Sci. Rep.*, 2016, **6**, 24372.

S9 D. Li, L. Zheng, Y. Zhang, J. Huang, S. Gao, W. Tang, Coexistence of Long-Range Ferromagnetic Ordering and Glassy Behavior in One-Dimensional Bimetallic Cyano-Bridged Polymers, *Inorg. Chem.* 2003, **42**, 6123–6129

S10 S. Chorazy, K. Nakabayashi, K. Imoto, J. Mlynarski, B. Sieklucka, S. Ohkoshi, Conjunction of Chirality and Slow Magnetic Relaxation in the Supramolecular Network Constructed of Crossed Cyano-Bridged Co^{II}–W^{V} Molecular Chains, *J. Am. Chem. Soc.*, 2012, **134**, 16151–16154.

S11 H. Zhao, A. J. Brown, A. V. Prosvirin, K. R. Dunbar, One-dimensional square- and ladder-type architectures incorporating octacyanometallates of molybdenum(V) and tungsten(V), *Polyhedron*, 2013, **64**, 321-327.

S12 Y.-Z. Zhang, B. S. Dolinar, S. Liu, A. J. Brown, X. Zhang, Z.-X. Wang and K. R. Dunbar, Enforcing Ising-like magnetic anisotropy via trigonal distortion in the design of a W(V)–Co(II) cyanide single-chain magnet, *Chem. Sci.*, 2018, **9**, 119-124.